Flux Pumping for High-T_c Superconducting (HTS) Magnets

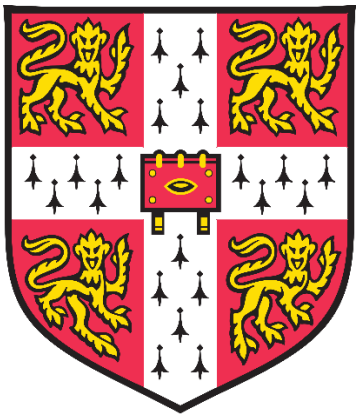

JIANZHAO GENG

Trinity Hall College

University of Cambridge

A thesis submitted for the degree of

Doctor of Philosophy

April 2017

Declaration of Originality

The work presented in this thesis was carried out in Department of Engineering, University of Cambridge, under the supervision of Dr. T. A. Coombs from October 2014 to April 2017.

The author declares that this thesis is his original work, except for where specific reference is made to others' work. This thesis has not been previously submitted in part, or in whole, to any other universities for a degree, diploma or other qualification. This thesis is within the limit of 65,000 words length.

Signature:

Acknowledgements

I would like to express my heartfelt thanks to my supervisor, Dr. Timothy A. Coombs, and his wife Mrs. Coombs. Dr. Coombs helped me in choosing this interesting topic. He also offered me great instruction, a lot of beneficial discussions, and abundant freedom in my research. I would like to give thanks to Mrs. Coombs for her sincere care.

I would also like to thank my colleagues in Superconductivity Group, for their generous help and support, and for their companion. In no particular order, I would like to thank Dr. Wei Wang, Dr. Koichi Matsuda, Dr. Mehdi Baghdadi, Dr. Zhaoyang Zhong, Dr. Zhen Huang, Dr. Yujia Zhai, Dr. Lin Fu, Heng Zhang, Xiuchang Zhang, Boyang Shen, Qihuan Dong, Chao Li, Jun Ma, and Jemie Gawith. I would like to thank Mr. John Grundy and other technicians in our workshop for their help.

I would like to give thanks to Prof. Yuki Iwasa from MIT, Prof. Justin Schwartz from NCSU, and Prof. Seungyong Hahn from FSU for hosting me during my academic visit in the USA, also for their strong support and beneficial discussions. I would like to give sincere thanks to Dr. Min Zhang from Bath University for her help in the application of my PhD study in Cambridge.

I would like to give acknowledgement to the Cambridge Trust, for offering me a Cambridge International Scholarship to support my study in Cambridge.

Last but not least, I am grateful to my girlfriend Ruby Cao for her love and sacrifice, and to my dearest family and friends.

PUBLICATIONS DURING PHD

[1] **J. Geng**, and T. A. Coombs, "Apparatus and methods for changing the magnetisation of a superconductor", *International Patent*, WO2017021674 (published in 2017).

[2] **J. Geng**, and T. A. Coombs, "Mechanism of a high-*T*c superconducting flux pump: Using alternating magnetic field to trigger flux flow", *Appl. Phys. Lett.*, **107**, 142601 (2015).

[3] **J. Geng**, et al, "Voltage-ampere characteristics of YBCO coated conductor under inhomogeneous oscillating magnetic field", *Appl. Phys. Lett.*, **108**, 262601 (2016).

[4] **J. Geng**, et al, "Origin of dc voltage in type II superconducting flux pumps: Field, field rate of change, and current density dependence of resistivity", *J. Phys. D: Appl. Phys.*, **49**, 11LT01 (2016).

[5] **J. Geng**, K. Matsuda, L. Fu, B. Shen, X. Zhang, and T. A. Coombs, "Operational research on a high- *T*c rectifier-type superconducting flux pump", *Supercond. Sci. Technol.*, **29**, 035015 (2016).

[6] **J. Geng**, and T. A. Coombs, "An HTS flux pump operated by directly driving a superconductor into flux flow region in the *E*–*J* curve", *Supercond.Sci. Technol.*, **29**, 095004 (2016).

[7] **J. Geng**, et al, "HTS persistent current switch controlled by AC magnetic field", *IEEE Trans. Appl. Supercond.*, **26**(3), 6603304 (2016).

[8] **J. Geng**, et al, "Feedback control of a rectifier type HTS flux pump: stabilizing load current with minimized losses", *IEEE Trans. Appl. Supercond.*, **27**(4), 0500104 (2017).

[9] **J. Geng**, H. Zhang, C. Li, X. Zhang, B. Shen, and T. A. Coombs, "Angular dependence of direct current decay in a closed YBCO double-pancake coil under

external AC magnetic field and reduction by magnetic shielding", *Supercond. Sci. Technol.*, **30**, 035022 (2017)

[10] **J. Geng**, C. Li, and T. A. Coombs, "A fast AC field controlled impedance in HTS coated conductors: response speed and electric field value", *IEEE Trans. Appl. Supercond.*.(published online 2017)

[11] T. A. Coombs, **J. Geng**, L. Fu, and K. Matsuda, "An Overview of Flux Pumps for HTS Coils", *IEEE Trans. Appl. Supercond.*, **27**(4), 4600804 (2017).

[12] H. Zhang, **J. Geng**, B. Shen, X. Zhang, M. Baghdadi, and T. A. Coombs, "Uniform Magnetic Field Mapping With HTS Coils: Conceptual Design and Optimization", *IEEE Trans. Appl. Supercond.*, **26**(3), 9000905 (2016).

[13] H. Zhang, **J. Geng**, B. Shen, L. Fu, X. Zhang, C. Li, J. Li, and T. A. Coombs, "Magnetization of HTS Coated Conductor Stacks using Flux Pumping", *IEEE Trans. Appl. Supercond.*. (published online 2017)

[14] B. Shen, L. Fu, **J. Geng**, H. Zhang, X. Zhang, Z. Zhong, Z. Huang, and T. A. Coombs, "Design of a Superconducting Magnet for Lorentz Force Electrical Impedance Tomography",*IEEE Trans. Appl. Supercond.*, **26**(3), 4400205(2016).

[15] B. Shen, L. Fu, **J. Geng**, X. Zhang, H. Zhang, Q. Dong, C. Li, J. Li, and T. A. Coombs, "Design and simulation of superconducting Lorentz Force Electrical Impedance Tomography (LFEIT)", *Physica C*, **524**, 5-12 (2016).

[16] X. Zhang, H. S. Ruiz, **J. Geng**, B. Shen, L. Fu, H. Zhang, and T. A. Coombs, "Power flow analysis and optimal locations of resistive type superconducting fault current limiters", *SpringerPlus*, **5**(1), 1972 (2016).

[17] Z. Huang, H. S. Ruiz, Y. Zhai, **J. Geng**, B. Shen, and T. A. Coombs, "Study of the Pulsed Field Magnetization Strategy for the Superconducting Rotor", *IEEE Trans. Appl. Supercond.*, **26**(4), 5202105(2016).

[18] X. Zhang, Z. Zhong, H. S. Ruiz, **J. Geng**, T. A. Coombs, “General approach for the determination of the magneto-angular dependence of the critical current of YBCO coated conductors”, *Supercond. Sci. Technol.*, **30**(2), 025010(2017).

[19] X. Zhang, H. S. Ruiz, **J. Geng**, and T. A. Coombs, “Optimal location and minimum number of superconducting fault current limiters for the protection of power grids”, *JEPE*, **87**, 136-143(2017).

[20] B. Shen, **J. Geng**, C. Li, X. Zhang, L. Fu, H. Zhang, J. Ma, and T. A. Coombs, “Optimization study on the magnetic field of superconducting Halbach Array magnet”, *Physica C*, **538**, 46-51 (2017).

[21] B. Shen, J. Li, **J. Geng**, L. Fu, X. Zhang, H. Zhang, C. Li, F. Grilli, and T. A. Coombs, “Investigation of AC losses in horizontally parallel HTS tapes”, *Supercond. Sci. Technol.*, published online 2017.

CONTENTS

List of Figures

Introduction

High T_c superconductors are enabling in the generation of extremely high magnetic fields. Flux pumping is a promising technology which can be used to operate HTS magnets without significant loss. In this decade, several HTS flux pumps based on travelling magnetic waves have been developed, yet their physics is still unclear. This thesis presents a thorough study on flux pumping for HTS coils. It will provide a brand new perspective to comprehensively understand flux pumping behaviour in type II superconductors, as well as present novel flux pump devices with enhanced performances.

Chapter 1 presents a brief introduction to superconductivity and its basic theories. It begins with the definition of superconductivity and the classification of superconductors. Macroscopic magnetization theories of type II superconductors are also introduced.

Chapter 2 explains the practical need and the purposes of the study in this thesis. Superconductor in high field applications is firstly introduced. The problems of operating HTS magnets in persistent current mode are analyzed, and the solution of using flux pumps is proposed. Several LTS and HTS flux pumps are introduced. Existing problems in travelling wave flux pumps such as their ambiguous physics and the limits to their performance are discussed.

In Chapter 3, the idea of using an AC magnetic field to induce a dynamic resistance in a piece of high T_c superconductor as a persistent current switch is proposed. Firstly the well-known effect that flux flow can be triggered when a DC transporting type-II superconductor is subjected to a perpendicular AC field is introduced. Then an AC field controlled switch is described to charge an HTS magnet. The time constant for transition between on and off states when actuated by a high frequency applied field is also investigated, and the results show that the proposed switch is considerably faster than heat controlled switches.

In Chapter 4, a novel flux pumping mechanism which is based on AC field triggered flux flow will be proposed. In the flux pump, a bridge superconductor shorts an HTS load. Low frequency alternating current is firstly induced in the bridge, and a high frequency AC field is then intermittently applied perpendicular the bridge, when the induced transport current in the bridge is in the same direction. The AC field triggers flux flow across the bridge superconductor, which is unidirectional. Flux gradually accumulates in the load, and flux pumping is thus achieved. An experimental system will be built to verify the proposed mechanism, and various influencing factors will be experimentally investigated. A feedback control system will be developed to achieve stabilized field and constant voltage output. This is the first HTS flux pump in which the physics is unambiguous and which is able to inject quantitative flux into superconducting circuits.

In Chapter 5, a novel self-switching HTS flux pump is to be presented. The flux pump further simplifies the work in Chapter 4. Instead of developing flux flow in the bridge superconductor by AC field, the self-switching flux pump is achieved by driving bridge superconductor into flux flow region using induced asymmetrical transport current. A transformer generates a high alternating secondary current with its positive peak value much larger than the negative peak value. During each cycle, around the positive peak of the secondary current, the bridge superconductor is driven into the flux flow region, whereas during the rest of the cycle the bridge remains superconducting. Flux is then accumulated in the load. This will be the simplest HTS flux pump both in physics and realization.

In Chapter 6, a generalized explanation to understand the physics of all flux pumps involving type II superconductors is given, although the work is mainly aimed to explain travelling wave based flux pumps. It will reveal that variation in the resistivity of type II superconductors is the origin of the DC component of the open circuit voltage of travelling wave flux pumps. Because the resistivity of type II superconductors depends on the field magnitude, field rate of change, and current density, when a travelling wave is applied to a superconducting loop, there is different and differing

resistivity around the loop. This results in a DC open circuit voltage and is the origin of flux pumping in travelling wave flux pumps.

Chapter 7 will present the investigation of the *V-I* curve of YBCO coated conductor under inhomogeneous AC field. The results are distinct from the well recognized dynamic resistance model in which the superconductor is under homogeneous AC field. When the transport current is low, the result follows the flux pump model proposed in Chapter 6, whereas when transport current approaches the critical value, the flux pumping effect gradually disappears. A circuit model is proposed which is a combination of the proposed flux pump model together with flux motion characteristics in DC carrying superconductor under an AC field. The result may help researchers further understand the magnetization behaviour of coated conductors under travelling magnetic field.

Chapter 8 presents a summary of this thesis, and proposes future work.

Chapter 1

Brief Introduction to Superconductivity

1.1 Introduction

In 1911, Dutch scientist H. Onnes discovered that the resistance of mercury suddenly dropped to zero at the temperature just below 4.2 Kelvin. He then defined this phenomenon as a superconductive state [1]. For many years after Onnes's discovery, superconductor was considered as an ideal conductor below a critical temperature (T_c). In 1933, W. Meissner and R. Ochsenfeld discovered the Meissner Effect [2], which occurs when the superconductor acts as a perfect diamagnet. The difference between an ideal conductor and a superconductor under field cooling condition is illustrated by Fig. 1.1.

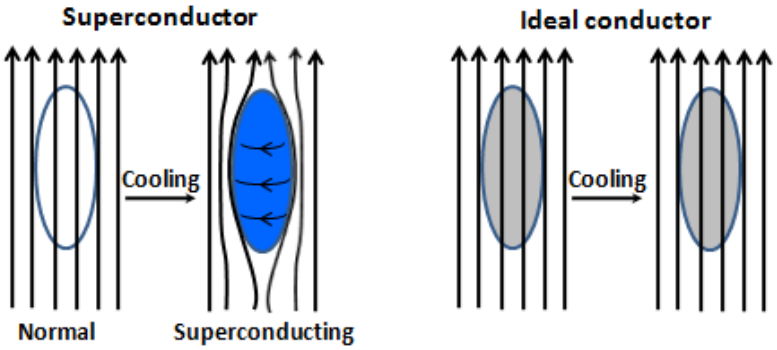

FIG. 1.1. Illustration of Meissner Effect under field cooling condition.

In an ideal conductor, the flux inside it cannot change, i.e.

$$dB/dt=0 \qquad (1.1)$$

Whereas in a superconductor, the field is always zero, i.e.:

$$B=\mu_0(H+M)=0 \qquad (1.2)$$

In the zero field cooling case, the behaviours of an ideal conductor and a superconductor are identical. Whereas in field cooling, the superconductor expels the field and has a magnetic susceptibility of χ=-1 (this is only true for type-I superconductors and type-II superconductors in Meissner state, with a demagnetization factor of 0), but ideal conductor traps the field.

To be a superconductor, the material should have both ideal conductivity and ideal diamagnetism under a critical field.

1.2 Classification of superconductors

Superconductors can be classified in different ways. According to their critical temperature, superconductors can be classified as low-T_c superconductors and high-T_c superconductors. Based on the magnetization behaviour, superconductors can be classified as type-I superconductors and type-II superconductors.

1.2.1 Low-T_c and high-T_c superconductors

In 1911, when Onnes firstly discovered superconductivity, the T_c of mercury is only 4.2K. Owing to the persistent effort by researchers, superconductors with higher critical temperatures have been continuously discovered during the last century. Fig. 1.2 shows the discovery history of some important superconductors [3]. In 1986, A. Muller *et al*. discovered Lanthanum-barium-copper oxide ceramic ($LaBaCuO_4$) [4]. The T_c of $LaBaCuO_4$ is 30K, which is a benchmark temperature to classify superconductors. A superconductor is defined as a low-T_c superconductor if its T_c is below 30K, otherwise it is defined as a high-T_c superconductor.

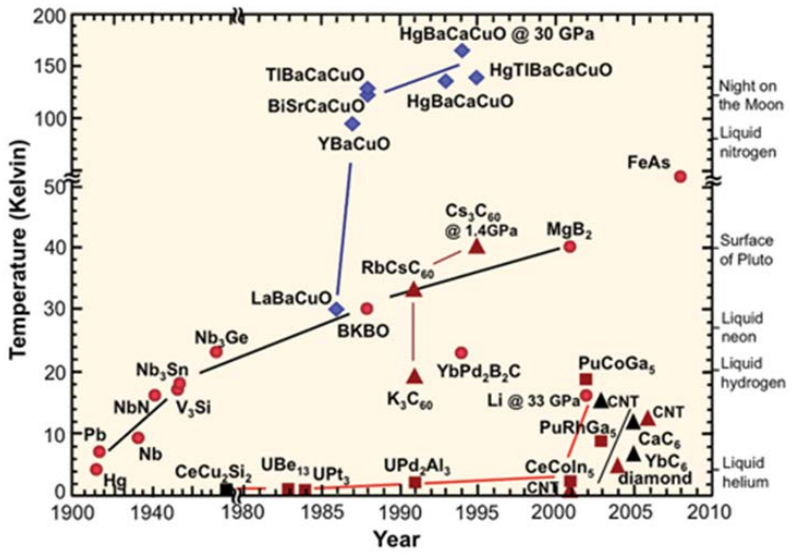

FIG. 1.2. The development history of superconductors [3].

Low-T_c superconductors are normally metals, alloys, and some compounds, among which NbTi and Pb_3Sn are most popular. High-T_c superconductors are normally compounds, in which copper oxides, such as BiSrCaCuO and YBCO are commonly used.

1.2.2 Type-I and Type-II superconductors

As described in Section 1.1, to be a superconductor, the material should have a Meissner state. But with the increase of external field, different superconductors have different behaviours. Some superconductors will directly enter a normal state. This type of superconductors is called type-I superconductors. Some superconductors will enter a mixed state before returning normal. This type of superconductors is called type-II superconductors. The schematic phase diagram of type-I and type-II superconductors is shown in Fig. 1.3.

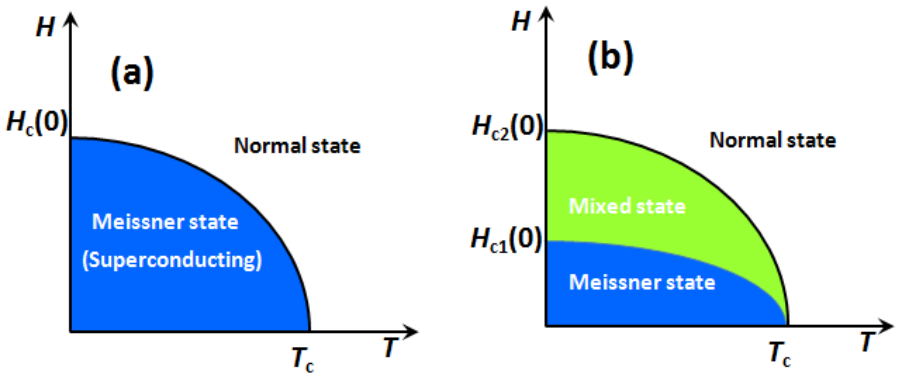

FIG. 1.3. Phase diagram of type-I and type-II superconductors. (a) type-I superconductors only have one critical field H_c, below which the material is superconducting, otherwise it is normal. (b) type-II superconductors have a lower critical field of H_{c1} and an upper critical field H_{c2}. Below H_{c1} the material is in Meissner state; between H_{c1} and H_{c2} the material is in a mixed state; above H_{c2} the material is normal.

Specifically, as shown in Fig.1.4 [5], type-I superconductors remain perfectly diamagnetic until the external field (in the thesis, both the field intensity H and flux density B are called "field" for short, if there is no confusion) exceeds the field B_c ($\mu_0 H_c$). After the external field exceeds B_c, the superconductors suddenly enter a normal state. The magnetization drops to zero, and the field fully penetrates the material. In this case, the external field is equal to the field in the material. B_c is defined as the critical field of type-I superconductors. Type-I superconductors are mainly metals and alloys, such as Hg and Sn.

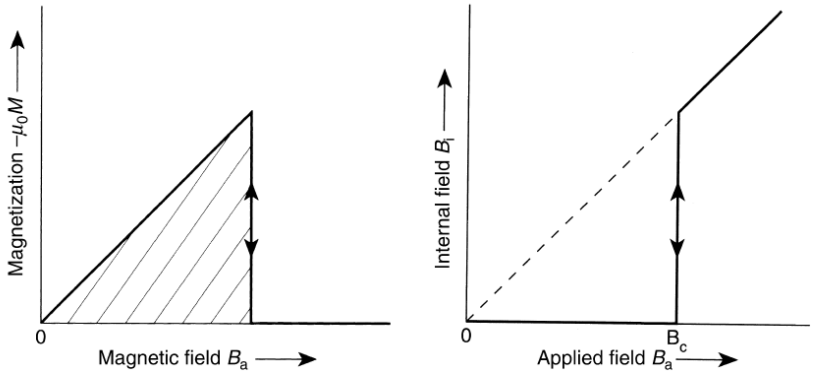

FIG. 1.4. The magnetization characteristics of type-I superconductors [5].

The magnetization curves of type-II superconductors are shown in Fig.1.5 [6]. Type-II superconductors remain in Meissner state until the external field exceeds the lower critical field B_{c1} ($\mu_0 H_{c1}$). With further increase of the external field, the superconductor will be gradually penetrated from the outer to the inner (will be discussed later). This state is defined as a mixed state, where the susceptibility is between -1 and 0. The superconductor enters a normal state if the external field exceeds the upper critical field B_{c2} ($\mu_0 H_{c2}$). Type-II superconductors are normally alloys and compounds, which normally have a much higher upper critical field [7].

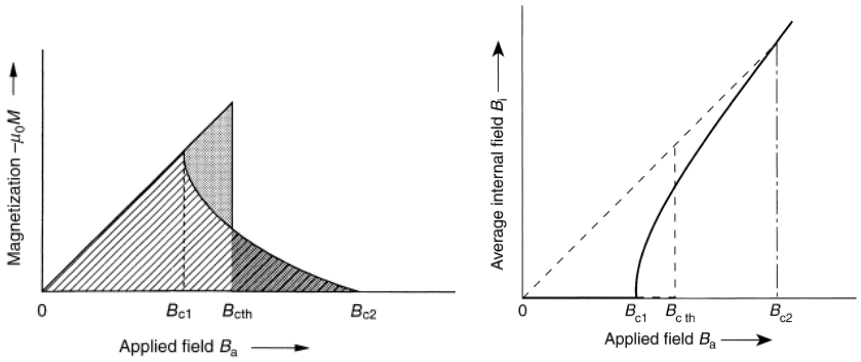

FIG. 1.5. The magnetization characteristics of type-II superconductors [6].

The difference between type-I and type-II superconductors can be explained by Ginzburg-Landau theory, which was proposed by Ginzburg and Landau in 1950 [8].

The theory is based on Landau secondary transition theory. By minimizing the free energy in a superconductor, two GL equations are obtained, and two important length scales are defined [9]. The first is called coherence length, denoted by ξ. The coherence length describes the distance near the boundary of a normal material and a superconductor, in which the super electrons' (Cooper pairs [10]) density increases from zero (in normal material) to a constant value far inside the superconductor. The second is called penetration depth, denoted by λ. It describes the length scale with which external magnetic field B decays exponentially to zero inside a superconductor. The Ginzburg-Landau parameter κ is defined as [9]:

$$\kappa = \frac{\lambda}{\xi} \qquad (1.3)$$

A superconductor can then be classified as a type-I superconductor if $\kappa < 1/\sqrt{2}$, otherwise it is classified as a type II superconductor, as shown in Fig. 1.6. From GL equations, the relation between B_{c1} and B_{c2} can be obtained as [9]:

$$\begin{cases} B_{c1} = \dfrac{B_{cth} \ln \kappa}{\sqrt{2}\kappa} \\ B_{c2} = \kappa\sqrt{2} B_{cth} \end{cases} \qquad (1.4)$$

Where B_{cth} is the thermodynamic critical field, indicated in Fig. 1.5.

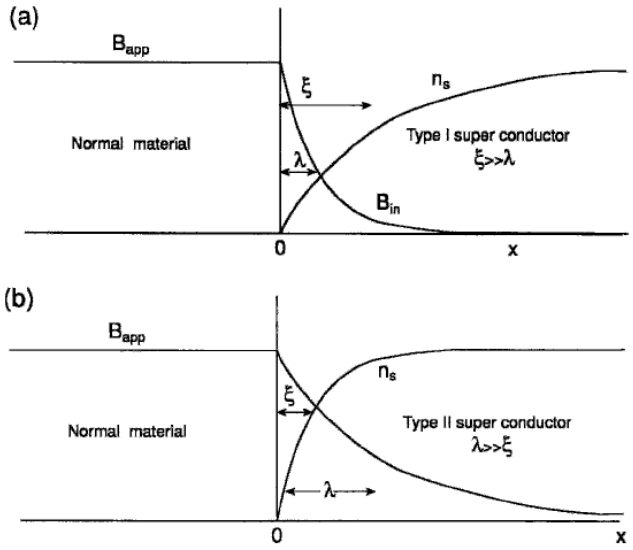

FIG. 1.6. Increase in the number of super electrons n_s and decay of the magnetic field B_{app} with distance x from the surface of the superconductor [9]. The coherence length and penetration depth are shown. (a) Type I superconductor, with $\lambda << \xi$; (b) Type II superconductor, with $\xi << \lambda$.

1.3 Magnetic field and transport current in type-II superconductors

1.3.1 Flux pinning and critical current

It has been shown that when a magnetic field B_{app} penetrates type-II superconductors they are then in the mixed-state. As proposed by Abrikosov [11], the flux in superconductor is in the form of tubes, named vortices. Each vortex has a core in which the flux lines go through, and screening currents flow around the core, as shown in Fig. 1.7 [12]. The core has a radius of ξ, which is the coherence length. In the core region, the density of super electrons is very low, so it can be considered as normal. The radius of screening current is the penetration depth λ, within which the current density decreases exponentially. According to Ginzburg-Landau theory, each vortex contains a flux quantum Φ_0. If the penetration depth is significantly larger than

the coherence length, the macroscopic flux density in the superconductor can be considered proportional to the density of vortices [12]:

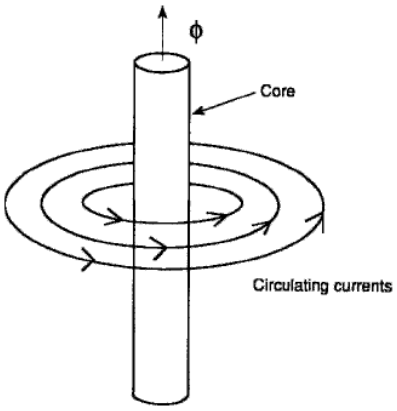

FIG. 1.7. Sketch of shielding currents circulating around a vortex core [12].

$$B_{\text{in}} = N_A \Phi_0 \qquad (1.5)$$

Where N_A is the number of vortices per unit area.

If two vortices are close to each other, there will be a Lorentz force between the screening current of a vortex and the magnetic flux of the other vortex. The Lorentz force per unit length is:

$$\boldsymbol{f}_2 = J_1 \times \boldsymbol{\Phi}_0 \qquad (1.6)$$

Where J_1 is the super current density of vortex 1 at the position of vortex 2, as shown in Fig. 1.8 [13]. This force is repulsive. In an ideal type-II superconductor, the vortices assume the arrangement that will keep them furthest apart, as illustrated in Fig. 1.9.

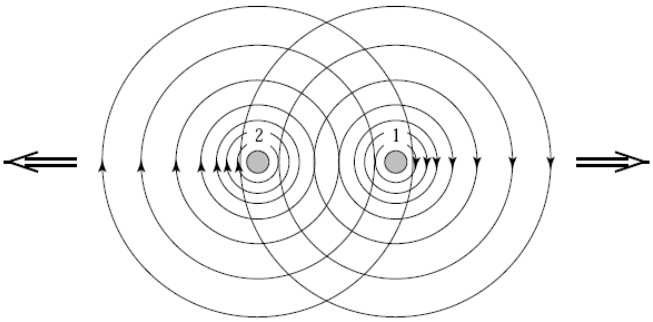

FIG. 1.8. Sketch of repulsive forces between two adjacent vortices [13].

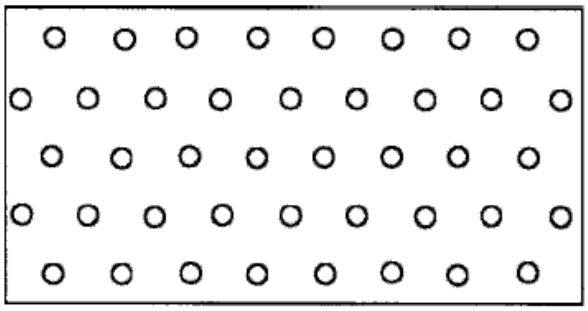

FIG. 1.9. Two-dimensional hexagonal lattice of vortex cores [14].

Macroscopically, if an ideal type II superconductor in the mixed state is transporting current, there will be an average Lorentz force between the transport current and vortices:

$$\boldsymbol{F}_L = \boldsymbol{J} \times \boldsymbol{B} \qquad (1.7)$$

Since the transport current is spatially fixed by the boundaries of the superconductor, the vortices have to move perpendicular to the current direction under the Lorentz force. This flux motion generates an electric field which shares the same direction with the transport current, indicating a resistance. Therefore an arbitrarily small transport current would generate a loss in an ideal type-II superconductor. In practical applications, however, it is known that type-II superconductors can transport a large current without loss. This is achieved by flux pinning [15-17], which fixes the

vortices and prevents motion of the flux. If a type-II superconductor contains impurities or crystal defects, etc., less energy is needed to form vortices in these positions (referred as pinning centres). Certain amount of vortices is pinned in the pinning centre. Because the existence of mutual repulsive forces among vortices, all vortices can be pinned in the superconductor by a few pinning centres. The pinning strength acting on individual vortices presents a macroscopic average pinning force F_p. If the pinning force is larger than the Lorentz force F_L, vortices in the superconductor cannot move, and current can flow without dissipation. The critical current density J_c in the superconductor can be considered as the value from which:

$$\boldsymbol{F}_P = \boldsymbol{F}_L = \boldsymbol{J}_c \times \boldsymbol{B} \qquad (1.8)$$

If the pinning force is strong, it is defined as a hard superconductor, otherwise it is defined as a soft superconductor.

1.3.2 Critical state model of Type-II superconductors

The Meissner state is entirely reversible, i.e. when the field is removed the currents die away. In the mixed state of type-II superconductors the situation is different. The critical state model is a very important tool to understand to magnetization in type-II superconductors. The model describes the current-field distribution in the mixed state of type-II superconductors. It assumes that a type-II superconductor is always in critical state, i.e. current density in the superconductor J is always its critical current density $\pm J_c$ or zero, and the curl of magnetic field is equal to J_c. The electric field (where there is electric field) E is always in the same direction as J. When a low current or field is applied to a superconductor, a current with critical current density will flow in the outer part. This current shields the inner part of the superconductor and there the B field and the current are zero.

According to different assumptions on critical current density, there are two most commonly used models: Bean model and Kim-Anderson model.

(a) Bean model

The Bean model [18] was firstly proposed by Bean in 1962. It assumes that in a hard superconductor, there are only three possible values for current density, 0, and $\pm J_c$. In the absence of flux J=0, otherwise it possesses a value of J=$\pm J_c$. The Bean model is a very simple but powerful tool to understand the magnetization of a hard superconductor under zero-field cooling and field cooling.

Assume a slab-like superconductor which is infinite long in y and z direction, and the length in x direction is $2a$. The field is applied in z direction, as shown in Fig. 1.10. According to Ampere's Law:

$$\nabla \times \boldsymbol{B} = \mu_0 \boldsymbol{J}_c \qquad (1.9)$$

In the proposed one-dimensional geometry, Eq.1.9 can be simplified as:

$$\frac{dB}{dx} = \mu_0 J_c \qquad (1.10)$$

Therefore, the penetration depth x is proportional to applied field intensity, and the gradient of the field (where there is field) is constant.

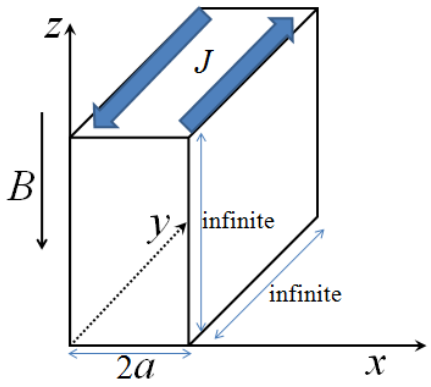

FIG. 1.10. Geometry of an infinite long slab subjected to homogenous external field.

Fig. 1.11 shows the zero-field cooling magnetization process of the above mentioned geometry under Bean model. In the beginning, when the applied field intensity is small, the field penetrates the outer part of the superconductor. With the increase of applied field, the superconductor is further penetrated. When the applied field reaches the value of $H_p=aJ_c$, current has reached the centre of the superconductor. Further increase in the field does not change the current distribution, but increases the field in the superconductor. When the applied field is decreased, the current in the outer part changes direction. After the field is removed, a field is trapped in the superconductor. In zero-field cooling case, if a maximum field of H_p in the centre of the superconductor is to be trapped, at least a field of $2H_p$ should be applied. Fig. 1.11(c) shows the superconductor with applied field over $2H_p$ and Fig. 1.11(e) shows the field distribution when the applied field has returned to zero.

In contrast, Fig. 1.12 shows field cooling process. Initially, the field in the whole superconductor has a homogeneous value of H_p, but no current exists in the superconductor. With the decrease of the external field, a current is induced in the outer part of the sample. When the field reduces to zero, a field of H_p is trapped in the centre of the superconductor. Therefore, to trap a field of H_p, field cooling only needs a minimum applied field of H_p.

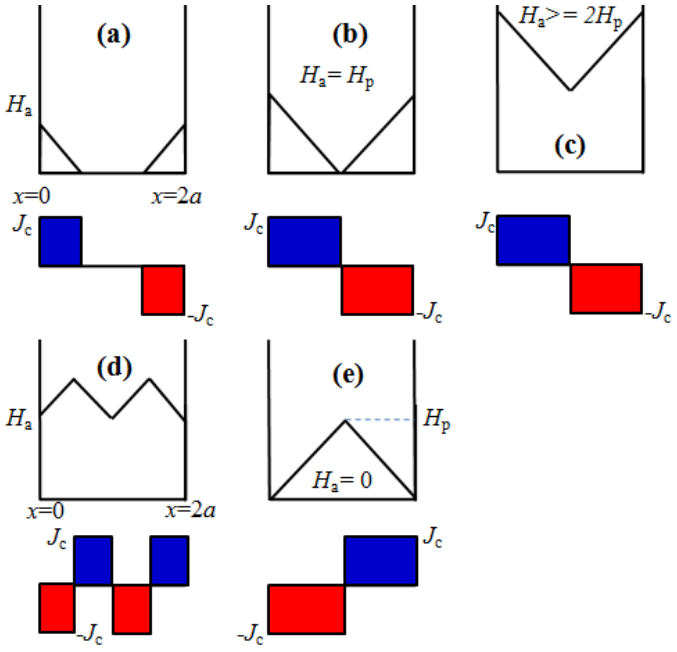

FIG. 1.11. Magnetization process of type-II superconductor in zero field cooling under Bean model. The applied field H_a increases monotonously from zero to over $2H_p$, and then reduces monotonously to zero.

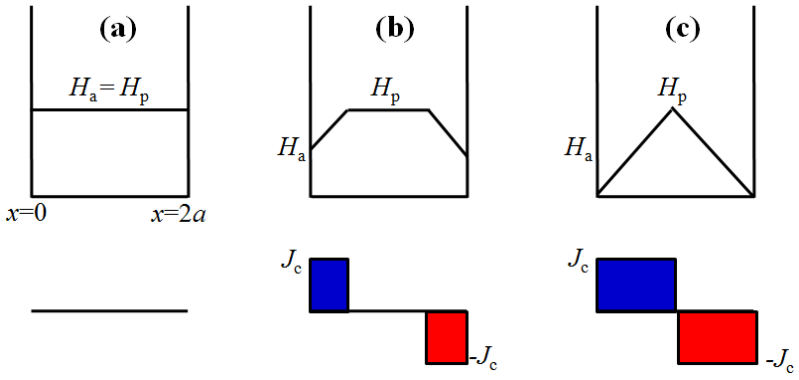

FIG. 1.12. Magnetization process of type-II superconductor in field cooling under Bean model. The initial applied field is H_a, and it reduces monotonously to zero.

(b) Kim-Anderson Model

Unlike the Bean model, the Kim-Anderson model assumes that the critical current density depends on the local field intensity. Among many forms of the field-critical relationships, the most commonly used equation is [19-21]:

$$J_c(B) = \frac{J_{c0}}{1 + B / B_0} \qquad (1.11)$$

Where J_{c0} is the critical current density with no applied field, and B_0 is a constant. Eq. 1.11 is normally referred to as the Kim-Anderson model.

1.3.3 Flux creep, flux flow, and *E-J* power law

In the critical state model, the superconductor is considered ideally stable, so that there is no loss in DC field or DC transport current when $J \leq J_c$. In practical case, when $T > 0$, especially for HTS materials which operate at a higher temperature, vortices may "creep" out of the pinning centre [22-25]. For $J \geq J_c$, the Lorentz force exceeds the pinning force, forcing the vortices to flow [25]. In both cases, the vortices' motion induces an electric field in the superconductor. The flux creep and flux flow characteristics can be macroscopically described by *E-J* power law [26]:

$$E = E_c \left(\frac{J}{J_c}\right)^n \qquad (1.12)$$

Where E_c is a constant, which is usually set as $10^{-4} V/m$ to experimentally determine critical current density of superconductors. The *n*-value in Eq. 1.12 varies with material as well as temperature. The critical state model is a specific case of Eq. 1.12, in which *n* is equal to ∞.

1.3.4 AC loss in type-II superconductors

According to critical state model, when the superconductor is transporting a direct current and (or) under a DC magnetic field, there is no loss in the superconductor.

However, when the superconductor is transporting an alternating current and (or) under an AC field, the situation is different. The change in transport current or external magnetic field gives rise to the magnetic field redistribution inside the superconductor. Flux motion inside the superconductor induces an electric field E according to Faraday's Law. Because electric field is always in the same direction as the current density J inside the superconductor, there is loss which is described as:

$$Q = \int_V EJdV \qquad (1.13)$$

Where Q is the total loss in the superconductor, and its unit is Watt. V denotes the whole superconducting domain. The loss caused by transporting an alternating current is defined as a transport loss, and the loss caused by external ac field is defined as magnetization loss [27]. Both of these losses occur when a superconductor transporting an alternating current is subjected to an external ac field.

1.4 Conclusion

This chapter introduces the fundamental knowledge of superconductors. Superconductors are the kind of materials which have perfect conductivity and ideal diamagnetism. According to their critical temperature, superconductors can be classified as low-T_c and high-T_c superconductors. According to the critical field, superconductors can be classified as type-I superconductors and type-II superconductors. As type-II superconductors are closely related to this thesis, flux pinning theory, critical state model, and E-J power law of type-II superconductors are introduced.

Chapter 2

Introduction to Flux Pumping Technologies for Superconducting Magnets

2.1 Superconducting magnets and flux pumps

2.1.1 Superconducting magnets

Superconductors are capable of transporting a direct current of high density with little Joule loss. This excellent property makes superconductors ideal for high field magnets. Superconducting magnets have been widely used in various areas such as Magnetic Resonance Imaging (MRI) [28, 29], Nuclear Magnetic Resonance spectroscopy (NMR) [30, 31], magnetic levitation systems [32-34], etc. Higher magnetic field provides MRI/NMR with a higher resonance frequency, a higher resolution, better-defined chemical shift spectra, and a larger data acquisition rate [30]. Low-T_c superconductors such as NbTi and Nb_3Sn normally have a much lower upper critical field B_{C2} than high-T_c superconductors, as shown in Fig. 2.1 [35].

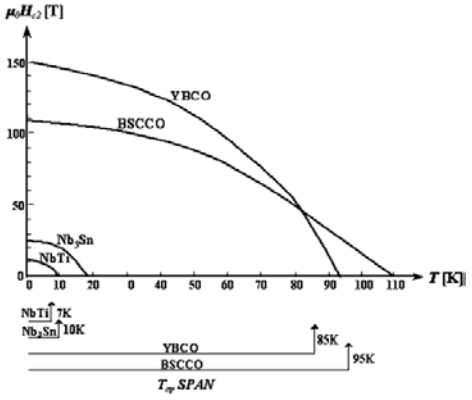

FIG. 2.1. Upper critical field VS temperature of low-T_c superconductors and high-T_c superconductors [35].

Low-T_c superconductors are cheaper, easier to handle and provide sufficient field for applications such as MRI. Therefore, in commercial MRI, NbTi continues to be widely used to generate the background field. Fig. 2.2 shows the development history of MRI. MRI for humans is limited to 3T, and the higher fields are usually used for animal experiments.

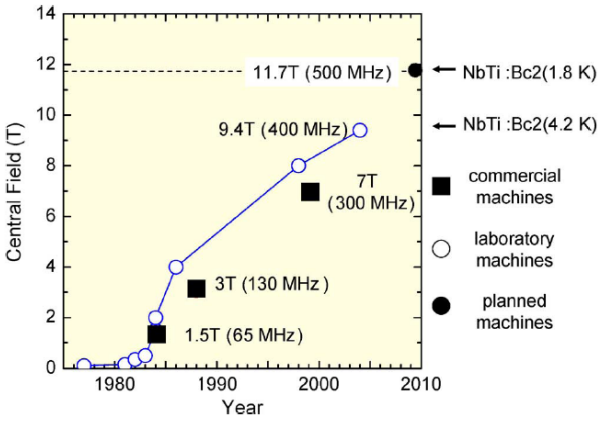

FIG. 2.2. Development of MRI [28].

In NMR, the field strength used is generally higher than that in MRI to achieve a higher resonance frequency. To date, 900MHz NMR which requires 20T is quite common and Nb_3Sn is capable of generating this field. But for 1.3GHz NMR, a field of over 30T is required which exceeds the upper critical field of Nb_3Sn. In this case, high-T_c superconductors are essential. The current design is using an LTS magnet to generate a background field (>20T) in its bore, and using an HTS magnet as an insert to generate an extra field of over 10T [30].

Superconductors are also enabling in providing extremely high magnetic field for research proposes. Researchers in National High Magnetic Field Lab (NHMFL) in the USA recently reported that they had achieved a persistent 42.5T field using a resistive-HTS hybrid magnet [36]. This is not the limit for HTS though and their next goal is to build a 60T fully superconducting magnet.

2.1.2 Persistent current operation of superconducting magnets

To generate strong magnetic field in superconducting magnets, superconductors need to transport a large current. One way to power superconducting magnets is to use external power supplies and current leads [37]. The power supply feeds a constant current to the magnet via a pair of current leads. There are several drawbacks of this approach. The first is that the constant current generates continuous loss in current leads. The second is that the field stability is limited by the stability of the power supply which is hard to improve. In applications like MRI/NMR, the field stability has to be 0.1ppm/h or higher, which cannot be achieved by external power supplies. Therefore, In MRI/NMR, the LTS magnet normally works in persistent current mode [38]. As shown in Fig. 2.3, the magnet is shorted by a persistent current switch [38-40]. In charging the magnet, the superconductor in the switch is firstly driven normal by heating it over its critical temperature. A voltage is then developed across the switch to charge the magnet. After the magnet is fully charged, the superconductor in the switch is cooled to be superconducting again. The joint resistance in LTS persistent current switches can be manufactured in the order of $10^{-13}\Omega$ [41, 42]. Therefore the transport current can flow in the magnet with nearly no decay. The persistent current operation enables LTS magnets to generate extremely stable magnetic field, which is essential for NMR/MRI.

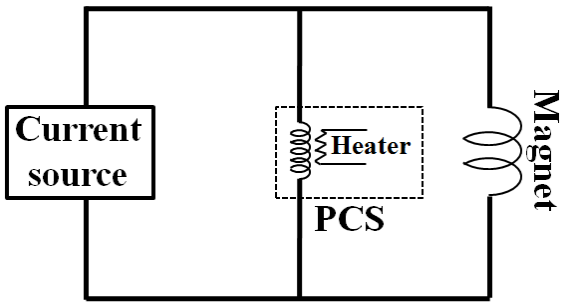

FIG. 2.3. Circuit of persistent current switch-superconducting magnet system. The PCS is driven normal by a heater in order to charge the magnet. After the magnet is fully charged, the

superconductor in the PCS is cooled down to be superconducting, allowing a persistent current flowing in the magnet.

2.1.3 Flux leakage in closed HTS magnets and flux compensation by flux pumps

Ideally HTS magnets should also operate in persistent current mode. However, several problems have to be solved before they can work in persistent current mode.

Unlike low-T_c superconductors which are metals or alloys, high-T_c superconductors are typically compounds. High-T_c superconductors for magnets' use are normally manufactured as Coated Conductors (CCs) which have a multi-layer structure [43], as shown in Fig. 2.4. Apart from the thin superconducting layer, buffer layers, substrate, and copper stabilizer layers are indispensable.

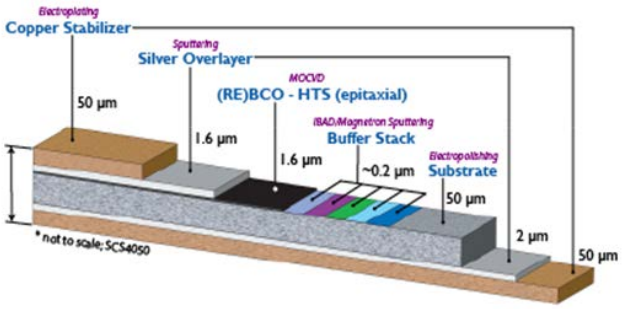

FIG. 2.4. Structure of *Superpower* coated conductor [43].

A low resistance joint in CCs is difficult to achieve because the existence of the non-superconducting layers. The value of joint resistances between CCs is commonly tens of nano-ohm [44], which is too large for persistent current operation. Although recent research [45] claims that a joint resistance of less than $10^{-17}\Omega$ between CCs is manufactured, no repeatable results have been shown, and even if it is true the manufacturing process is far too complicated for engineering use.

The other source of flux leakage is flux creep [23]. The flux creep will generate a transport loss in superconducting magnets. This phenomenon is quite eminent in high-T_c superconductors, resulting in a relatively low n-value [46].

Another source of flux leakage is that when a DC HTS magnet is in AC magnetic field, it will generate a significant transport loss [47-49]. This is the common case where the DC winding of a motor or generator is subjected to ripple field generated by the armature windings due to harmonics or mechanical vibration.

Flux pumps are capable of injecting flux into closed superconducting circuits without electrical contact. So they can be used to compensate the current decay in HTS magnets, making them operate in real persistent current mode, at the cost of insignificant loss.

Flux pumps can also be used to charge closed HTS magnets. In this way, external power supplies, persistent current switches, and thick current leads can all be saved. Thus the heat loss can be significantly reduced and the system can be much more compact. Flux pumping is a promising technology which may promote the wide application of HTS magnets, such as in MRI/NMR, motors/generators, levitation systems, etc.

2.2 LTS flux pumps

The flux pumping technologies [50, 51] for an LTS coil were developed several decades ago. Although LTS flux pumps are dispensable because of the availability of low resistance joints, to understand their physics is beneficial for developing HTS flux pumps.

Almost all LTS flux pumps share the same principle-that is to alternatively drive part of low-T_c superconductors (most commonly type-I superconductors, due to their

low critical field which is easy to exceed) normal. The circuit has been shown in Fig. 2.5 [52].

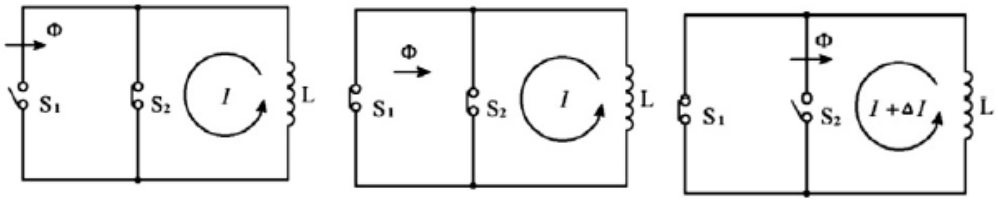

FIG. 2.5. Mechanism of LTS flux pumps [52].

S_1 and S_2 are LTS switches, and L is a superconducting load. When an amount of external flux Φ is approaching, S_1 is open and S_2 is closed, so that the load current I passes through S_2, as shown in the left figure. Then S_1 is also closed, Φ is trapped in the loop formed by S_1 and S_2. In the last step, S_2 is opened, so load current is forced to flow through S_1.Φ links the loop formed by S_1 and the load, thus resulting in a current increase ΔI in the load.

In the following part of this section, several specific LTS flux pumps are introduced.

2.2.1 A DC dynamo

One way to achieve the above mechanism is called a DC dynamo [50]. As shown in Fig. 2.6, the superconducting load is shorted by a type-I superconducting sheet. A magnet moves above the sheet. The field intensity is higher than the critical field of the sheet, so that when the magnet moves, a moving normal spot in the sheet can be created. The process can be explained by Fig. 2.5, in which the switches are created by the moving magnet.

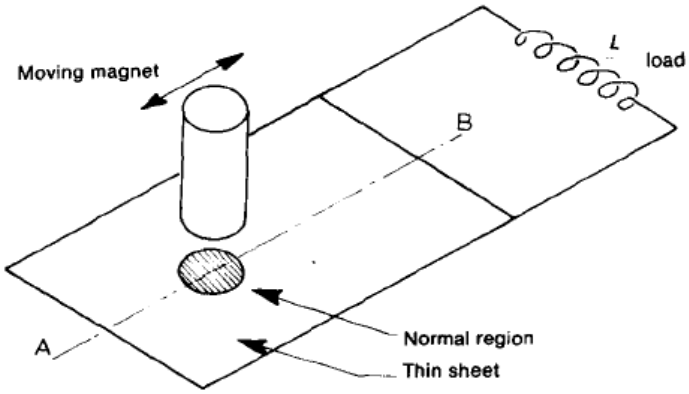

FIG. 2.6. Schematic drawing of a DC dynamo [50].

The moving normal spot can also be generated by multi-phase windings [53], as shown in Fig. 2.7.

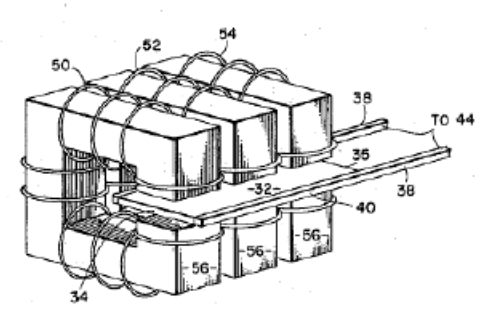

FIG. 2.7. Schematic drawing of a three-phase winding controlled DC dynamo [53].

Alternatively, the normal spot can be created by heating the superconductor above its critical temperature T_c. As shown in Fig. 2.8, a magnet and a laser spot are moving synchronically across a superconducting sheet; the lasers generate a moving normal spot to facilitate flux moving across the sheet [54].

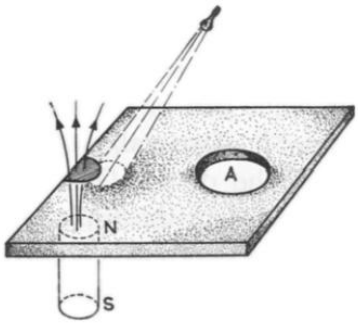

FIG. 2.8. Schematic drawing of a laser controlled DC dynamo [54].

2.2.2 Transformer rectifier flux pumps

A more direct way to achieve flux pumping is called a transformer rectifier flux pump [50, 51], which can be used in high current applications. The flux pump consists of a transformer and a rectifier. The transformer can be either with iron core or air core, and the rectifier can be either half bridge or full bridge. The flux pump works similarly to a normal transformer rectifier, as illustrated in Fig. 2.9. The transformer is used to generate a high alternating current in the secondary winding. The rectifier then converts this alternating current into a direct current. In the flux pump, two or more superconducting switches (1 and 2 in Fig. 2.9(b) (c)) alternatively switch on or off, to perform as a rectifier. The key point is how to control the superconducting switches. The switches can be switched thermally, magnetically, or mechanically [51].

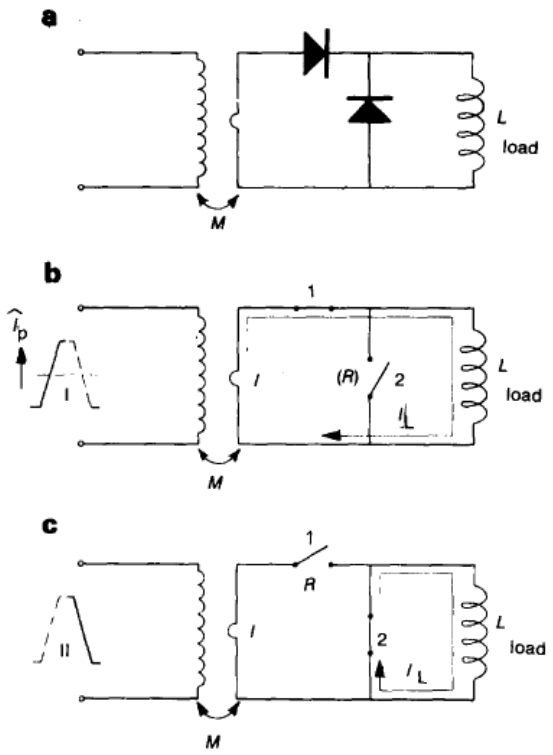

FIG. 2.9. Normal transformer rectifier and flux pump, (a) normal transformer rectifier, (b), (c), flux pump [51].

2.3 HTS flux pumps

Several HTS flux pumps have been proposed in recent years. These flux pumps are mostly based on travelling magnetic waves, although the devices generating the travelling waves are quite different from one another. This section reviews these existing flux pumps.

2.3.1 Heat actuated flux pump for HTS bulks

The technology of using a travelling magnetic wave to magnetize a bulk superconductor was originally put forward by Coombs [55-61] from University of Cambridge.

As shown in Fig. 2.10, a bulk of ferromagnetic material (Gadolinium) is placed in between an NdFeB magnet and an YBCO bulk. The permeability of the Gadolinium bulk can be changed by partially heating or cooling the material. Therefore, when a heat wave travels through the Gadolinium material, a magnetic travelling wave can be generated accordingly. The HTS bulk subjected to the travelling magnetic wave can be gradually magnetized.

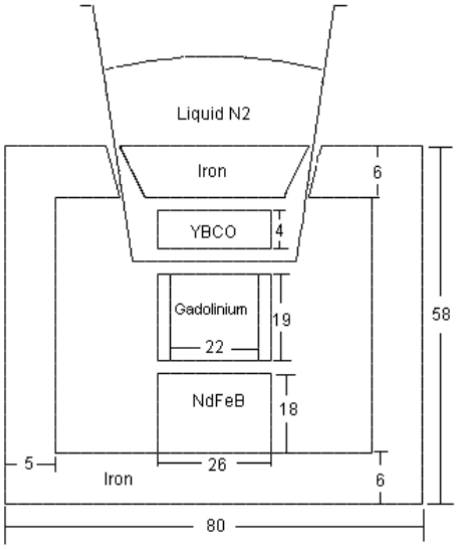

FIG. 2.10. Schematic drawing of heat actuated flux pump [57].

Although Coombs et al proposed using heat to generate the travelling wave this was chiefly because they were looking at magnetising bulks are compact and switching coils is not practical.

2.3.2 Rotating magnets based flux pump

Rotating magnets based flux pump [62-66] was firstly proposed by Hoffmann and coworkers [62]. The basic set up of Hoffmann's experiment is shown in Fig. 2.11. Several permanent magnets (NdFeB N38) are uniformly mounted to the circumference of two discs which can be driven by a motor shaft. One or more 2G superconducting wires are placed beneath the discs, where the wires are aligned

parallel with the shaft. Two ends of each 2G superconducting wire are soldered to a SC coil to form a closed loop circuit. When the magnets rotate above the 2G wire, a DC voltage will appear across the 2G wire, thus gradually ramping up the current in the superconducting coil to a high value, as can be seen from Fig. 2. 12.

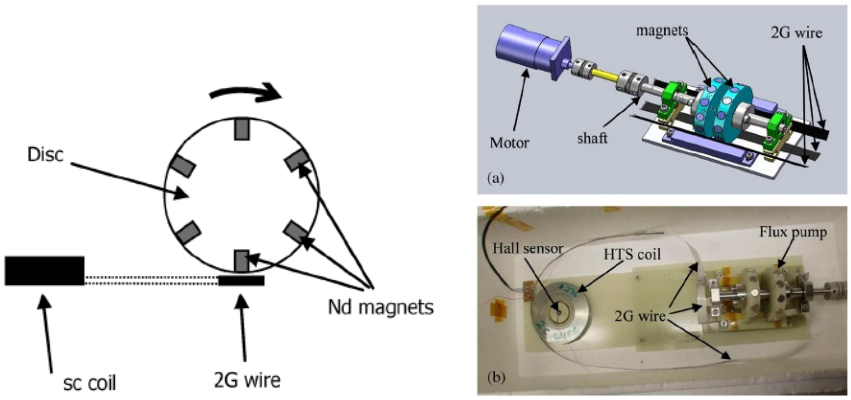

FIG. 2.11. Hoffman's flux pump [62]. Left: schematic drawing. Right: Device drawing and picture.

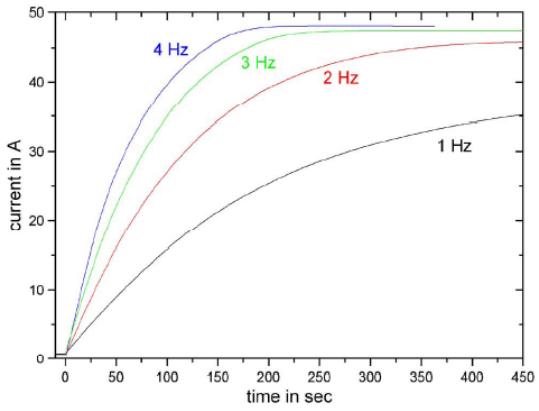

FIG. 2.12. Load current curves in Hoffmann's flux pumping experiment [62].

The flux pumping method has been successfully applied to magnetize a 2T NMR relaxometry magnet. The magnet can be pumped up to a field of 2T in 2.5 hours [63].

Hoffmann's work has drawn broad attention and has been followed by many researchers. Researchers from VUW [67] measured the output voltage-current curves of a rotating magnets based flux pump. They discovered that the final achievable load current was limited by a resistance which was two orders higher than the joint resistance in the circuit. They attributed this resistance as a dynamic resistance [67]. Many influential factors of the flux pump have been investigated, such as the influence of flux gap [68], the influence of operating frequency [69], the influence of stator wire width [70], the influence of magnets' geometry [71]. A through wall excitation system [72] was also developed, showing that the flux pump can be removed from the cryogenic system. The work makes flux pump more practical. The researchers from VUW and their cooperators have been focusing on developing 10MW class superconducting wind turbines with the flux pump as an exciter [73, 74].

In terms of the mechanism of the flux pump, Hoffmann provided an explanation [62]: when the magnets go across the wire, flux will be 'dragged' across the wire if the magnetic field is strong, and flux will be expelled by the wire if the field is weak; since the field is inhomogeneous in space, a net among of flux can be 'dragged' across during each magnet goes across the wire. Reference [75] gave a more specific explanation: screening current follows the position of the magnet; when magnets rotates, the relative position between the magnet and the CC changes, which changes the forward path and backward path of the screening current, thus resulting in a rectifying effect.

2.3.3 Linear-type flux pumps

HTS linear-type flux pump was firstly achieved by Nakamura [76]. Yet, in his work, a MgB2 sheet is partly driven normal, therefore this is actually not different from an LTS flux pump. Bai [52, 77, 78] uses an electromagnet to generate linear travelling magnetic wave. As shown in Fig. 2.13, the flux pump consists of an iron yoke which has several poles, and copper windings. The iron poles are linked by copper windings.

The windings are powered sequentially by alternating current so that a travelling magnetic wave can be generated in the gaps of the poles. An HTS slice which shorts a superconducting coil is put into the gap. When the slice experiences travelling magnetic field the load connected to the slice can be gradually energized.

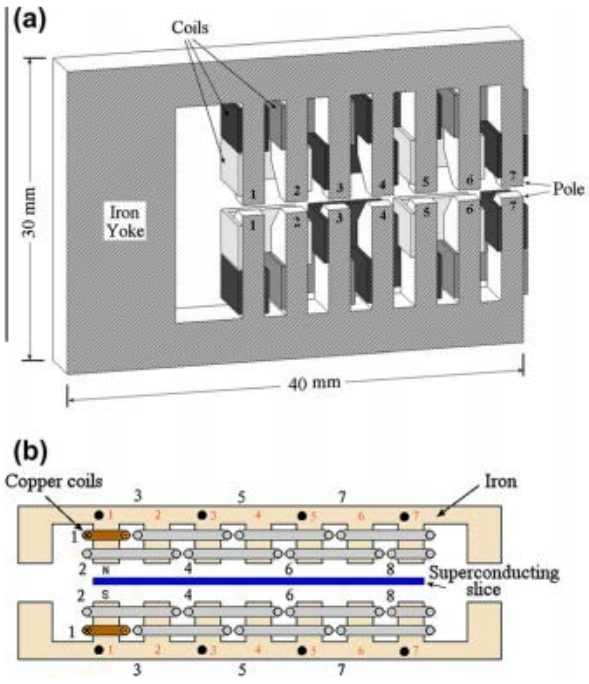

FIG. 2.13. Schematic drawing of Bai's flux pump [52], (a) three dimension view (b) a profile view.

Fu and coworkers [79-81] developed a linear flux pump which is similar to Bai's flux pump. The difference is that several parallel tapes instead of an entire slice are used as the stator to be subjected to travelling magnetic wave.

Although these flux pumps are able to inject flux into superconducting circuits, no convincing explanation on their mechanism has been proposed. In Bai's work [52], they explain the mechanism as the travelling magnetic wave generates a moving normal spot in the superconducting slice, which is the same as LTS flux pumps. The

explanation ignores the fact that the field magnitude in their experiment is far too low to break superconductivity of the HTS slice.

2.3.4 Transformer-rectifier flux pump

Oomen and coworkers [82] proposed an HTS transformer-rectifier flux pump, which is the same as an LTS transformer-rectifier flux pump from circuit point of view. As shown in Fig. 2.14, a transformer generates high alternating current in its secondary winding, and the alternating current is rectified by two switches S1, S2, thus generating a direct current in the load. Oomen proposed two ways of controlling the switches; the first is using superconducting switches controlled by heat, and the second is using power electronic components as switches. Although this flux pump is able to inject flux very fast, it has some drawbacks. The first is that the heat controlled superconducting switch generate great loss, and the second is that the power electronic components has a high on-state resistance, which means the flux leakage in the load loop is very fast.

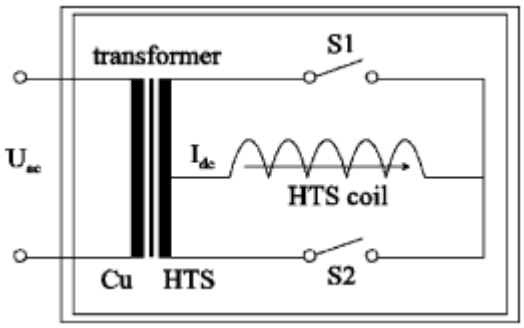

FIG. 2.14. Schematic drawing of Oomen's flux pump [82].

Because flux injection in this flux pump is achieved not merely using magnetic field, technically it is not a flux pump. Therefore this thesis will not discuss it in detail.

2.3.5 A circular-type magnetic flux pump for HTS films

A circular-type magnetic flux pump (CTMFP) was proposed by Wang and coworkers [83] to magnetize HTS films. The idea of a CTMFP is a combination of linear-type flux pumps and heat actuated flux pumps. As shown in Fig. 2.15, the windings of CTMFP are placed concentrically rather than linearly. A circular shape travelling magnetic wave can be generated in space, as depicted in Fig. 2.16. The wave can travel inward or outward depending on the phase difference of the windings.

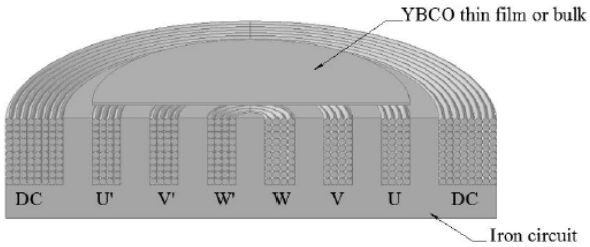

FIG. 2.15. Schematic drawing of CTMFP [83].

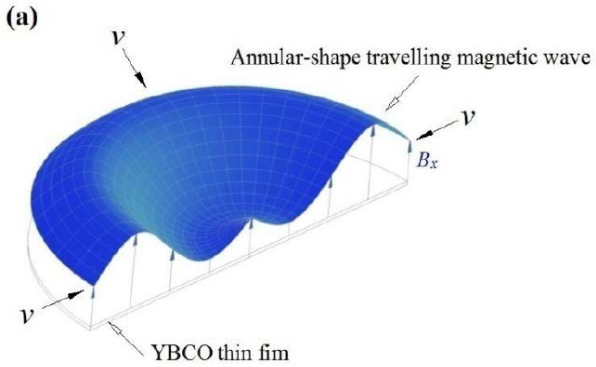

FIG. 2.16. Schematic drawing of travelling wave which can be generated by the CTMFP [83].

The experimental results from Wang show that the magnetization profile of a 2-inch diameter YBCO film under travelling magnetic wave is different from Bean's mode which bases on the assumption of homogeneous AC magnetic field.

2.4 Problems remaining in HTS flux pumps

Although existing flux pumps have been able to inject flux into HTS circuits, there are still several problems remaining to be solved.

The first is the mechanism of travelling wave flux pumps is unclear. How flux could travel across an HTS sheet without breaking superconductivity is mysterious. And it seems against Faraday's Law that an AC magnetic field induces a DC electric field in high T_c superconductors. Researchers have been struggling with the correct answer for many years.

The second problem is that the travelling wave flux pumps are not easily controllable and the performance cannot be exactly predictable. These flux pumps are more like a black box. It is impossible for using these flux pumps to make exact flux injection. So the field fluctuation is the load is considerable.

The third problem is that it is difficult to analyze or measure the loss in these flux pumps, let alone minimizing the loss.

2.5 Conclusion

This chapter briefly introduced the development of superconducting magnets, LTS flux pumps, and HTS flux pumps. It explained the practical engineering demands on HTS flux pumps, and summarized the existing problems in HTS flux pumps confronting researchers. This chapter proposed the motivation and importance of this work.

In the remaining chapters of this thesis, systematic and concrete studies are described which focus on revealing the physics of HTS flux pumps, developing new flux pumping devices, and improving flux pumping performances.

Chapter 3
Study on an AC Magnetic Field Controlled Persistent Current Switch

3.1 Introduction

Persistent Current Switch (PCS) [84-91] is an essential part for LTS magnets to operate in persistent current mode. As described in Section 2.2, the mechanism of LTS flux pumps is basically how to create and control superconducting switches. In the same way, if we can effectively control an HTS persistent current switch, we may also achieve flux pumping for high T_c superconductors. Therefore, it is reasonable to start research on HTS PCSs.

Existing PCSs can be classified as two types: heat controlled PCSs [84-88], and magnetic field controlled PCSs [90, 91]. Heat controlled PCS switches off by heating the superconductor to above its critical temperature. Heat controlled PCS can achieve a high switching off resistance, but the switching time is too long, normally several seconds or even longer [85]. Field controlled PCS operates by applying a field to drive the superconductor normal. A DC field with high intensity is commonly used in LTS PCS. For high T_C superconductors, however, it is difficult to drive them normal by DC field, because their upper critical field is rather high.

In this Chapter, the author proposes an idea that the dynamic resistance caused by AC magnetic field in type II superconductors could be useful in HTS PCS. The theory of dynamic resistance is introduced first, and then experiment aiming to verify the feasibility of the PCS is presented.

3.2 Dynamic resistance of type II superconductors

Dynamic resistance [92-94] appears when a high T_c superconductor carrying a direct current is subjected to an AC magnetic field perpendicular to current direction. The physics of the dynamic resistance is hysteresis magnetization behaviour of high T_c superconductors.

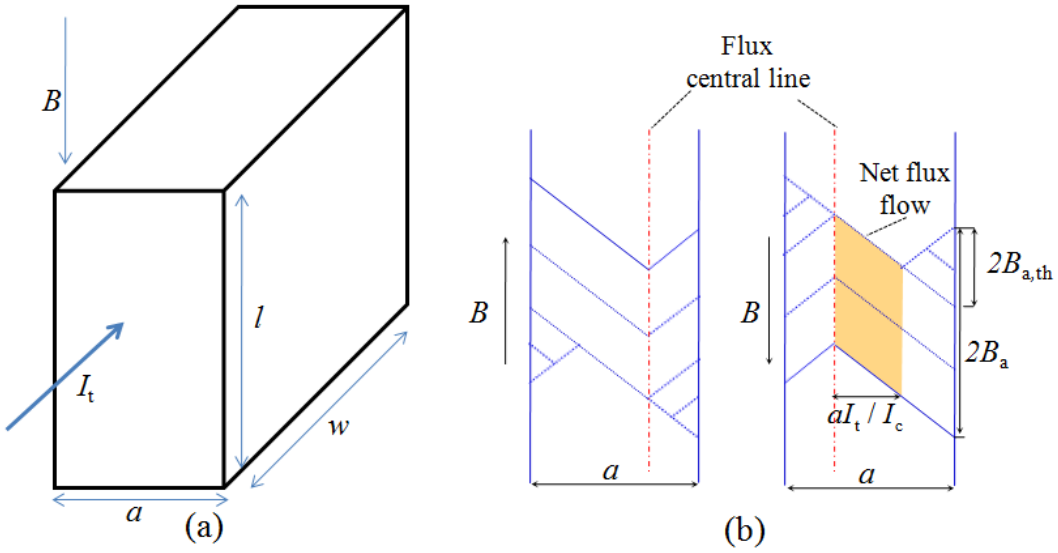

FIG. 3.1. Field profile inside a slab-like superconductor carrying DC transport current in AC magnetic field under Bean model. The DC transport current results in an asymmetric field profile in the slab.

As shown in Fig. 3.1(a), a slab-like type II superconductor carrying a direct current I_t is subjected to a perpendicular AC field B. The superconductor is with a width of a, the length of w, and a thickness of l, where $a<<w$, $a<<l$. When the field intensity is low, the field cannot reach transport current, the loss is pure magnetization loss. If the field intensity is high (the induced current together with transport current can occupy the whole superconductor), the situation is quite different. As shown in Fig. 3.1(b), when the field increases from the minimum to maximum, most flux enters the superconductor from the left edge of the superconductor; whereas when the field

decreases from the maximum to minimum, most flux exits the superconductor from the right edge. The red dash-dot lines in Fig. 3.1(b) are called the flux central line [94], which means no flux could move across (electric field equals to zero). These two lines are the boundary of transport current in the superconductor. During the field increasing and decreasing process, the position of flux central line changes, causing a net flux flowing across the superconductor. The shaded area in Fig. 3.1(b) shows the amount of flux flowing across the superconductor during each field cycle in per unit length. The total flux flowing across the superconductor can be expressed as:

$$\Phi_{\text{per\_cycle}} = 2(B_{\text{a}} - B_{\text{a,th}})aI_{\text{t}}w / I_{\text{c}} \qquad (3.1)$$

Where $B_{\text{a,th}}$ is the threshold field [92] as depicted in Fig. 3.1(b), and this value has to be overcome before the applied field can interact with the transport current. I_{t} is the transport current in the superconductor, and I_{c} is the critical current of the superconductor.

Because there is net flux flowing across the superconductor, according to Faraday's law, there will be a dc voltage generated across the superconductor which shares the same direction with the transport current. The dc voltage can be described as:

$$V_{\text{DC}} = f\Phi_{\text{per\_cycle}} = 2f(B_{\text{a}} - B_{\text{a,th}})aI_{\text{t}}w / I_{\text{c}} \qquad (3.2)$$

Where f is the applied field frequency. The voltage over the transport current is equal to the equivalent resistance:

$$R_{\text{dyn}} = V_{\text{DC}} / I_{\text{t}} = 2awf(B_{\text{a}} - B_{\text{a,th}}) / I_{\text{c}} \qquad (3.3)$$

This resistance is defined as a dynamic resistance.

For a superconducting thin sheet in which $a >> l$, the expression is slightly different, the analysis can be found in Brandt's paper [95]. Oomen [94] presented an analytical expression of the dynamic resistance under high applied field magnitude, which considers the field dependence of critical current density:

$$R_{dyn} = \frac{2awf}{I_{c0}}(B_a + cB_a^2) \qquad (3.4)$$

Where I_{c0} is the critical current of the superconductor without external field, and c is a factor describing the field-critical current relationship. With Bean's model, c is 0.

As shown in Eq. 3.4, the dynamic resistance is proportional to field frequency and positively related to field magnitude. It might be possible to use this property as an AC field controlled persistent current switch, which will be investigated in following sections.

3.3 Using an AC field controlled PCS to charge an HTS magnet

3.3.1 Experimental system

The whole system:

Schematic experimental system is depicted in Fig. 3.2. The system consists of a DC current supply, a closed YBCO load coil, an AC magnetic field controlled PCS, and a Hall Sensor. The picture of the system is shown in Fig. 3.3.

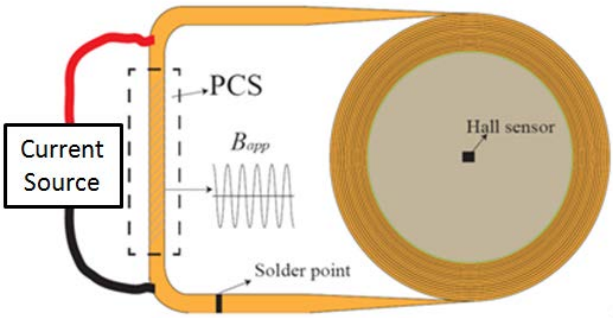

FIG. 3.2. Schematic drawing of the experimental system consisting of a power supply, an AC field controlled PCS, and a superconducting load. The left part represents the current supply and current leads, and the yellow strip represents YBCO tape.

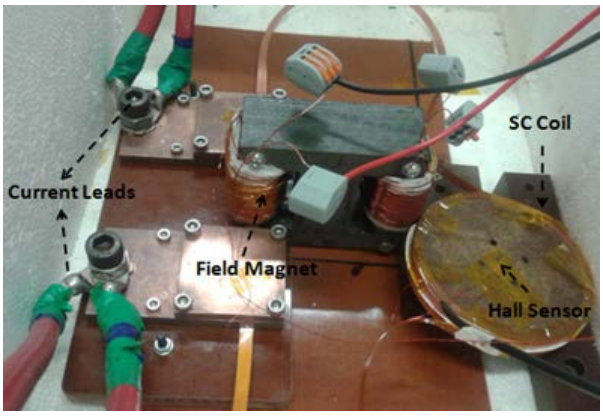

FIG. 3.3. Picture of PCS experimental system.

The Power supplies:

The current supply used to charge the coil is Agilent 6680A, which can output a current of 0-875A, and voltage of 0-5V. A KEPCO BOP 2020 power supply was used to power the electromagnet. The KEPCO was able to independently output a direct current, or amplify external DC or AC voltage signals. A function generator was used to control the KEPCO in the case of AC output.

The PCS:

The PCS was a portion of the YBCO tape in the coil loop, which was subjected to an AC field, as can be seen from Fig. 3.3. The tape was 6mm wide with copper stabilizer manufactured by *Superpower*. The AC field was generated by an electromagnet, which had an inductance of 36mH, as shown in Fig. 3.4. The magnetic circuit of the electromagnet was a transformer core, which was made of laminated steel and was cut to form a 1mm air gap. In the experiment, the portion of tape was put in the middle of the air gap. The winding of the magnet had 240 turns distributed in 4 layers. In between each two layers of the winding, there was a piece of paper tape for insulation.

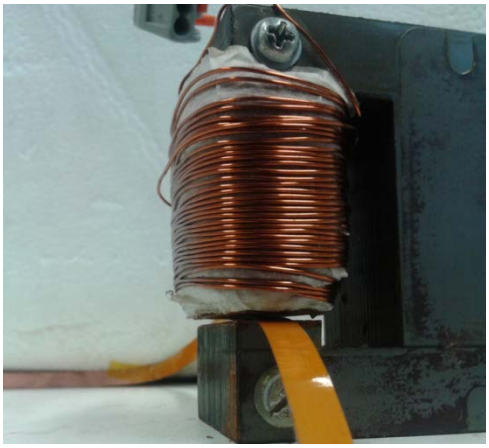

FIG. 3.4. Picture of the field magnet. It consisted of a laminated steel core, a copper winding, and an air gap. A portion of CC is also shown in the picture to exemplify how field was applied to the superconductor.

The cross section of the air gap in the electromagnet had a size of 35mm×12mm. As shown in Fig. 3.5, the field-current relationship was measured in 3 positions by a Gauss meter under direct current input condition. The result is shown in Fig. 3.6. The core behaved linearly up to 0.65T. After the current was removed, no residual field was observed in the air gap, indicating the hystersis of the laminated steel was negligible. In the following experiment, the current-field relationship in the centre of the air gap is used as a benchmark.

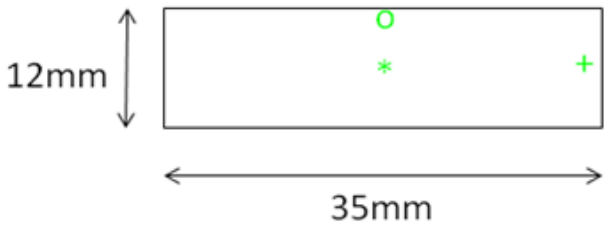

FIG. 3.5. Cross-section of the air gap and three field calibration points.

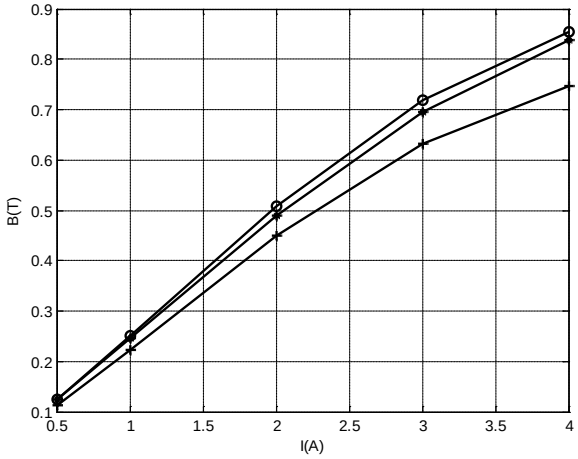

FIG. 3.6. Field-current relationship of the magnet measured at three positions in the air gap. The three symbols correspond to the three positions in Fig. 3.5.

The superconducting coil:

The double pancake coil was wound from *Superpower* 6mm wide YBCO Coated Conductor (CC), as shown in Fig. 3.7 [96]. The CC was insulated by wrapping a layer of Kapton tape. The two ends of the coil were soldered together by SnPb solder [44]. Specifications of the coil are shown in Tab. 3.1. The inductance of the coil was measured by an inductance meter before soldering the two ends together.

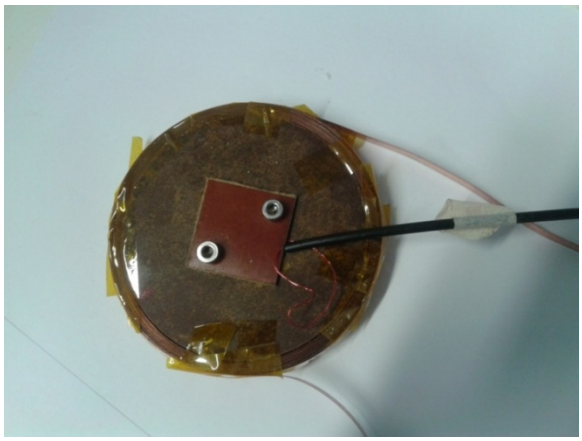

FIG. 3.7. Picture of the double pancake superconducting coil with a Hall sensor mounted in its centre.

TABLE 3.1SPECIFICATIONS OF THE COIL AND PCS

Tape type	*Superpower*6mm width YBCO tape
Tape I_c in air gap	123A@77K self-field
Coil I_c	81A@77K
Coil inner diameter	8cm
Coil outer diameter	8.9cm
Number of turns	40
Total Tape length	10.6m
Coil inductance	0.388mH
PCS conductor length	3.5cm
Tape insulation	Kapton tape

Signal sensing and acquisition system:

A Hall sensor was fixed in the centre of the coil to determine the transport current in the coil. The Hall sensor used in the experiment is shown in Fig. 3.8. It is able to sense magnetic field perpendicular to its surface, and to output a Hall voltage which is proportional to the magnetic field at a fixed current input. The sensor has four pins, two of which are for current input and the other two for voltage output. Because the output voltage also depends on the current input, a constant current source as shown in Fig. 3.9 was used to power the Hall sensor, and the input current was fixed at 14.7mA.

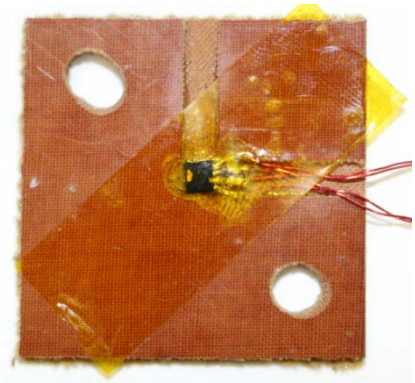

FIG. 3.8. Picture of the Hall sensor.

FIG. 3.9. Picture of the constant current source for the Hall sensor.

The Hall voltage was acquired by an NI-USB6002 DAQ card and recorded by LabVIEW Signal Express software. The sampling frequency was 1kHz. Before making the HTS coil as a closed circuit, the relationship between the transport current of the coil and the Hall voltage were calibrated, and the result is shown in Fig. 3.10. The ratio was approximately 1mV/A.

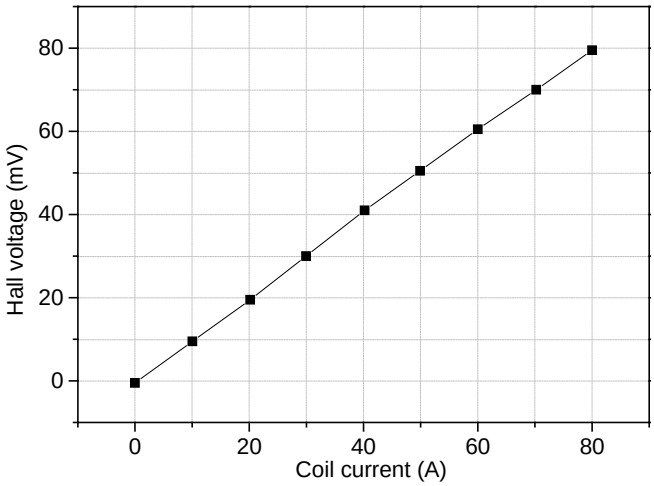

FIG. 3.10. Relationship between the Hall voltage and the transport current in the coil.

3.3.2 Experimental procedure

The charging procedure was as follows: turn on the current supply → apply AC magnetic field to open the PCS→ turn off the AC field →turn off the current supply. Unlike heat controlled PCS or high field controlled PCS, which drive the superconductor normal, the AC field controlled PCS is switched "off" by dynamic resistance, so that the value of switching "off" resistance can be controlled by changing the intensity or frequency of the applied AC field. In the following experiment, applied field magnitude varied from to 18mT to 0.695T (peak value), with the frequency changing from 1Hz to30Hz.

3.3.3 Influence of field frequency

The charging current of the power supply was set to be 85A, which was slightly larger than the critical current of the coil. The magnitude of applied field was 0.695T. Field frequencies used were 1Hz, 5Hz, 10Hz, 20Hz, and 30Hz.

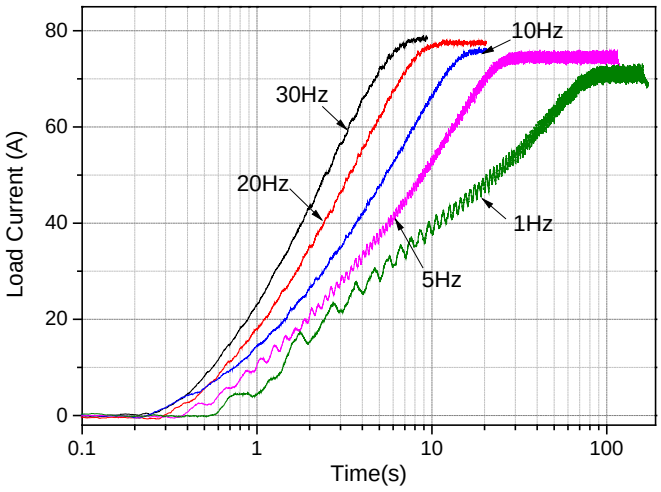

FIG. 3.11. Load current curves under different field frequencies. The field intensity was 0.695T.

Fig. 3.11 shows the load current curves in which each data point was the average of adjacent samples over 0.1s. Higher field frequency achieves a faster charging speed, as well as a higher load current. For field frequency over 5Hz, the final load current

reaches a value close to the critical current of the coil. The current curve of 1Hz field differs from other curves, besides the overall low charging speed. The load current increases faster in the beginning, this is mainly because high frequency noises existed in the applied field. Because the KEPCO is not designed for inductive loads, when it is driving an inductive field magnetic, there are high frequency noises with magnitude up to 10mT.

3.3.4 Influence of field magnitude

The charging current was set to be 85A. The field frequency was 30Hz. Field magnitudes of 0.695T, 0.49T, 0.245T, 0.12T, 50mT, and 24mT were chosen.

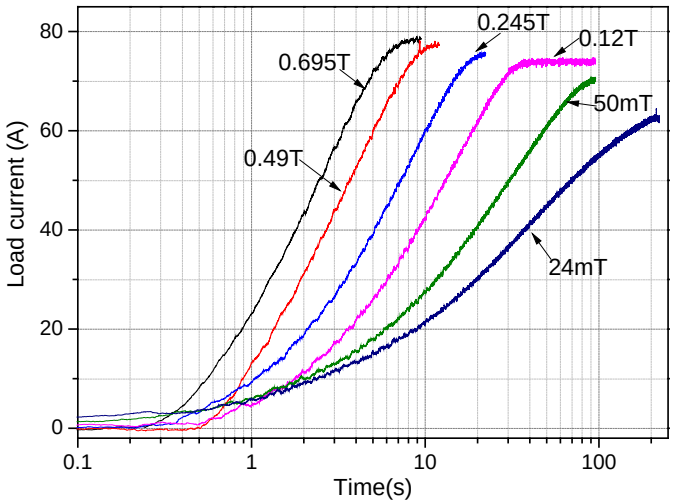

FIG. 3.12. Load current curves under different field magnitudes. The field frequency was 30Hz.

As can be seen from Fig. 3.12, before the load current saturates, all curves approximately follows the charging curve of an *RL* circuit. Time constant τ of charging is obtained by calculating the time of load current increasing from 0A to 53.7A (85(1-1/*e*)A). The result is shown in Table 3.2.

TABLE 3.2 TIME CONSTANT OF CHARGING

Field intensity (T)	τ (s)
0.024	93.4
0.05	37.5
0.12	15.6
0.245	8.18
0.49	3.62
0.695	2.55

The time constant is approximately inversely proportional to field intensity for all cases except 24mT. The final load current level of 24mT field case is also much lower than other cases, which indicates that 24mT field cannot fully switch “off” the PCS.

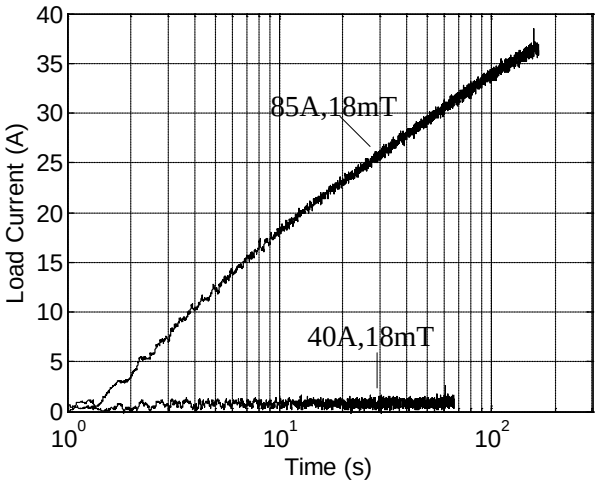

FIG. 3.13. Load current curves under low field intensity with different charging currents. Field frequency was 30Hz, with a magnitude of 18mT.

To test the performance of the PCS under lower field, the magnitude of the AC field was adjusted to 18mT (which was the minimum achievable field in the setup). As shown in Fig. 3.13, for 85A charging current, the load current can be charged to 37A in 200s. For 40A charging current, however, nearly no current was charged into the load. According to Oomen [94], to generate the dynamic resistance, the AC field magnitude must be larger than a threshold field [92], so that the field can reach the

transport current. Lower transport current in the PCS means a higher threshold field. Therefore, when the field intensity is too low, it cannot overcome the threshold field, so that a certain amount of DC current can flow in the centre of the PCS where it is free from transport loss.

3.3.5 Switching off resistance

The switching off resistance can be calculated by $R=L/\tau$, where L is the coil inductance. As previously discussed, for low frequency and low field intensity case, the resistance is variable, therefore only the result of field magnitude over 0.12T and frequency over 5Hz is presented.

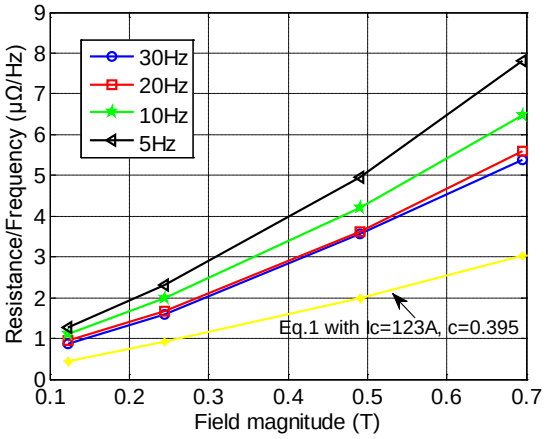

FIG. 3.14. Relationship between switching off resistance, field frequency, and field magnitude.

Fig. 3.14 shows the normalized switching off resistance against frequency (R/f) with different field magnitudes. It can be found that the normalized resistance value is higher with lower frequency, but the difference between 20 Hz and 30Hz is very small. This is mainly caused by the noises in the field, which makes the measurement less reliable. Assuming that the absolute value of noise generated dynamic resistance is independent on the signal frequency, relatively it contributes more to the total dynamic resistance at lower signal frequency. It can also be seen from Fig. 3.14 that although the normalized resistance increases with field increase, the curves are not

linear. The result indicates a field dependence of critical current density in the switch superconductor. By fitting the 20Hz and 30Hz curve using the form of Eq. 3.4, we can get the coefficient $c \approx 0.395$. However, if we take into consideration of I_C=123A, the calculated resistance value is much lower than the experimental result, as shown in Fig. 3.14. This is because of a large demagnetization factor of the tape, whereas Eq. 3.4 describes the result for an infinite slab.

The largest switching off resistance value is less than 0.2mΩ. Considering the copper stabilizer in parallel with the superconducting layer, it is quite difficult to achieve a resistance higher than 0.6mΩwithout increasing PSC tape length.

3.3.6 Current retaining test

After charging the coil to about 80A, the current retaining test was conducted. Fig. 3.15 shows the current decay curve, in which the Y-axis is in Natural Logarithm Coordinate (ln). A rapid current decay was observed in the beginning when the current was over 65A. This fast current decay can be mainly attributed to flux motion associated resistance of the coil superconductor nearly its critical current. For current lower than 65A, the current decayed with a slow but constant rate. This constant decay is mainly caused by the joint resistance. The joint resistance is therefore estimated from the slope of the curve to be 0.12$\mu\Omega$.

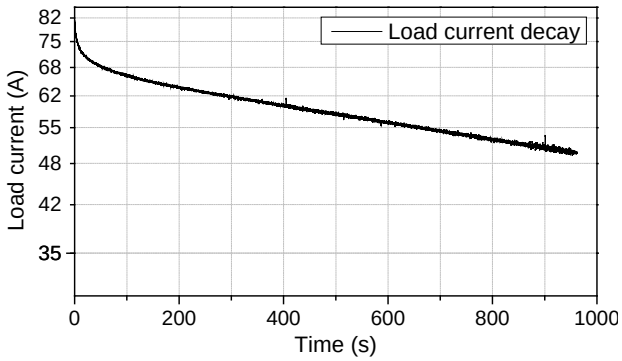

FIG. 3.15. Current free decay in the superconducting coil.

3.3.7 Summary

The result in this section preliminarily verified that the dynamic resistance induced by external AC field can be used as a persistent current switch in charging an HTS coil. The response speed and stability are also crucial characteristics for the switch, which will be investigated in the following section.

3.4 Response speed and stability of the AC field controlled switch

3.4.1 Experimental system

The experimental system is shown in Fig. 3.16, which is slightly different from that in the previous section.

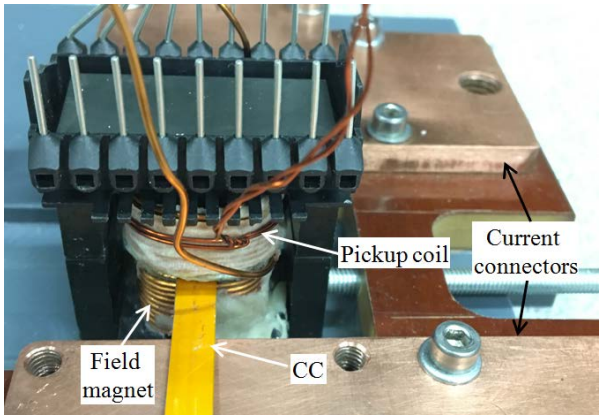

FIG. 3.16. Experimental system to investigate the dynamic response of AC field controlled PCS.

It is expected to study the voltage response speed to the applied field, so a higher frequency field is required. A new electromagnet was manufactured, which consisted of a pair of ferrite core, and a copper winding of 80 turns. The cross section of the air gap in the new arrangement was 2cm×1.2cm. The inductance of the magnet was 0.82mH from the previous 36mH. A more powerful EP4000 audio amplifier was used to power the electromagnet. A portion of CC of the same type as that in the previous

section was used as the switch superconductor. It had a 135A critical current (@77K, with E_0=1μV/cm criterion) in the gap. The CC was only connected to the current supply rather than to any superconducting load. The CC voltage was measured via a pair of voltage taps which were soldered to the CC surface with a 2cm separation. The AC field value was obtained using a pickup coil which had two turns closely wound outside the field winding. All signals were acquired by an NI-PCIe 6221 DAQ card, which had a sampling resolution of 69μV.

The signal which controlled the applied field was programmed in LabVIEW and outputted by the DAQ card. In order to study the response speed, the field was applied intermittently rather than continuously. As shown in Fig. 3.17, the signal consists of multiple sequences of sinusoidal wave. The number of cycles in each sequence was adjustable, and it can be as low as only one. The frequency and magnitude of the sinusoidal wave, as well as the time interval between two sequences were also adjustable. Fig. 3.17 shows a case in which there are three sequences of sine wave, each sequence consists of two continuous cycles of a 2kHz sine wave, and the time interval between sequences is about 100ms.

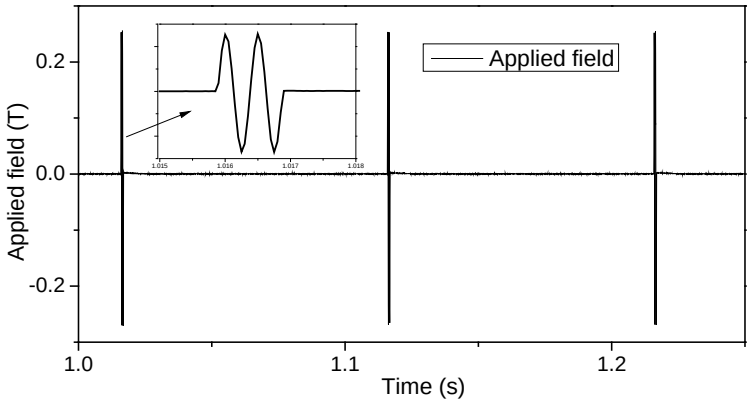

FIG. 3.17. Waveform of the applied field. The waveform consists of three sequences, each sequence includes two cycles of sine wave.

3.4.2 Dynamic response

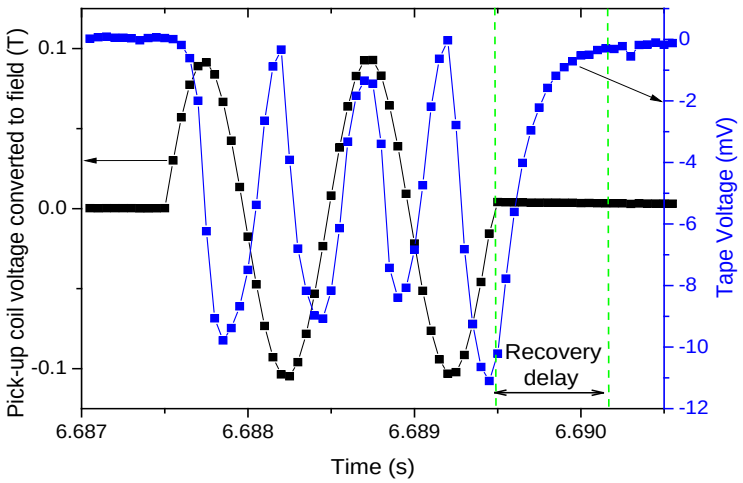

FIG. 3.18. Dynamic response of tape voltage to the applied field. Two cycles of 1kHz sine wave field was applied.

Fig. 3.18 shows the result for an 80A transport current under 1kHz, and 0.1T applied field. In each sequence, two continuous cycles of sine wave were applied, as can be seen in the black curve. As soon as the field was applied, a voltage appeared across the tape, as shown in the blue curve. The tape voltage was always negative although there was fluctuation, indicating that the flux going across the tape was unidirectional. Four peaks appeared in the voltage waveform. This is in accordance with the typical dynamic resistance's characteristic which shows two peaks per field cycle [93]. The peaks, however, did not always appear at the field fastest changing point. This may be because of the field dependence of critical current density. After the applied field was removed, the tape voltage did not disappear instantaneously. There was a recovery delay of about 0.7ms. This delay limits the operating frequency of the switch at about 1.5kHz which is high enough for most practical applications.

3.4.3 Voltage stability versus applied field duration

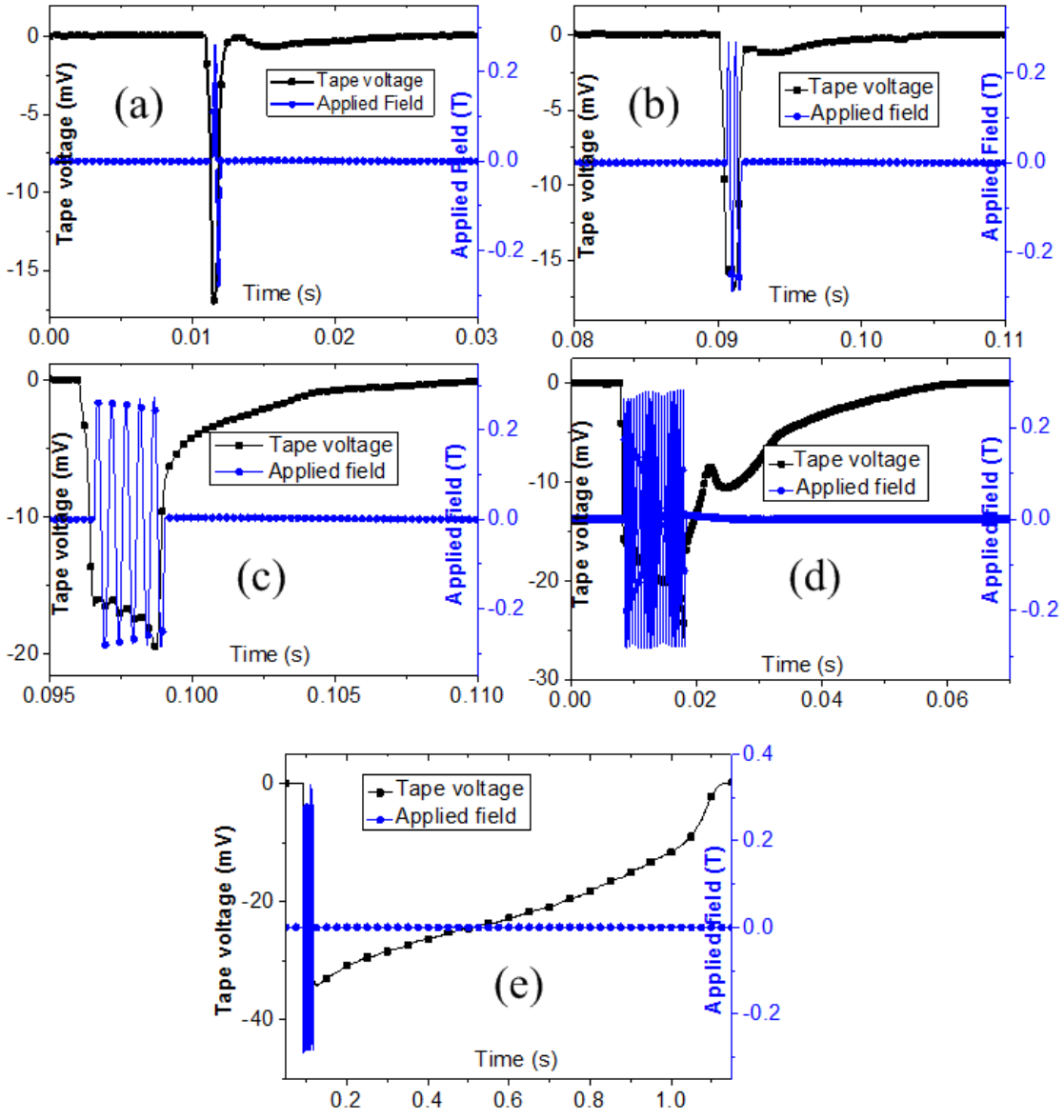

FIG. 3.19. Tape voltage recovery delay under different cycles of applied field. The field frequency is 2kHz. (a) 1 cycle, (b) 2 continuous cycles,(c) 5 continuous cycles, (d) 20 continuous cycles,(e) 50 continuous cycles.

Fig. 3.19 shows the voltage recovery delay versus different cycle numbers of applied field. The cycle numbers of 1, 2, 5, 20, 50 were chosen. The voltage has been filtered by averaging samples over each cycle. The applied field frequency was 2kHz and the

magnitude was about 280mT. Obviously the recovery time is positively related to the number of field cycles. For one cycle or two cycles of applied field, the tape voltage disappeared shortly after the field was removed. In contrast, for 5 cycles of applied field the recovery delay was about 10ms, and for 50 cycles of applied field, the superconductor quenched. In Fig. 3.19(c), it is clear that with each cycle of field being applied the voltage increased a little bit, indicating that the superconductor was becoming more and more unstable. This was mainly caused by the thermal instability. Heat is generated from various sources. Firstly, flux motion (including dynamic resistance and flux flow resistance) in the DC carrying superconductor generated heat. Moreover, AC magnetization loss also contributed to heat generation. Lastly, the substrate may also have non-negligible eddy current loss under high frequency field. The heat dissipation was mainly through heat conduction between the CC and Liquid Nitrogen (LN) in the gap. If the temperature rises severely the LN would vaporize. Because the gap was so narrow, nitrogen bubbles might attach to the tape surface, thus further deteriorating heat transfer. The positive feedback eventually resulted in a quench of the superconductor. The author conducted the same experiment under lower field magnitudes and lower frequencies. It was found that for a tape voltage of less than 10mV (5mV/cm electric field) no obvious recovery delay was observed. This electric field magnitude could be indicative for future applications.

3.5 Conclusion

In this chapter, the idea of using an AC magnetic field controlled high temperature superconducting persistent current switch was proposed and verified. Different from DC field controlled PCS, the AC field controlled PCS employs dynamic resistance as the source of switching off resistance. Compared with heat controlled PCS, the AC field controlled switch is much faster. The advantage of AC field controlled PCS over DC field controlled switch is that field intensity required is much lower. Although the

switching off resistance is too small for power use, it may be promising in HTS flux pump usage, which is to be studied in the next chapter.

Chapter 4
An HTS Flux Pump Based on AC Field Triggered Flux Flow

4.1 Introduction

In this chapter, firstly, a novel flux pumping mechanism for HTS coils is proposed, together with an analytical model. An experimental system which includes a prototype flux pump is built and tested, and the proposed mechanism and the analytical model are verified. The flux pumping characteristics under various operating conditions are then investigated.

4.2 Basic mechanism of an HTS flux pump [97]

4.2.1 Using AC magnetic field to trigger a unidirectional flux flow

In Chapter 3, it was demonstrated that an HTS coil can be charged up to nearly its critical current using a high DC power supply and an AC magnetic field. The underlying physics is that when an AC magnetic field is applied perpendicular to a DC transporting HTS tape, flux flow is triggered in the tape. During each AC field cycle, the flux flow direction is only dependent on the direction of transport current, rather than the polarity of the AC field. For a DC transport current, the flux flow is always in one direction. Therefore, flux can be accumulated in the load coil, thus pumping up its current. Although it is not a flux pump because of the existence of a DC power supply, it could be indicative for achieving flux pumping. One possible way is to induce a high AC transport current in the superconducting switch tape using an external magnetic field, rather than using the DC power supply. To achieve a

unidirectional flux flow, the AC field should be intermittently applied to the switch superconductor when the alternating current in the switch reaches one polarity.

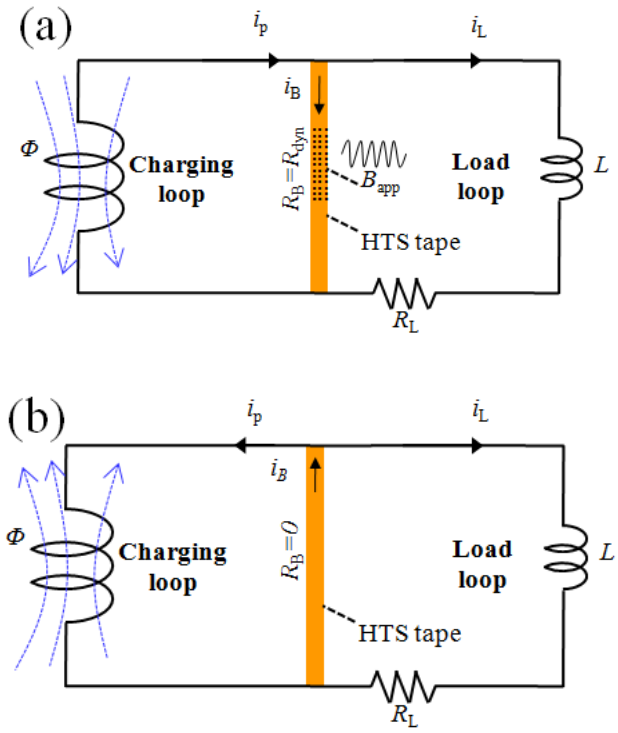

FIG. 4.1. Circuit of the proposed flux pumping mechanism, (a) AC field is applied to the HTS tape, so that flux flows into the load loop through the resistive bridge. (b) Current retaining process, AC field is removed, so that the load loop is shorted by the HTS tape. Φ denotes the instantaneous value of flux applied to the charging loop.

The arrangement is shown in Fig. 4.1. Two current loops, a charging loop and a closed superconducting load loop are joined together by an HTS bridge (a piece of HTS tape). Low frequency alternating current i_p in the charging loop is induced by an external magnetic field. During each i_p cycle, there are two phases: the energizing phase and the current retaining phase. In the energizing phase, as shown in Fig. 4.1(a), when instantaneous bridge current i_B flows from top to bottom, an AC field B_{app} with a much higher frequency (referred as 'bridge field') is applied perpendicular to the bridge tape surface. Flux flows into the load loop through the bridge tape. An

alternative way to understand this is that a voltage is developed across the bridge tape when the bridge tape is resistive (i.e. the dynamic resistance), and this voltage appearing across the load coil charges the load. In the current retaining phase, as shown in Fig. 4.1(b), there is no bridge field, and the bridge tape has nearly zero resistance, thus shorting the load coil. By repeating the above process, flux may gradually be accumulated in the load loop, and the load current i_L is increasing.

4.2.2 A basic analytical model

During the energizing phase, because the frequency of B_{app} is much higher than the frequency of i_p, i_p can be considered as quasi-DC. The amount of flux injected into the load is

$$\Delta\phi_{on} = (I_p - i_L) R_{dyn} pT - i_L R_L pT \qquad (4.1)$$

Where R_{dyn} is dynamic resistance which is the same as described in Chapter 3, T is the period of i_p, p is the proportion of T during which B_{app} is applied. I_p is the average value of i_p for the time during which B_{app} is applied. i_L is the load current, and R_L is the load loop resistance. R_L is an equivalent value for the resistance of the load coil which considers joint resistance, flux creep and other losses in the load loop.

During the current retaining phase, the amount of flux that flows out of the load loop is

$$\Delta\phi_{off} = -i_L R_L (1-p) T \qquad (4.2)$$

Therefore, during time period T, the net flux increase in the superconducting load can be expressed as

$$\Delta\phi = \Delta\phi_{on} + \Delta\phi_{off} = I_p R_{dyn} pT - i_L T (R_{dyn} p + R_L) \qquad (4.3)$$

Considering T as being short in comparison to the time taken to charge the load, the variation of i_L in a single cycle neglected. Thus Eq. 4.3 can be described in differential equation form as

$$\frac{\Delta\phi}{T}=L\frac{i_L}{dt}=I_p R_{dyn} p - i_L (R_{dyn} p + R_L) \qquad (4.4)$$

Where L is load inductance.

Assuming that I_p is constant during the whole charging period, the solution for Eq. 4.4 is

$$\begin{cases} i_L = A(1-e^{-t/\tau}) \\ A = I_p / (1 + R_L / R_{dyn} p) \\ \tau = L / (R_L + R_{dyn} p) \end{cases} \qquad (4.5)$$

According to Eq. 4.5, the final load current can be obtained is proportional to I_p, which means if B_{app} is always applied at i_p reaching one peak, a high value of i_L can be achieved.

In the above analysis, the author only considers the process of flux flowing into the load loop from the charging loop. Since flux must flow into the charging loop the charging loop must have some resistance its own independent of any resistance in the bridge. These resistances can be joint resistance, AC loss resistance, or simply another dynamic resistance. Quantitative analysis of the function of these resistances is discussed in Chapter 6.

4.3 Experimental system

An experimental system was built to verify the proposed mechanism and the analytical model. Fig. 4.2 shows the schematic system. The system has four elements: the circuit, the power supplies, a control signal generation system, and a signal

measurement system. Each of the elements is introduced in detail in the following discussion.

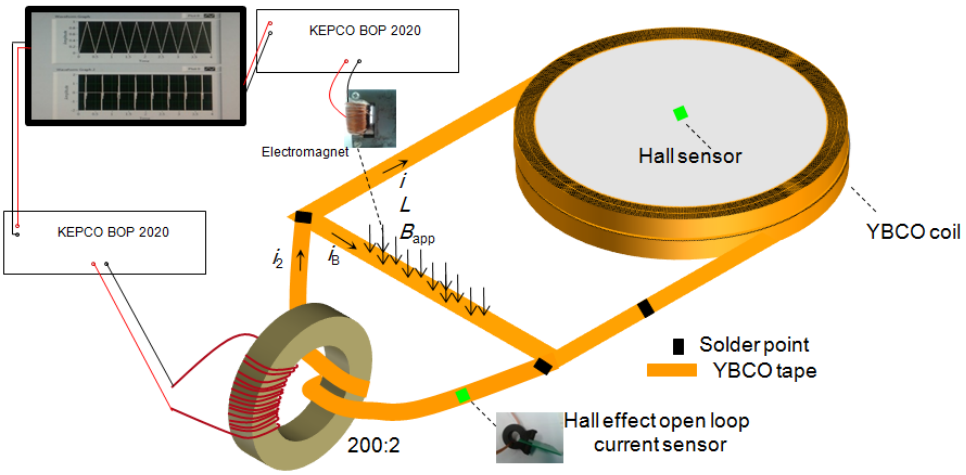

FIG. 4.2. Schematic drawing of experimental system of the flux pump.

4.3.1 Circuit

A picture of the circuit is shown in Fig. 4.3, with its schematic drawing shown in Fig. 4.4.

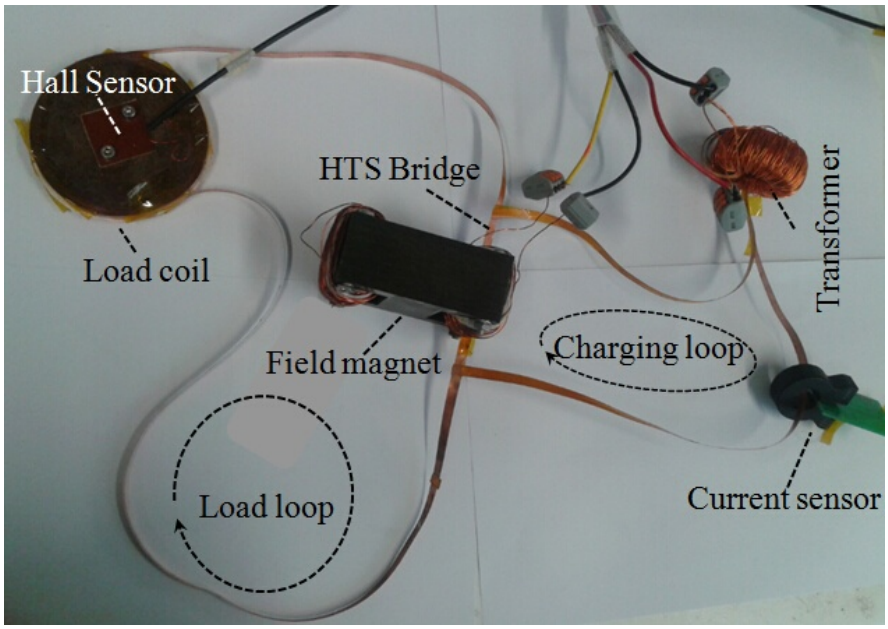

FIG. 4.3. Picture of the flux pump circuit.

The charging current i_p in Section 4.2 can be induced by an external field in various ways, but in the experimental system, an iron core transformer was used. **The subscript "*p*" in charging current i_p is replaced by the subscript "2" in transformer secondary current i_2 from now on**. The primary side of the transformer consisted of 200 turns, which was wound by copper wire of 0.8mm diameter. The secondary side of the transformer consisted of 2 turns. It was formed by a 1 meter long section of 6mm YBCO tape. The shape of the iron core was a hollowed cylinder, which had an inner diameter of 1cm, outer diameter of 3cm, and length of 1cm. The secondary winding of the transformer was shorted by soldering its two ends to a 10cm portion of YBCO tape of the same type (referred as "the bridge"), thus forming the charging loop. The bridge also shorted a double pancake CC coil, thus forming the load loop. The coil is the same one which was described in Chapter 3. Its inductance and critical current were measured to be 0.388mH and 81A @77K respectively. The joint resistance in the load loop was measured to be $1.2\times10^{-7}\Omega$. The bridge field B_{app} was generated by an electromagnet, which was the same as described in Section 3.3. The magnet's inductance was measured to be 36mH.The bridge tape was put into the centre of the 1mm air gap of the electromagnet, so that B_{app} was applied perpendicular to the wide surface of tape. The effective area of the bridge tape subjected to the field was 35mm×6mm.The bridge tape was measured to have a critical current of 123A in the air gap @77K (with $E_0=10^{-4}$V/m criterion). All the superconducting parts in the circuit worked in Liquid Nitrogen @77K.

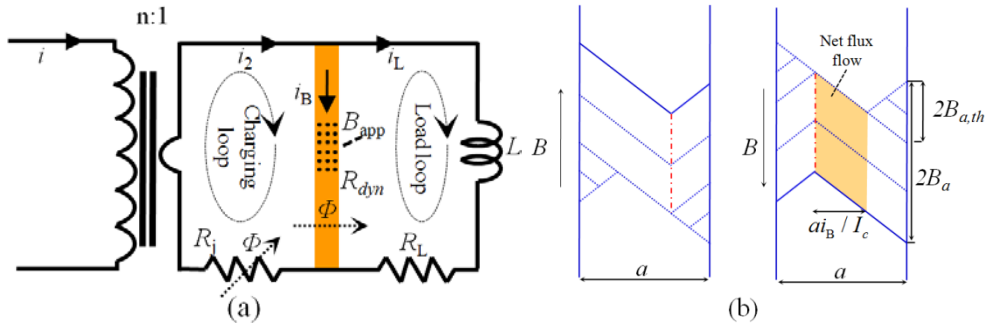

FIG. 4.4. Schematic drawing of the flux pump circuit and trace of flux flow. (a) Schematic drawing of the flux pump circuit, in which flux motion direction is indicated. R_j represents the joint resistance in the charging loop. (b) flux flow mechanism in DC carrying type II superconductor under one cycle of perpendicular AC field, in which a is the width of the superconductor, I_c is the critical current of the superconductor, $B_{a,th}$ is the threshold field, and the superconductor is assumed to have infinite thickness. The figure can approximately represent the flux flow process in the bridge superconductor, although it is thin.

4.3.2 Power supplies

Two KEPCO BOP 2020 power supplies were used in the experiment. One was used to power the transformer and the other was used to power the field magnet. The KEPCOs worked as power amplifiers, which were able to amplify external input signal and give an output up to 20A and 20V. In the experiment, both of the KEPCOs operated in current mode, which means that the output currents were the amplification of external input signals. Because the load of the KEPCOs were mainly inductive, to protect the KEPCOs from being over voltage when operating in high frequency, two 20V anti-series connected Zener diodes were connected in parallel with the output terminals of each KEPCO, as shown in Fig. 4.5.

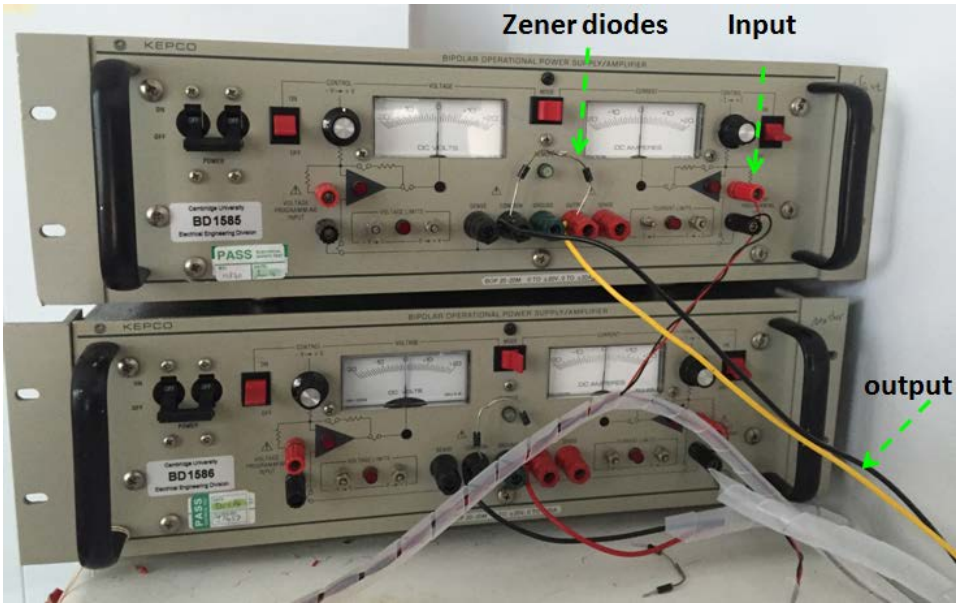

FIG. 4.5. Picture of KEPCO power supplies with input and output signals.

In order to damp down the noises in the inductive circuits (because the KEPCOs are not designed for driving inductive load), as well as to monitor output currents, a 0.1Ω resistor was connected in series with the primary winding of the transformer, and a 0.47Ω resistor was connected in series with the field magnet.

4.3.3 Generation of control signal

To control both of the power supplies, two signals were required. As described in Section 4.2, in order to achieve flux pumping, the bridge field must always be applied when the secondary current reaches the same polarity. Therefore, the two control signals should be synchronized. A program was built in LabVIEW software to generate digital control signals, as shown in Fig. 4.6.

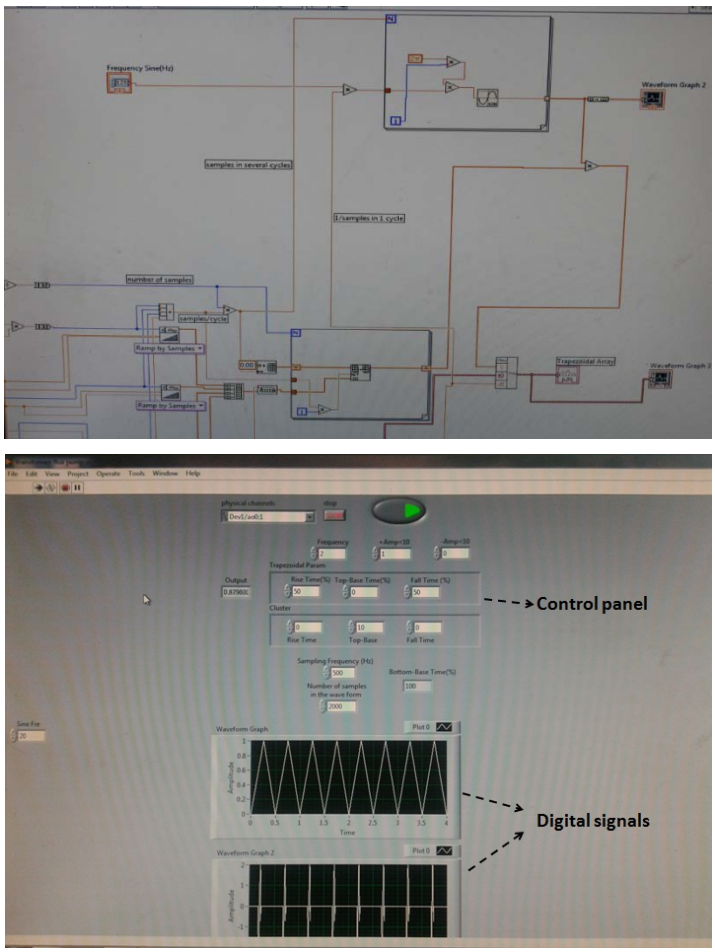

FIG. 4.6. Logical diagram and front panel of the digital control signal generating program in LabVIEW software.

The program allows users to set the frequency, magnitude, and waveform of each individual output signal, as well as the phase difference between the two output signals. The digital signals were then converted to analog signals using an NI-USB6002 DAQ card which was also controlled by LabVIEW software. Fig. 4.7 shows two synchronized signals generated by the DAQ card and captured by a scope. The intermittent, high frequency signal, in yellow was used to control the bridge field magnet, and the continuous triangular signal with relatively low frequency was used to control the transformer.

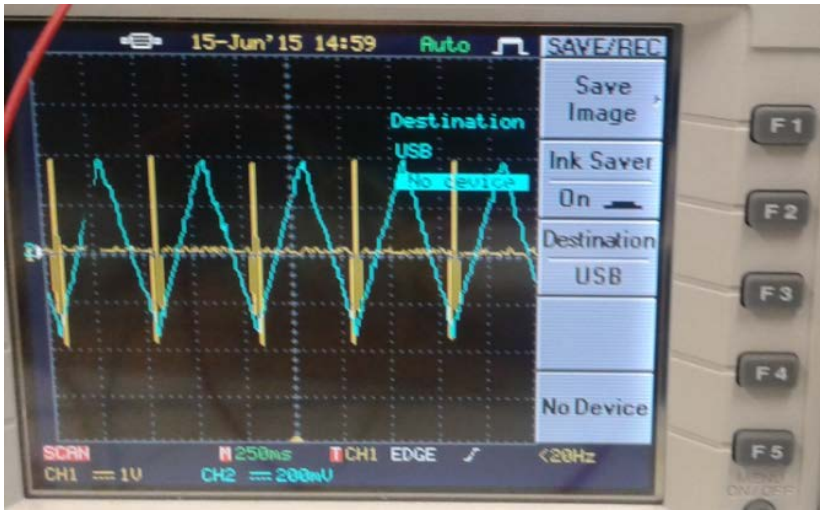

FIG. 4.7. Analogue signals generated by an NI DAQ card and captured by a scope. The signal in blue is to control the transformer current and the signal in yellow is to control the field magnet.

The analog output channels of the DAQ card were connected to the input of the two power supplies via voltage followers. This is to increase the output impedance as well as to isolate the DAQ card from the power supplies. In order to minimize external disturbance on the input signal, the signal lines were closely twisted together. A schematic of the control signal generation system is shown in Fig. 4.8.

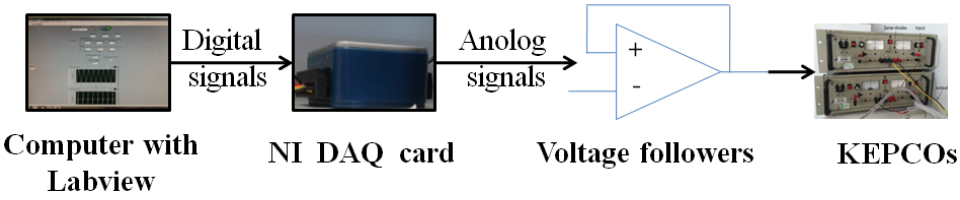

FIG. 4.8. Schematic drawing of signal generation system.

4.3.4 Signal measurement system

Three output signals were monitored and recorded, including secondary current i_2, the load current i_L, and the applied field B_{app}. The current i_2 was measured by a Hall effect open loop current sensor, as shown in Fig. 4.9.

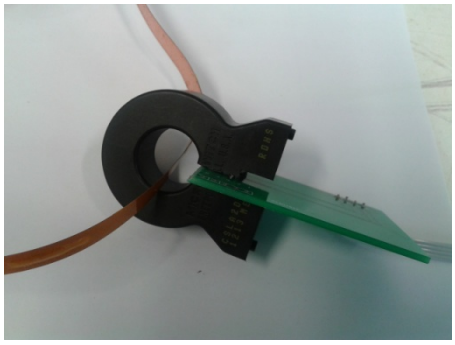

FIG. 4.9. Picture of the Hall effect open loop current sensor which is used to measure the secondary current in the experimental system.

The sensor consists of a ferrite core with a narrow gap (about 2mm), and a Hall sensor fixed in the centre of the gap. The secondary winding of the transformer is passed through the iron core. According to Ampere's Law, when current flows through the secondary winding, flux lines will circulate the current. The magnetic iron core concentrates the flux lines and generates a magnetic field proportional to current magnitude in the air gap. By measuring the magnetic field via the Hall sensor, the transport current can be obtained.

Before measuring i_2, the Hall effect open loop current sensor was calibrated using a DC power supply. As can be seen from Fig. 4.10, the measured Hall voltage is nearly proportional to the transport current, the ratio is determined to be 65mV/100A.

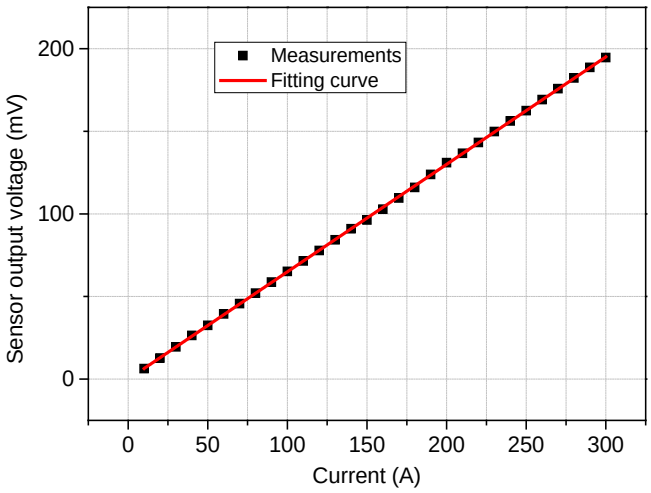

FIG. 4.10. Calibration of the Hall effect open loop current sensor.

The i_L was measured by a Hall sensor fixed in the centre of the coil, which is the same as described in Chapter 3. B_{app} was acquired by measuring the current supplied to the field magnet (actually by measuring the voltage of the 0.47Ω resistor connected in series with the magnet). All of the analog signals were digitised using an NI-USB6002 DAQ card. The card has 4 differential A/D conversion channels, with a resolution of 16 bits of each channel. The digitalised signals were recorded in a computer by NI Signal Express software.

4.4 Preliminary results

Fig. 4.11 shows the waveform of the secondary current i_2, the applied magnetic field B_{app} and the load current i_L in the first three cycles. The secondary current i_2 had a magnitude of about 90A and a frequency of 2Hz. B_{app} had a frequency of 20Hz with a magnitude of 0.65T. In each i_2 cycle, B_{app} was applied for 0.05s.

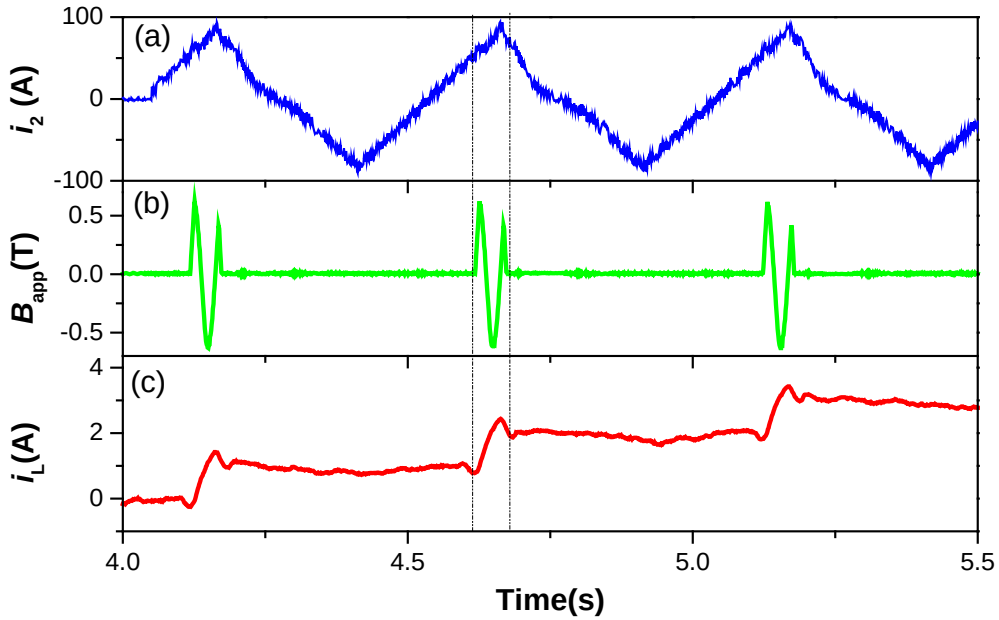

FIG. 4.11. Plots showing the waveforms of secondary current i_2, applied field B_{app}, and load current i_L during the first three cycles of charging.

From Fig. 4.11, it is very clear that each time B_{app} was applied to the bridge superconductor, the current in the load loop increased by a certain amount, indicating flux was injected into the superconducting load loop. The results in Fig. 4.11 fundamentally proved that flux pumping can be achieved by AC field triggered flux flow in a current carrying HTS tape, without breaking superconductivity. This is a novel and very important conclusion. Although the current i_B in the bridge superconductor had a 2Hz AC component, it was always the same polarity when B_{app} was being applied, as a result the flux flow across the bridge was unidirectional.

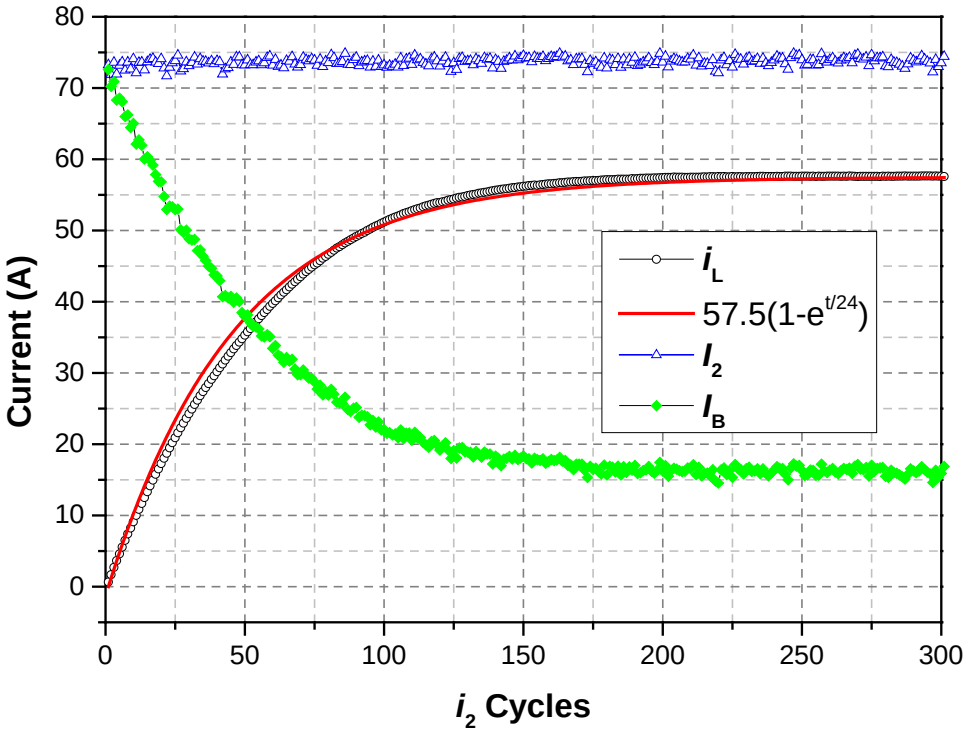

FIG. 4.12. Plots showing the waveform of currents during the whole charging process. The average transport current experiencing external field during each $i_2$cycle is $I_B=I_2-i_L$.

Fig. 4.12 shows the current curves during the whole charging process. During the charging process, $I_2$was maintained at a value of 74A. The load current i_L can be fitted by

$$i_L=57.5(1-e^{-t/24}) \qquad (4.6)$$

This has the same form as the prediction in Eq. 4.5. From the fit and according to Eq. 4.5, the dynamic resistance R_{dyn} is calculated to be 0.131mΩ, and R_L is 3.73$\mu\Omega$.

The value of R_{dyn} was measured under a DC transport current with 20Hz, 0.65T applied field, and the value was 0.106mΩ. The value of R_{dyn} in the flux pump is slightly larger than in the DC transport current condition. This is because the poor controllability of the DAQ card results in transience in B_{app}, which means that its real frequency is a value between 20Hz and 30Hz, as is shown in Fig. 4.11(b). According to Oomen [94] with Bean's model, the value of R_{dyn} is calculated to be 0.044mΩ, which is

less than half of 0.106mΩ. The higher result was obtained because of the field dependence of critical current density of the bridge superconductor, as well as the demagnetization factor of the thin bridge tape.

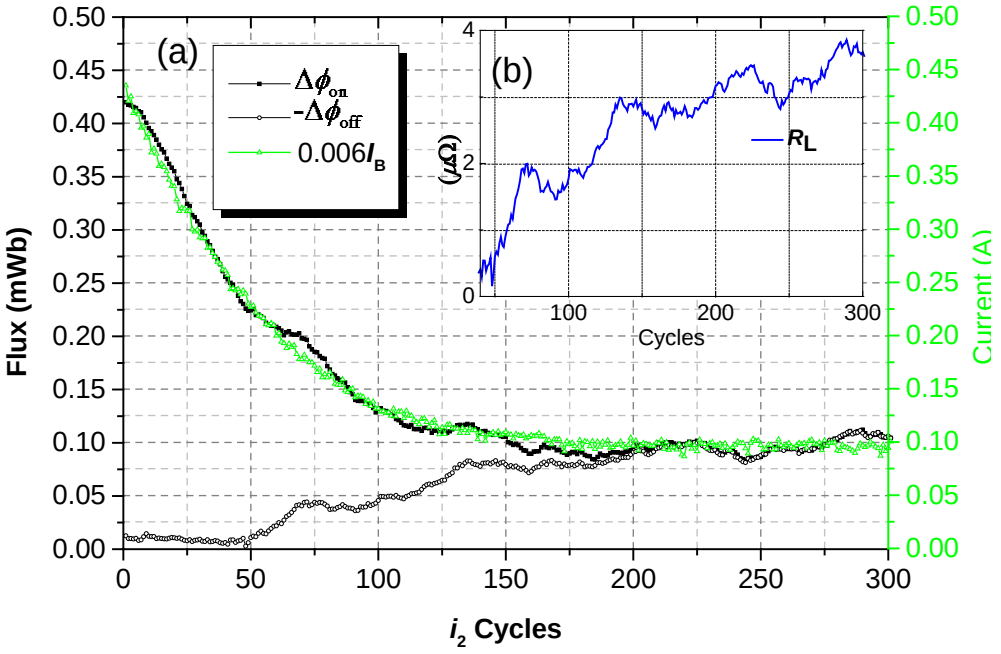

FIG. 4.13. (a)flux injected into the load and consumed in the load in each i_2 cycle in comparison with average bridge current. (b) instantaneous value of load loop resistance.

The value of R_L, however, is much larger than the joint resistance of $1.2\times10^{-7}\Omega$. To understand this phenomenon, $\Delta\phi_{on}$ and $\Delta\phi_{off}$ are extracted from load current waveform according to Eq. 4.1 and Eq. 4.2. As shown in Fig. 4.13(a), in each i_2 cycle, $\Delta\phi_{on}$ is nearly proportional to I_B, which indicates that R_{dyn} is constant during the charging process. As R_{dyn} is much larger than R_L, its value can be approximately calculated by $\Delta\phi_{on}/I_B pT$=0.129mΩ, which is close to the value of 0.131mΩ calculated by Eq. 4.5. $-\Delta\phi_{off}$ has a very small value in the beginning, but increases rapidly after 50 i_2 cycles. R_L in each i_2 cycle is calculated by Eq. 4.2 using $-\Delta\phi_{off}$ and i_L. As shown in Fig. 4.13(b), after 50th i_2 cycle, R_L increased sharply from 0.4μΩ to a stable value of about 4μΩ. This is because after 50 i_2 cycles, i_L exceeded 35A. When i_2 approached its negative peak, $i_B=i_2+i_L$ exceeded the critical current of the bridge superconductor. So that some current

in the bridge flowed through the copper layer in parallel with the bridge superconductor, thus causing a loss in the load loop. Therefore, in order to increase the final load current, a wider bridge tape with larger critical current value should be used. An alternative way is to induce an asymmetric current. For example, the positive current magnitude is 90A and the negative current magnitude is 60A. In this way, R_L can be reduced. The integration of the current over each cycle, however, should be zero to prevent the saturation of transformer. The influence of secondary current magnitude on charging will be discussed in detail in Section 4.5.1, in which asymmetrical secondary current result will also be presented.

4.5 Open loop operation characteristics of the proposed flux pump [98]

In Section 4.2, it has been shown that the pumping speed and final achievable load current are influenced by dynamic resistance of the bridge (R_{dyn}), the average secondary current experienced by applied field (I_2) and applied field duration over transport current period (p). These parameters are directly related to the transport current and applied field. In this section, the performance of the proposed flux pump is studied based on the following influential factors: secondary current magnitude and frequency, applied field intensity, applied field frequency, relative phase between applied field and secondary current, field applied duration, and secondary current waveform. The current waveform is triangular, as shown in Fig. 4.11(a), unless otherwise specified. In the experiment, all above mentioned parameters are controlled using a program written in LabVIEW.

4.5.1 Influence of secondary current magnitude on pumping performance

In the experiment of this section, the magnitude of secondary current was changed from 69A to 109A, with an increment of about 10A. Other parameters were fixed as: applied field magnitude 0.49T, applied field frequency 40Hz. Fig. 4.14 shows the load current curves under different magnitudes of i_2. The influence of i_2 magnitude on flux pumping performance is quite complicated. In terms of pumping speed, the load current saturates faster with a higher i_2 magnitude. The final load current, however, does not always increase with the increase of i_2 magnitude. Maximum load current is achieved when the i_2 magnitude is 80A. The final load current level decreases with the further increase of i_2 magnitude.

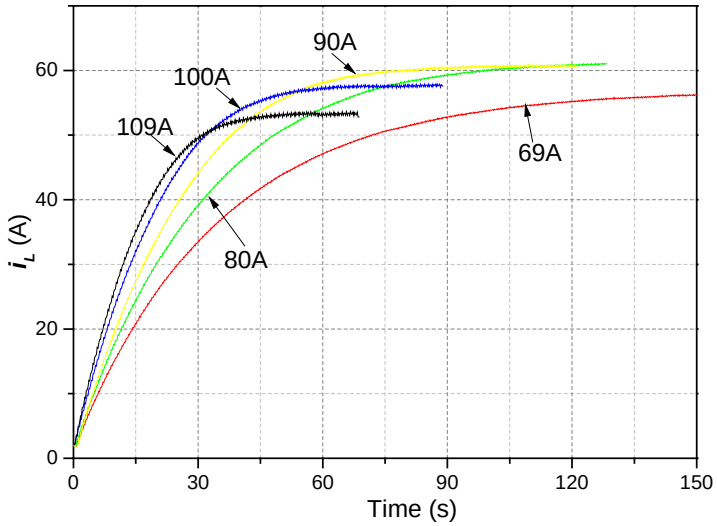

FIG. 4.14. Plots showing the load current curves during charging under different magnitudes of i_2. The magnitude changes from 69A to 109A with an increment of about 10A.

According to Eq. 4.5, the final load current should be proportional to the magnitude of i_2. However, Eq. 4.5 describes the ideal case without considering the current capacity of the bridge superconductor. Considering $i_B=i_2-i_L$, with the increase of i_L, i_B will reach a high value when i_2 is around its negative peak, which can be seen from Fig. 4.15(b).

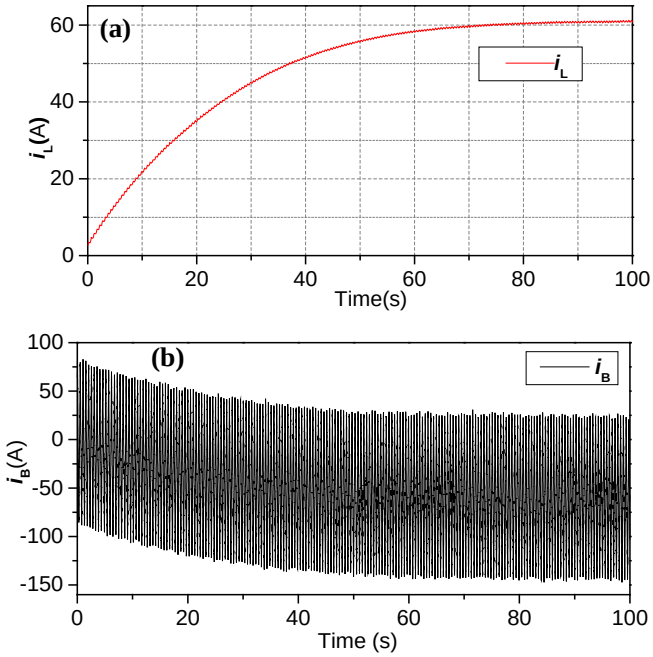

FIG. 4.15. Plots showing the variation of the bridge current with load current.

The critical current of the bridge superconductor is only 123A, if the bridge current exceeds this value, a certain amount of current has to flow through the parallel copper layer, thus generating a loss (in Eq. 4.5, the author treat this loss as one source of R_L).

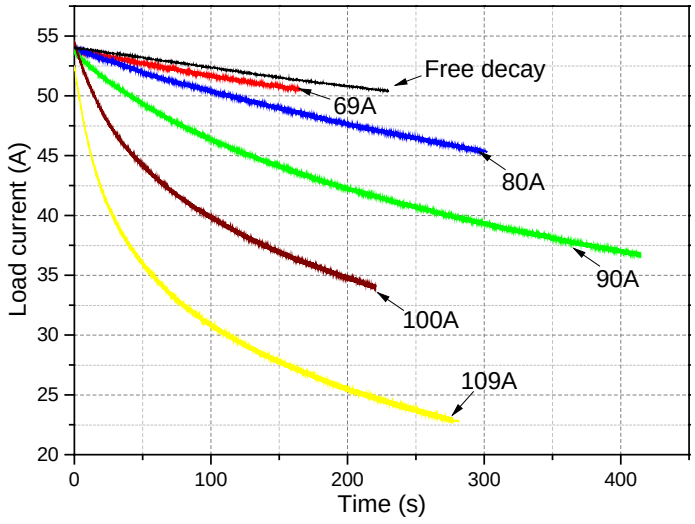

FIG. 4.16. Plots showing the load current decay curves under different magnitudes of i_2. The magnitude changes from 69A to 109A with an increment of about 10A.

To study this loss, a decay experiment was conducted under different secondary current magnitudes. In each case, the load current was firstly pumped up to saturated value, then the bridge field was switched off, but the secondary current remained. To make a comparative study, a free decay experiment was also conducted, in which case both of the applied field and the secondary current were switched off after charging the load. Fig. 4.16 shows the load current decay curves. The plot begins with all currents decaying to about 54A. As shown in Fig. 4.16, in the free decay case, the load current decays slower than all of those with secondary current, and the decay speed remains constant. The free decay is mainly caused by the joint resistance. For all cases with secondary current, larger secondary current magnitude causes a faster load current decay. For secondary current magnitude of 80A or above, the load current decay rate is not constant. These load currents decay faster in the beginning, and gradually slow down. In the 69A secondary current case, load current decays slightly slower than free decay case, with a nearly constant decay rate. The load current decay with secondary current is mainly caused by the limitation of the critical current of bridge superconductor.

In the charging up process, the load current saturates when the bridge field triggered flux flow is balanced by the flux consumption in the load loop which is contributed largely by the over current on the bridge, i. e.:

$$\Delta\phi_{on} = \int_{B_{app}\,on} (I_2 - i_L) R_{dyn} dt = \Delta\phi_{off} \approx \int_{B_{app}\,off} v_B dt \qquad (4.7)$$

Where v_B is the bridge voltage when field is off.For secondary current magnitude of 80A case, the final I_2-i_L≈9A, and R_{dyn}≈0.13mΩ with 40Hz, 0.49T field. Considering p=0.1, $\Delta\phi_{on}$ is calculated to be 0.058mWb. Fig. 4.17 shows the V-I curve of a tape which has the same type and length as the bridge tape. According to the V-I curve and waveform of i_2, the last term in Eq. 4.7 is estimated to be 0.02mWb-0.04mWb (it is unlikely to accurately calculated the value, because the sharp V-I curve will

significantly amplify any measurement error in the current.). The difference between these two terms can be attributed to extra losses contributed by joint resistance and hysteresis.

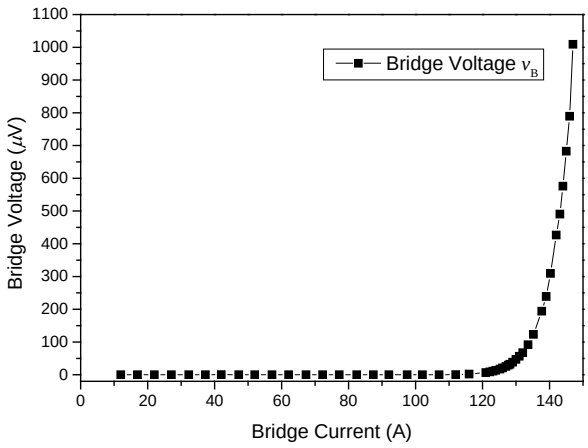

FIG. 4.17. V-I curve of an YBCO tape which has the same type and length as the bridge tape.

To overcome the current limit, one way could be to increase the width (current capacity) of the bridge. But in this way, the bridge field area and hence the inductance of the bridge magnet has to be increased to achieve the same dynamic resistance. An alternative solution is to generate an asymmetrical secondary current, with its positive peak value larger than its negative peak value. One waveform is shown in Fig. 4.18(a), and the pumping result is shown in Fig. 4.18(b). It is clear that an asymmetrical secondary current results in a better performance compared with symmetrical one.

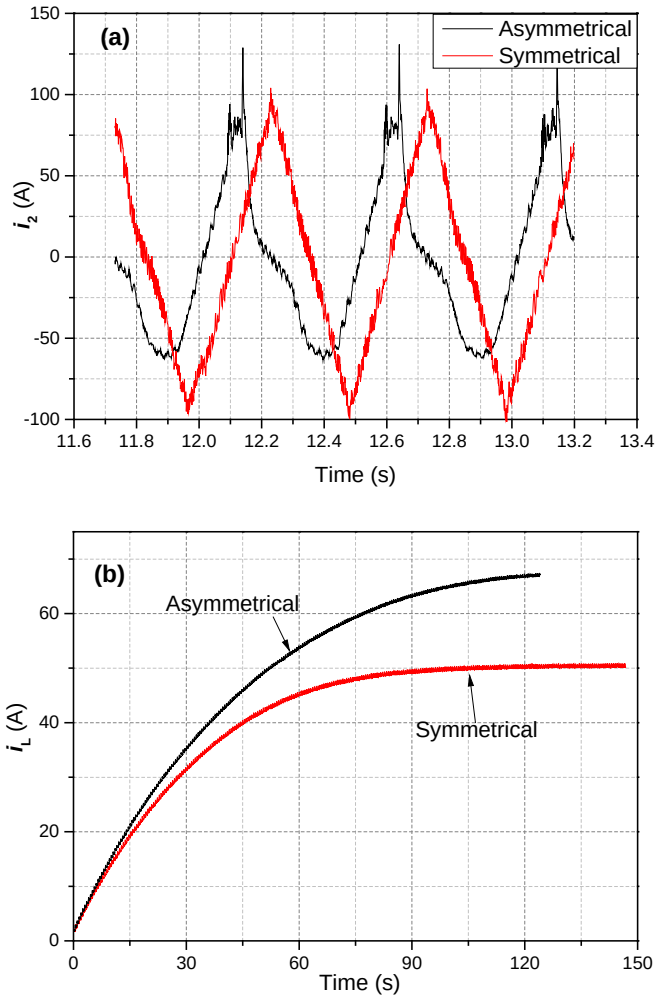

FIG. 4.18. Results on symmetrical and asymmetrical secondary current experiment, where bridge field magnitude is 0.49T, frequency 20Hz.(a) Waveforms of secondary current i_2. (b) Charging curve of load current i_L.

4.5.2 Influence of phase difference between secondary current and bridge field on pumping performance

The phase difference between the applied field and secondary current is defined as:

$$\Delta\theta = \frac{t_B - t_P}{T} \times 360^\circ \qquad (4.8)$$

Where t_B is the time centre of the applied field duration, t_P is positive peak time of i_2, and T is the period of i_2, as shown in Fig. 4.19. It should be noticed that a fixed time window pT was used to modulate B_{app}. If pT is not the integral multiples of B_{app} period, B_{app} has to be truncated. Therefore, $\Delta\theta$ relies on the centre of pT rather than the specific phase of B_{app}. If $\Delta\theta$=0°, it is defined as 'in phase'. The phase difference between secondary current and applied field directly determines I_2. When $\Delta\theta$=0°, maximum I_2 is achieved, whereas I_2=0 when $\Delta\theta$=90°. In the results of this section, all other parameters are fixed as: field frequency 30Hz, magnitude 0.49T, and secondary current magnitude 77A.

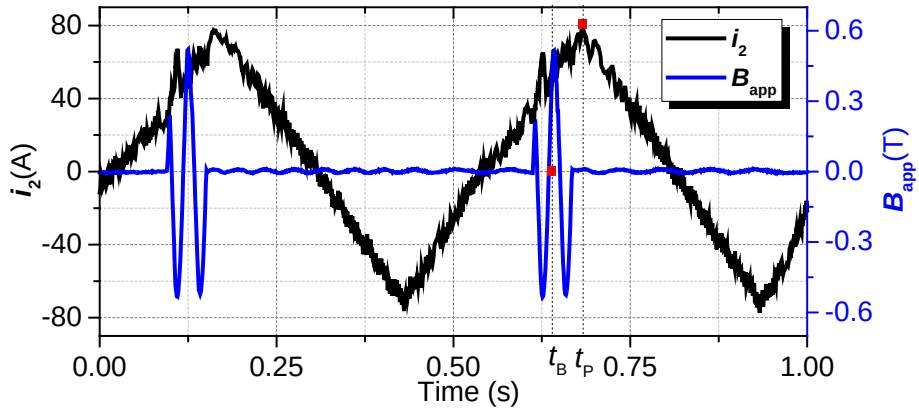

FIG. 4.19. Plots showing the waveforms of secondary current i_2 and applied field B_{app} together with the definition of t_B and t_P.

The load current curve of $\Delta\theta$=0°and$\Delta\theta$=180° is shown in Fig. 4.20. In the beginning, $\Delta\theta$ was set 0°, the load current gradually increased, and saturated at about 55A after 150s. Then the author changed $\Delta\theta$ to 180°, the load current decreased to zero, and then increased inversely. The final load current saturated at about -55A.

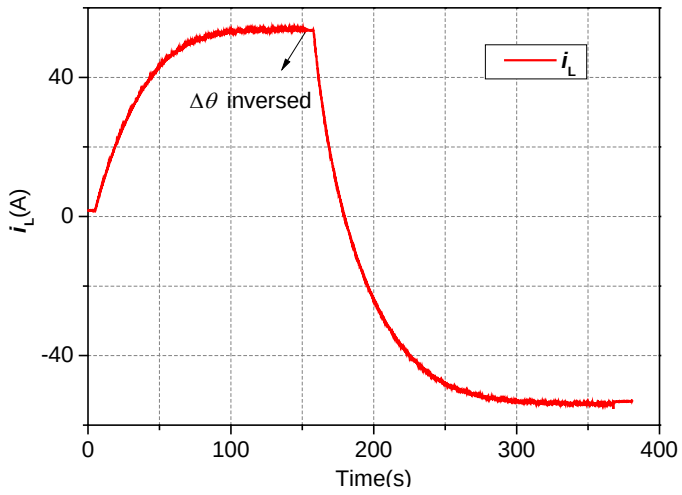

FIG. 4.20. Plots showing the waveform of load current with $\Delta\theta$=0° and $\Delta\theta$=180°, where $\Delta\theta$ is the phase difference between secondary current and applied field defined in Eq.4.8.

Load current curves under different $\Delta\theta$ are shown in Fig. 4.21(a). Each waveform was then divided by its saturated value, and the result is shown in Fig. 4.21(b). As can be seen from Fig. 4.21(a), although the load current curves are different from one another in terms of magnitude, their time constants are very similar. This is because R_{dyn} is nearly independent of transport current when the applied field magnitude is high. The load current curve of $\Delta\theta$=0 saturated slightly faster than other cases, because the bridge current capacity limits the load current, as discussed above.

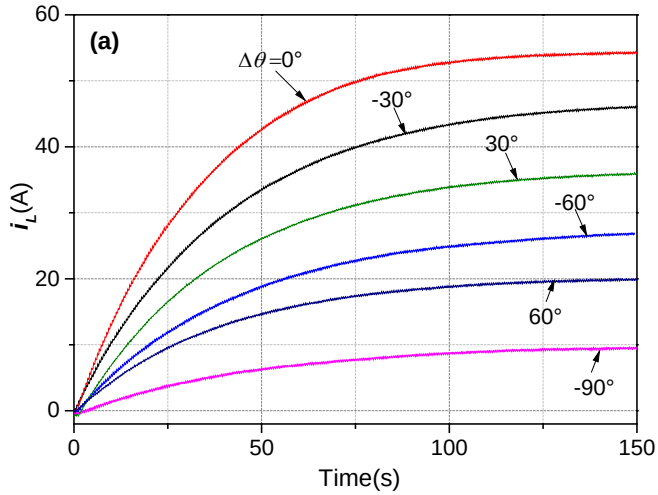

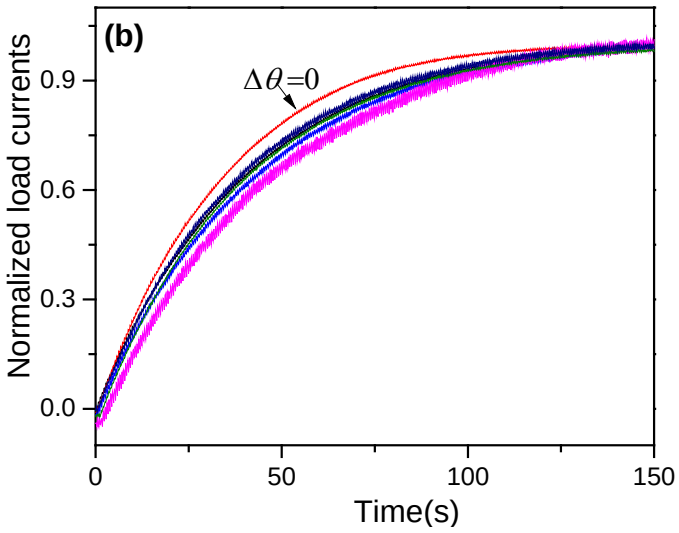

FIG. 4.21. Plots showing the load current curve under different values of $\Delta\theta$. (a) Load currents. (b) load currents divided by their final values.

Detailed experiments have also been done concerning the phase difference. The author incremented the phase difference $\Delta\theta$ in 10° steps up to 180°. The result of I_2 and final load current versus $\Delta\theta$ is shown in Fig. 4.22. The plot of I_2 versus $\Delta\theta$ is similar as the time domain waveform of i_2. The maximum final load current is achieved when the applied field and the secondary current are in phase. The curve is not perfectly symmetrical, mainly because of the distortion in the secondary current, which can be partly seen in Fig. 4.19.

The results shown in this section indicate that the final load current can be easily controlled by changing the phase difference between bridge field and secondary current. This is an obvious advantage over those travelling wave based flux pumps.

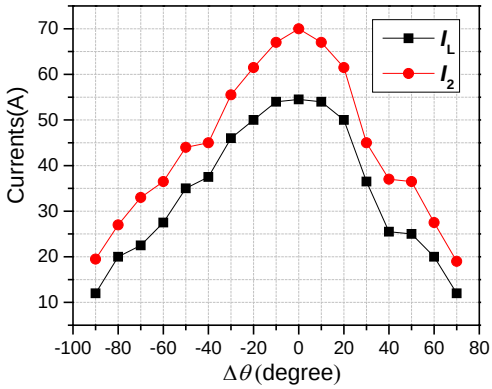

FIG. 4.22. Plots showing the final load current I_L and average secondary current over field duration I_2 with respect to $\Delta\theta$.

4.5.3 Influence of bridge field magnitude on pumping performance

The magnitude of applied field directly influences the amount of flux flowing across the bridge per cycle, as depicted in Fig. 4.4(b). It can also be considered as the influence on R_{dyn}, as described in Eq. 3.4. In this part of experiment, the author tried to decrease the field magnitude from 0.66T to nearly zero, with all the other parameters fixed as: magnitude of secondary current 90A, frequency of applied field 20Hz. The load current results under different field magnitudes are shown in Fig. 4.23.

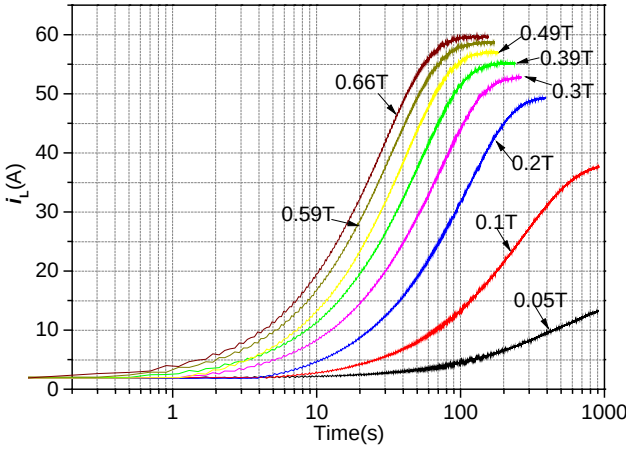

FIG. 4.23. Plots showing the waveform of load currents under different applied field magnitude. The field frequency is 20Hz.

As shown in Fig. 4.23, lager field magnitude generates a higher final load current level as well as a faster pumping speed. The minimum observable load current occurs when the field magnitude decreased to 50mT. In this case, it took about 15 minutes for the load current to saturate at about 13A. With field less than 50mT, no load current was observed, mainly because there was a noise of about 10mT in the field which would generate losses in the bridge all the time.

The load currents under B_a=0.65T and 50mT are shown in Fig. 4.24, together with a first order fitting.

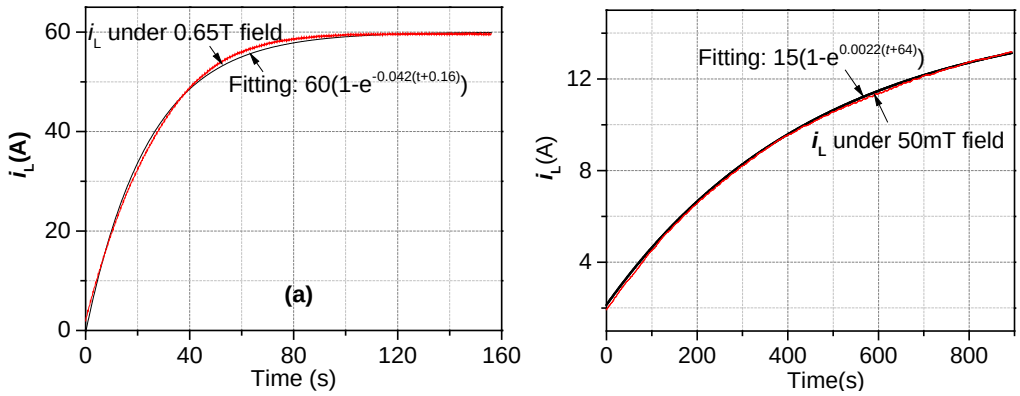

FIG. 4.24. Plots showing the load current curves and fitting curves. (a) under B_a=0.65T. (b) under B_a=50mT.

Each load current curve can be well fitted by a first order exponential fitting, which well proves the analytical model in Eq. 4.5. The fitting error in Fig. 4.24(a) is larger than that in Fig. 4.4(b). This is because for final load current less than 33A (the difference between critical current of the bridge and magnitude of secondary current, i.e. 123A-90A) the bridge current never exceeded the critical value of 123A, so R_L *is* nearly constant; whereas for final load more than 33A, the loss in the load loop (mainly on the bridge) increases with the increase of load current, resulting in a variable R_L. However, the error is tolerable by considering an averaged constant R_L.

The load current curve under 50mT field can be well fitted by:

$$i_L = 15\left(1 - e^{-0.0022(t+64)}\right) \qquad (4.9)$$

Considering the value of I_2 is about 74A, from Eq. 3.3, Eq. 4.5, and Eq. 4.9, we can calculate the value of the threshold field $B_{a,th}$ is around 25mT. The value is comparable with the measured value of 18mT under 60A DC current. All other load current curves can also be well fitted by a first order exponential fitting. The dynamic resistance values were calculated based on these fittings. The dynamic resistance are also calculated by Eq. 3.3, under Bean's model. Both results are shown in Fig. 4.25. The different between the measured value and predicted value under Bean's assumption is small when the field magnitude is less than 0.1T. And it increases with the increase of field magnitude. The difference on one hand comes from the demagnetization factor of the tape, as it is not infinite thick; on the other hand the difference indicates a very strong field dependence of critical current density in the bridge superconductor, as indicated in Eq. (3.4).

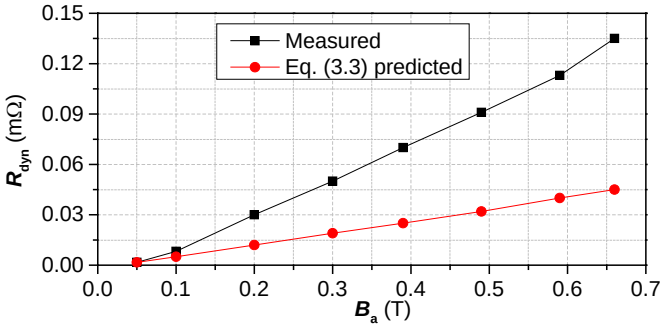

FIG. 4.25. Plots showing the calculated dynamic resistance under Bean's model and the measured value in the pump under different field magnitudes.

4.5.4 Influence of bridge field frequency on pumping performance

The magnitude of B_{app} influences the amount of flux flowing across the bridge per cycle, whereas the frequency of bridge field determines the number of cycles applied. Therefore, the total flux flow should be proportional to field frequency, which can also be seen from Eq. 3.3 in terms of dynamic resistance. In this part of experiment, all other

parameters were fixed except the applied field frequency. The secondary current magnitude was 90A, applied field magnitude was 0.49T. The frequency of applied field varied from 10Hz to 40Hz with a 10Hz increment. The load currents are shown in Fig. 4.26. The result shows that both of the pumping speed and final load current level can be enhanced by the increasing of bridge field frequency.

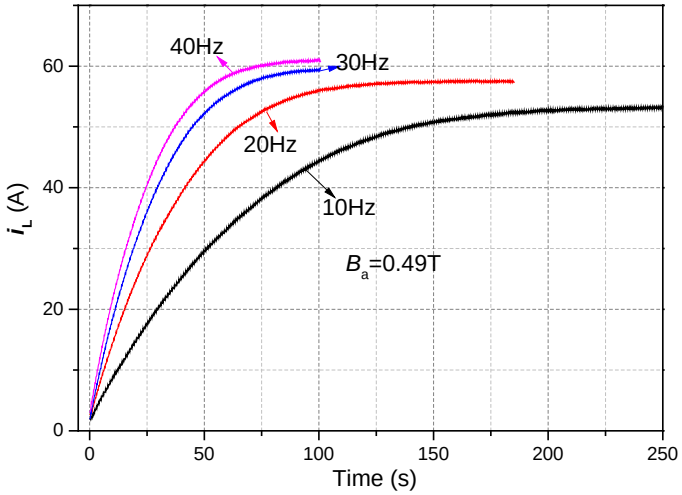

FIG. 4.26. Plots showing the load current curves under different applied field frequencies. The field magnitude is 0.49T.

The current curves are fitted by first order exponential equations. The values of dynamic resistance are calculated from the fitting and also from Eq. 3.3. The measured value of R_{dyn} seems not strictly proportional to field frequency. This is mainly because the control strategy. During each secondary current cycle, the field applied duration is fixed as 0.05s, which may truncate the field signal, so that transience is inevitable in the applied field. The transience will increase the actual field frequency. The effect is more significant when the field frequency is low, because fewer cycles of field are applied.

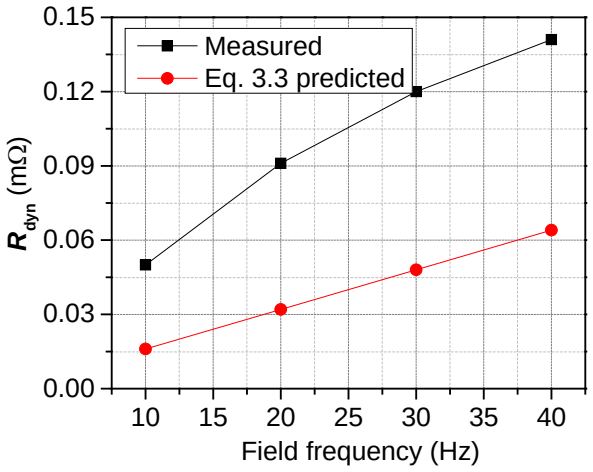

FIG. 4.27. Plots showing the calculated dynamic resistance under Bean's model and the measured value in the pump under different field frequencies.

4.5.5 Influence of secondary current frequency on pumping performance

According to Eq. 4.5, the performance of the pump is independent of frequency of i_2, as long as p is fixed. Eq. 4.5 describes the ideal case, where the transformer is ideal. In practical, if the transport current frequency is too low, say less than 0.5 Hz, the iron core of the transformer is likely to saturate. In this case, the charging current cannot remain controlled. In the following experiment, the author chooses to vary the frequency from 1.5Hz to 3Hz. Other parameters are: i_2 magnitude 90A, applied field magnitude 0.49T, applied field frequency 40Hz.

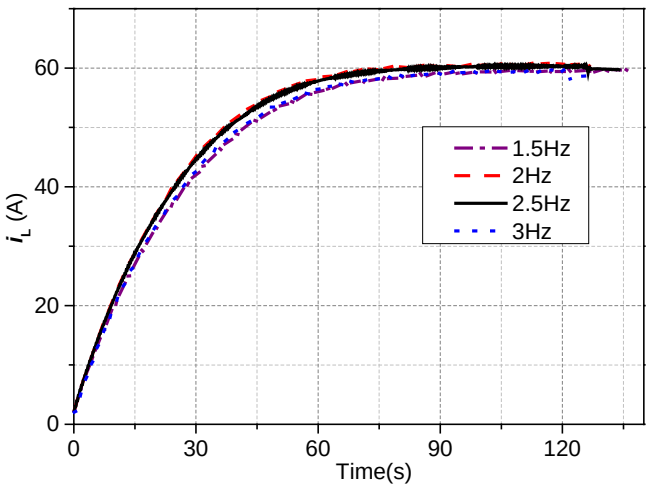

FIG. 4.28. Plots showing the load current curves under different charging current frequencies.

As shown in Fig. 4.28, there are very little differences between the four curves. The 1.5Hz and 3Hz curves are nearly overlapped, and the 2Hz and 2.5 Hz curves are nearly overlapped. A slight difference occurs between these two groups. This may be caused by some synchronising error between i_2 and modulated B_{app} in 1.5 and 3Hz cases. Thus the pumping speed is slower and the final load current is smaller compared with 2Hz and 2.5 Hz cases. The experimental result verifies the prediction in Eq.4.5 that transport current frequency has little influence on the pumping performance. In practical use, the transport current frequency should be as low as possible to reduce AC transport loss in the charging loop.

4.5.6 Influence of bridge field duration on pumping performance

The value of applied field duration p determines how long the field is applied in one charging current cycle. That is to say p determines the number of cycles of applied field if the field frequency is fixed. According to Eq. 4.5, a larger p means a faster pumping and a higher level of final load current. Rectangular secondary current waveform was used in this section, so that I_2 was independent of p. In theory, p can reach as high as 0.5. But in real experiment, the transformer was not powerful enough, so when p was larger than 0.3, the secondary current was severely influenced by the

applied field. The duration *p*, therefore, was chosen to vary from 0.1 to 0.25 to make sure that the secondary current did not change too much. We can see from Fig. 4.29 that the final load current is positively correlated with *p*. When the load current is less than 30A, the pumping speed is nearly proportional to *p*, which well proves the model in Eq. 4.5.

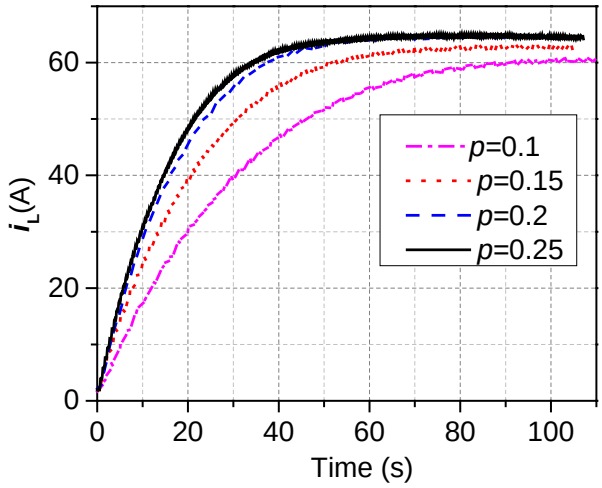

FIG. 4.29. Plots showing the load current curves under different time proportion of applied field.

In real applications, a larger *p* is preferable, because it can improve pumping performance without extra requirements on capacity of the power supplies. The advantage of using a rectangular charging current over a triangular one is that for rectangular wave I_2 equals to the magnitude of i_2, so that we can achieve the same I_2 with a relatively small i_2.

4.5.7 DC applied field case

All above experiments focus on AC applied magnetic field. To rule out the possibility that DC magnetic field may also work because of the field dependence of critical current of the bridge YBCO tape, DC applied field was also tested.

The waveform of applied field and secondary current is shown in Fig.4.30. A DC field of 0.5T was always applied when secondary current was in its negative half cycles.

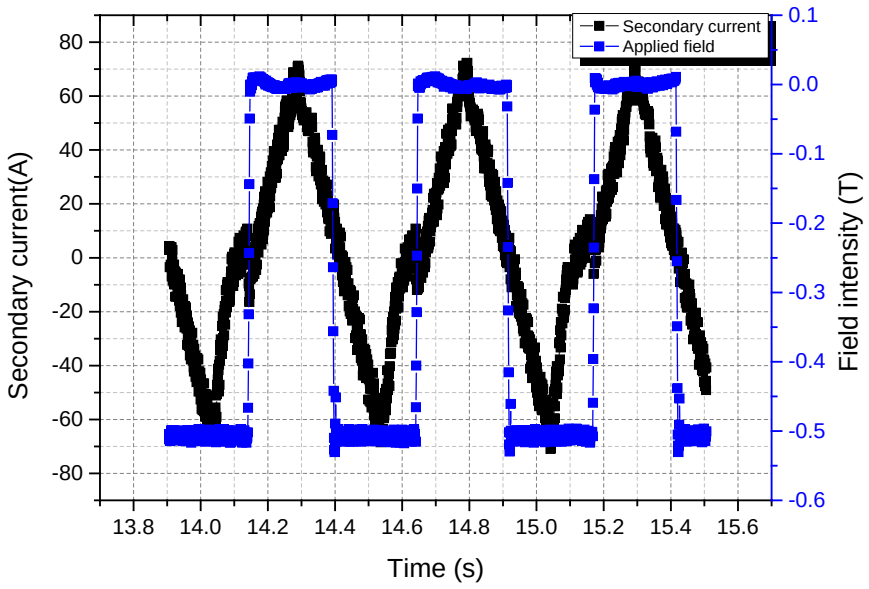

FIG. 4.30. Plots showing the waveform of secondary current and DC applied field.

The pumping result is presented in Fig. 4.31. To make a comparative study, the pumping result under 40Hz, 0.49T applied field is also plotted in the same figure (the load current curve under DC field is reversed to make an easy view). From Fig. 4.31, it can be seen that the AC field works much better than the DC field. It is interesting to see that the DC field also pumps the load current to about 8A, with a very slow speed. In fact, although the applied field is 'DC', there is still some hysteresis loss between the transport current and the applied field. This loss may contribute to the dynamic resistance (or it can be considered as transport AC loss). To prove this, both the secondary current and applied field frequency were increased to 30Hz, the result is also shown in Fig. 4.31. The final load current increased to 20A. To summarise, the experimental results have shown that AC applied field contributes most to flux

pumping. The results also show that a much higher frequency of the applied field than that of the secondary current is preferable, but not necessary.

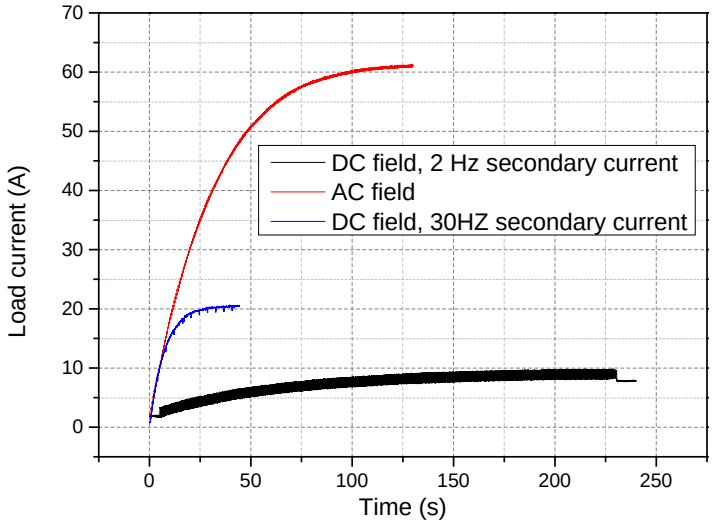

FIG. 4.31. Plots showing the load current curves under different AC and DC applied field.

4.6 Feedback control of the proposed flux pump [99]

The previous section shows the open loop operation characteristics of the proposed flux pump. In practical use, it is essential to operate the flux pump in controlled mode, for the following reasons. In open loop operation, the load current saturates at a certain value when the flux injection is counteracted by the flux leakage in the load loop. In many applications, however, the field is supposed to maintain at a required value. In this case, feedback control system is indispensable. The other reason is that continuous operation of flux pump is energy consuming. As the current decay in the HTS load is rather slow, it is unnecessary to continuously operate the flux pump. In the following part of this section, a feedback control system for the proposed flux pump was built and tested.

4.6.1 Control system and control algorithm

The experimental system was same as that in previous sections, except for two minor differences. The first was that the KEPCO powering the field magnet was replaced by an EP4000 audio amplifier. The second was that the joint resistance in the superconducting load loop was intentionally enlarged to about *1*μΩ. This was to make the decay faster, otherwise it would take too long for the load current to decay and the current signal change would be beyond the resolution of the Hall sensor. The picture of the new experimental system is shown in Fig. 4.32.

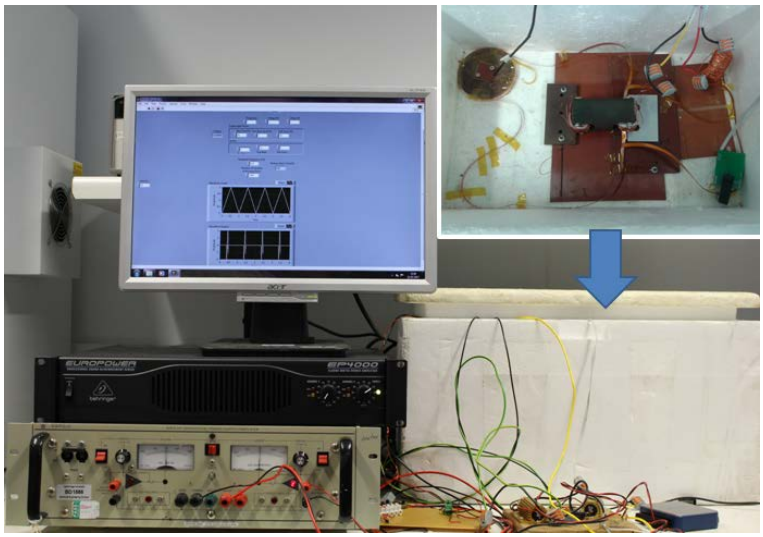

FIG. 4.32. Proposed flux pump system with feedback control.

A LabVIEW program was written to achieve real time feedback control logic. The input signal is the load current (voltage from the Hall sensor fixed in the centre of the load coil). The load current is firstly sampled and low-pass filtered by averaging the samples over each 1s. Then the filtered load current is compared with a preset current i_{preset}. If the load current is lower than the preset value, the flux pump remains in an on state, in which the DAQ card outputs desired analogue waveform to control secondary current i_2 and bridge field B_{app}. If the load current is over the preset value, two strategies are proposed: Strategy 1 is to set the controlling signals of i_2 and bridge field B_{app} both

zero, as shown in Fig. 4.33; Strategy 2 is to set controlling signal of i_2 zero and leave controlling signal of B_{app} as in flux pump mode. In the following we will show the results of these two control strategies.

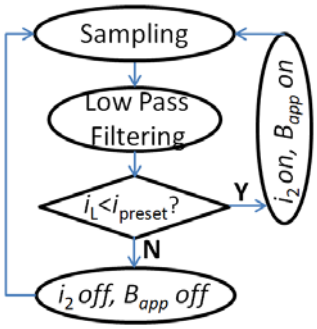

FIG. 4.33. Logic diagram of feedback control Strategy 1 of the flux pump.

4.6.2 Result

Fig. 4.34 shows the result using control Strategy 1.

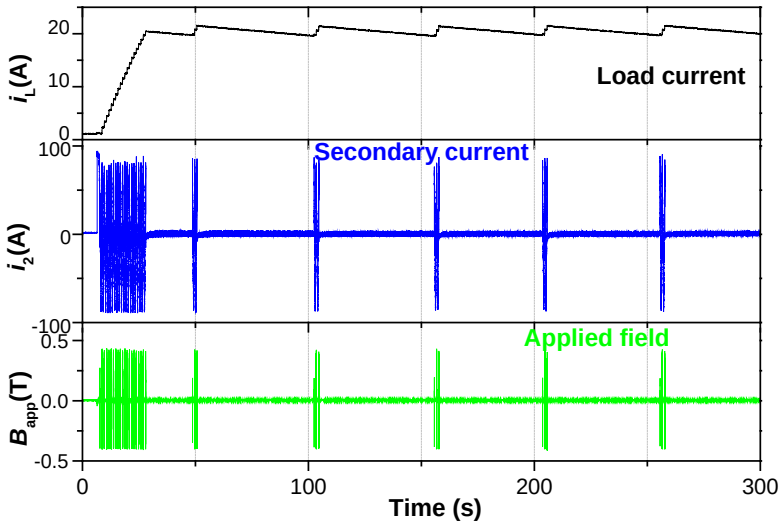

FIG. 4.34. Experimental result on stabilizing load current using control Strategy 1 described in Fig. 4.33. The top figure shows the load current curve where the load current i_L is pumped up and then stabilized at around 20A, the middle figure shows the waveform of the transformer secondary current i_2, and the bottom figure shows the waveform of applied field B_{app}.

The preset load current level was set to 20A. The top figure shows the load current i_L, the middle figure is the secondary current of the transformer i_2, and the bottom figure is the applied field B_{app}. In the beginning, the load current was pumped up from nearly zero to up to slightly above 20A. Then the flux pump was stopped by setting the transformer secondary current and the applied field to zero. Without the flux pump the load current gradually decayed until the current was lower than 20A. Then the flux pump was triggered again, and the current was pumped up to over 20A again. This process was repeated and the load current was stabilized at about 20A.

The details of waveforms during one start-up in Fig. 4.34 are shown in Fig. 4.35. The flux pump started up for about two seconds. During each cycle of the secondary current, the field was applied 10 cycles and the load current increased by about 1A. The flux pumped to the load during each field cycle was about 38μWb. This value can be further reduced by reducing the magnitude of i_2 or B_{app}.

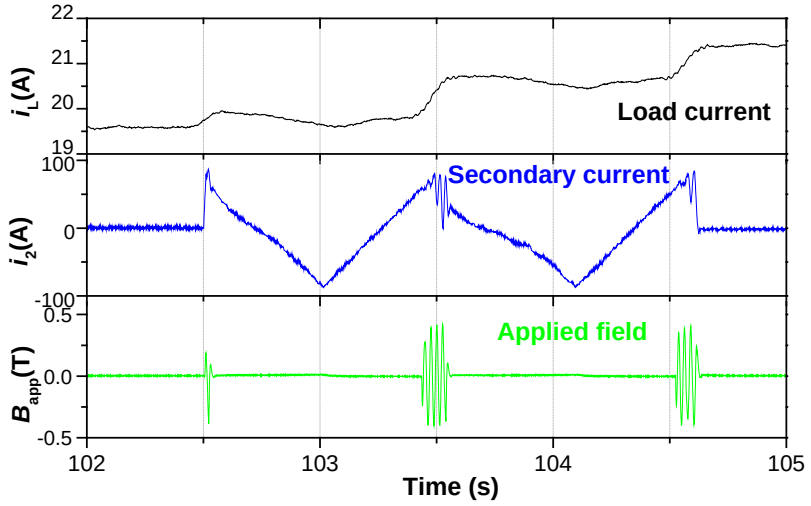

FIG. 4.35. Details of the waveforms in Fig. 4.34.

Fig. 4.36 shows the result of load current with different preset levels, together with a load current curve under no feedback control. All curves nearly overlap at the beginning of charging. Each curve stabilizes at the preset level. The flux pump starts

more frequently when the preset current level is higher. This is because the load current decays faster when it is at a higher value.

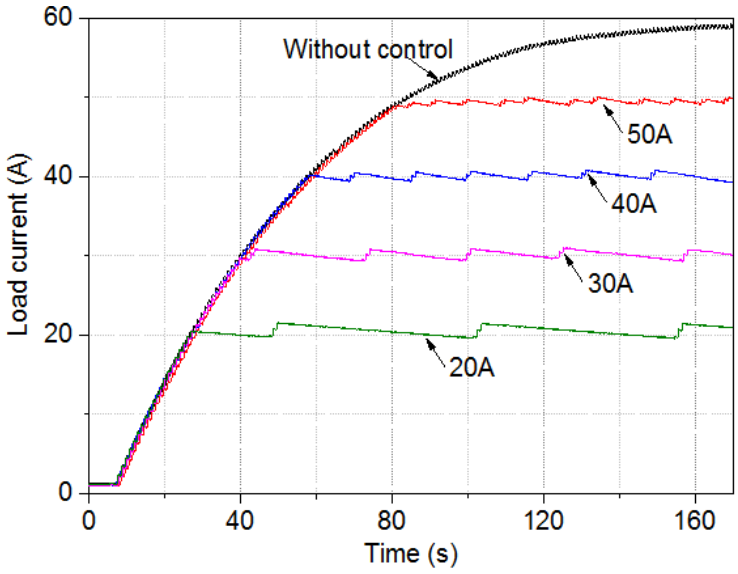

FIG. 4.36. Plots show the load current curves with various preset levels, together with a load current curve under no feedback control for comparison.

Control Strategy 1 is suitable for stabilizing the load current from a lower level to a higher level. However, it is not suitable for changing load current from a higher level to a lower level, because it cannot pump flux out of the load. To deal with the problem, control Strategy 2 was proposed. The logic is when the load current value is lower than the preset level, the flux pump is started, which is the same as that described in Strategy 1;when the load current value is higher than the preset value, the secondary current i_2 is set zero, but the field is still applied to the bridge superconductor. The applied field induces a flux flow out of the load, thus reducing the load current quickly.

The current and field waveforms of using Strategy 2 are shown in Fig. 4.37.

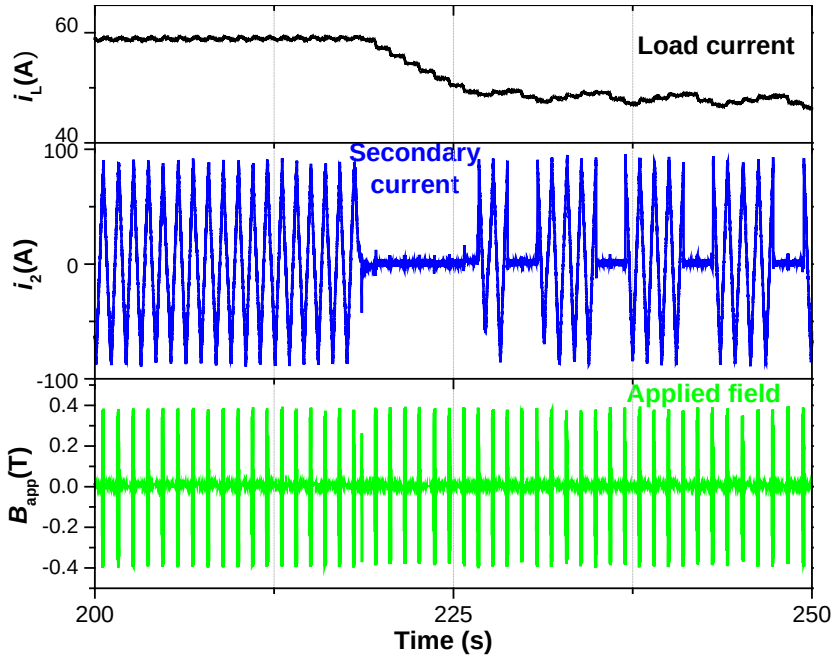

FIG. 4.37. Experimental result on stabilizing the load current using control Strategy 2. The top figure shows the load current curve where the load current decreases from around 60A to a stabilized value of about 45A, the middle figure shows the waveform of the transformer secondary current i_2, and the bottom figure shows the waveform of bridge field B_{app}.

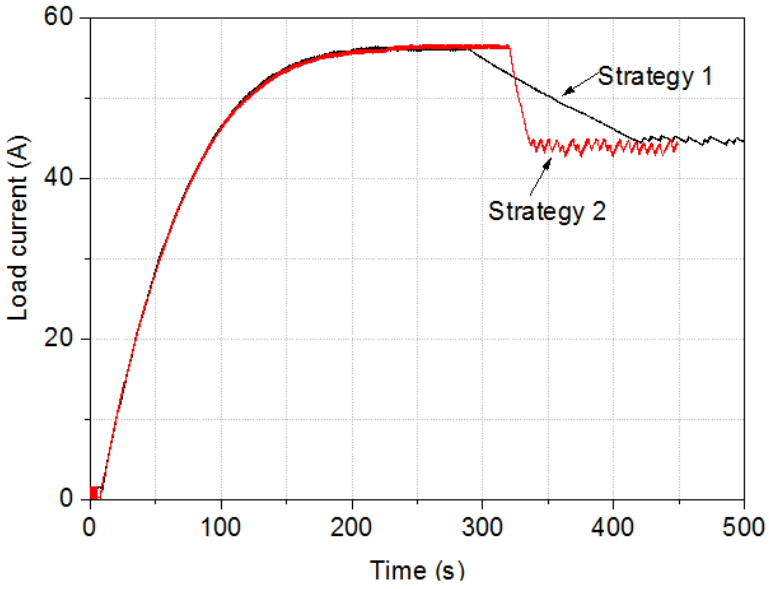

FIG. 4.38. Comparison between load curves under control Strategy 1 and Strategy 2.

Fig. 4.38 shows a comparison between these two control strategies in stabilizing load current from a higher level to 45A. We can see that Strategy 2 stabilizes the load current much faster. The load current has to be reduced by the joint resistance of the coil for Strategy 1. Strategy 2, however, has much higher operating loss than Strategy 1, because the field is applied even without the secondary current.

Although the above results are preliminary, they have shown the feasibility of using a feedback control system to stabilize the load current at a preset level. To further reduce the load current ripple, more complicated algorithms as well as high precision sensors are required.

4.7 Using the flux pump to achieve a quasi-constant voltage source

4.7.1 Three circuit models

It has been widely accepted that travelling wave based flux pumps can be equivalent to a circuit which consists of a constant DC voltage in series with a dynamic resistance, as shown in Fig. 4.39(a). From a circuit point of view, these flux pumps have two drawbacks. The first is that the output voltage reduces with the increase of transport current in the superconductor, and the maximum output current is limited by the dynamic resistance as V_{DC}/R_{dyn}(considering that $R_{dyn}>>R_L$). The second is that the loss generated in the circuit is proportional to the square of load current, which indicates that the loss becomes more and more significant when charging up the load current.

In contrast, the operation mode of the proposed flux pump in Section 4.4 can be considered as a circuit which consists of a constant DC current in parallel with an internal resistance, as shown in Fig. 4.39(b). Ideally, there is little loss in the circuit after the load being charged up. But in the beginning of charging, all current flows through the internal resistance, so the loss is high.

In a real application, it is sometimes desirable to achieve a power source which has constant DC voltage output, irrespective of output current level. In this way a constant rate of charging can be achieved. Another advantage of a constant output voltage is that the loss during charging is nearly constant, so that the heat load in cryogenic system is minimized. One equivalent circuit to achieve a constant voltage output could be like Fig. 4.39(c), in which the induced DC voltage is in parallel with the source resistance. In the following the author will exemplify how this is achieved.

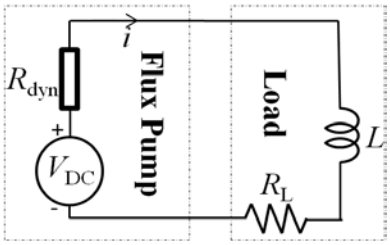

(a) Equivalent circuit of travelling wave based flux pumps.

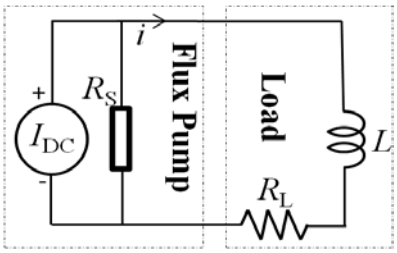

(b) Equivalent Circuit of the operation mode of the proposed flux pump in Section 4.4.

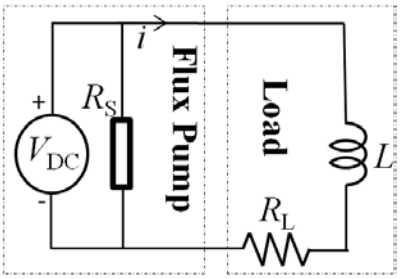

(c) Equivalent circuit of a constant voltage output of the proposed flux pump.

FIG. 4.39. Three circuit models of flux pumps.

4.7.2 Control strategy and control system

The output DC voltage of the flux pump can be expressed as:

$$V_{DC} = \frac{1}{T}\int_0^T i_B(t)R_B dt = \frac{1}{T}\int_{field\_on} i_B(t)R_{dyn} dt = pI_B R_{dyn} \qquad (4.10)$$

To achieve a quasi-constant AC output voltage, it is essential to make the average bridge current seen by the applied field constant over each cycle of secondary current. As the bridge current is the sum of secondary current and the load current, with the increase of the load current, a direct current bias will occur in the bridge current. To stabilize the average bridge current seen by the applied field, one way is to increase the magnitude of the primary current with the increase of load current, specifically:

$$I_{1\_mag} = 0.01 I_{2\_mag} = 0.01(i_L + I_B)/\alpha \qquad (4.11)$$

Where I_{1_mag} and I_{2_mag} is the magnitude of primary and secondary current respectively, α is the ratio of I_2/I_{2_mag}, and I_2 is the average secondary current when the field is on. Considering triangular wave of primary current is applied, bridge field is applied around the peak of secondary current, and the bridge field applied duration is 10% of a secondary current period, the ratio α is determined to be 0.9. The average bridge current I_B is a preset value, which determines the output DC voltage as shown in Eq. 4.10.

The control system is the same as that described in Section 4.6. The load current was firstly sampled and low-pass filtered by averaging the samples over each 1s. This value was used as an input to generate the primary current described by Eq. 4.11.

4.7.3 Results

Fig. 4.40 shows the waveform of load current i_L, secondary current i_2, and applied field B_{app}. The magnitude of the secondary current increases linearly at the beginning of charging, as predicted by Eq. 4.11. The load current also increases at a constant rate

in the beginning, indicating that the flux pump outputs a constant DC voltage. The result proves the feasibility of using the flux pump to output a quasi-constant voltage. Both of the magnitude of the secondary current and the load current saturate after they reach a certain value, this is because the current capacity limit of the bridge superconductor, which has been discussed in Section 4.5.

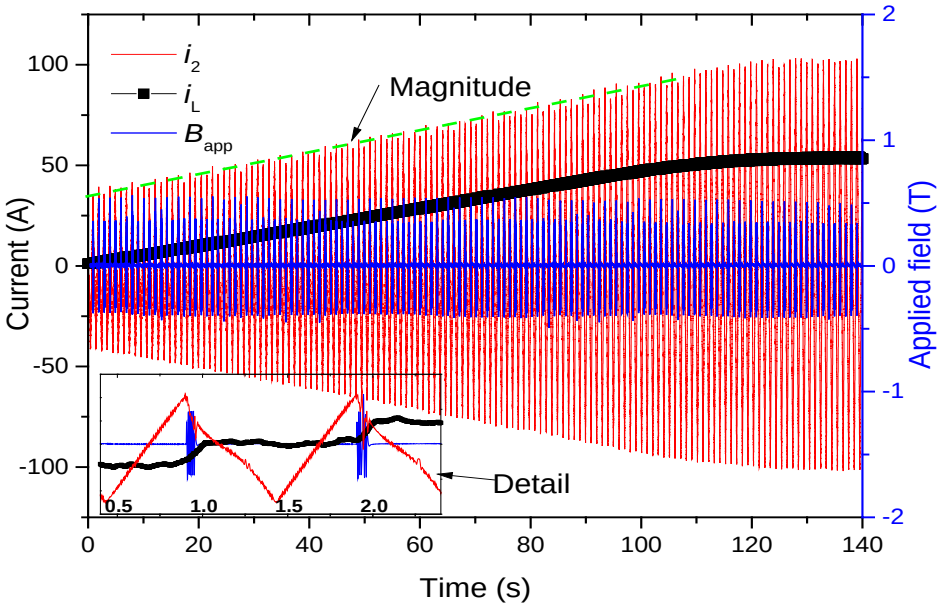

FIG. 4.40. Waveforms of i_2, i_L, and B_{app} under constant output voltage operation mode of the flux pump.

A clear comparison between the constant voltage output mode and the operation mode described in Fig. 4.39(b) is shown in Fig. 4.41.

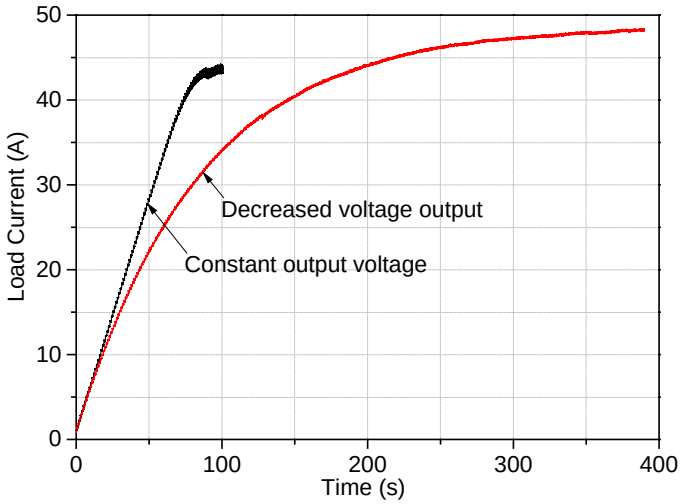

FIG. 4.41. Load current comparison between constant voltage output and the operation mode described in Section 4.4.

Initially the two curves have the same slope, because the values of initial output voltage in the two measurements are the same. The output voltage reduces in the red curve because the voltage drop in the internal resistance, making it an exponential curve. In contrast, the black curve remains a constant slope for a long time until the load current saturates.

Fig. 4.42 shows load current curves under different values of average bridge current I_B. Other parameters are the same in the three measurements. Three values of I_B are chosen as 18A, 36A, and 54A. The values of output voltage are roughly 1:2:3. The final load current under lower value of I_B is higher, which is also because the current capacity of the bridge superconductor.

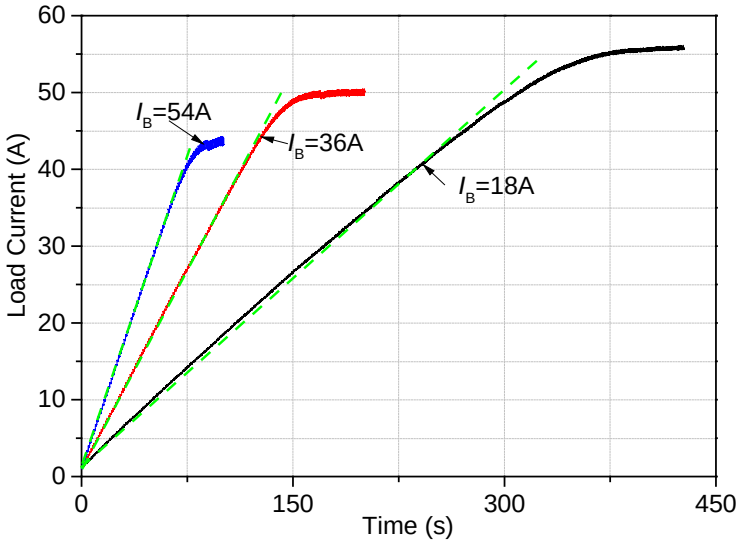

FIG. 4.42.Load current curves under different values of I_B.

Fig. 4.43 shows the load current curves under different applied field magnitudes. Larger field magnitudes correspond to a faster charging and a higher saturated current, because the field magnitude is closely related to the dynamic resistance and the output voltage.

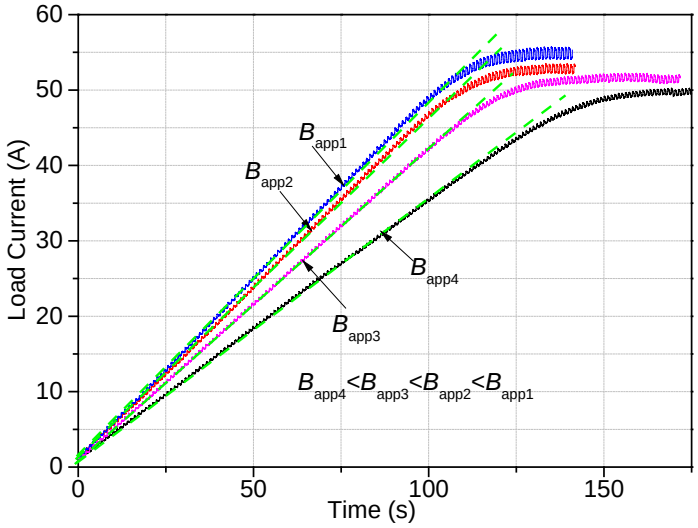

FIG. 4.43. Load current curves under different bridge field magnitudes.

Although the instantaneous output voltage value is not constant, the average voltage value over each secondary current cycle is. Therefore the flux pump can be considered as a quasi-constant DC voltage supply. If a bridge superconductor with a

larger current capacity is used, it is possible to achieve quasi-constant DC voltage output over a wide range of load currents. It may become a useful equipment in various superconducting applications.

4.8 Loss analysis

The efficiency of the flux pump is an important issue. The loss in charging up a magnet is quite different from that in maintaining a stable field. Therefore, these two types of loss are discussed separately in this section.

4.8.1 Loss classification

The total loss of the flux pumping system can be divided into two categories: loss in the superconducting circuit, and loss in electromagnets including the transformer. Three sources of loss contribute to the total loss in the superconducting circuit: transport AC loss in the secondary winding of the transformer, dynamic resistance loss of the bridge superconductor (loss caused by flux flowing across the bridge), and magnetization AC loss in the bridge superconductor (loss caused by hysteretic magnetization in the area without transport current). The loss in the electromagnets includes copper loss of the transformer primary winding and the field magnet winding, and hysteresis loss in the transformer core and field magnet core.

In charging up the load coil, the flux pump works in continuous mode; whereas in stabilizing the load current, the flux pump can work intermittently. Therefore charging up the load incurs much greater loss than maintaining the load field. In the following these two cases will be discussed separately.

4.8.2 Loss estimation of the flux pump in maintaining a field

Basic assumption

In the following we calculate the loss of the flux pump in maintaining current in a magnet, using control Strategy 1 described in Section 4.6. The equivalent resistance of the load is denoted by R_L. The load inductance is denoted by L, which is high enough so that the load current decay is slow. The load current is I_L, and the bridge current experiencing applied field is I_B. The magnitude of the secondary current I_{2_mag} is assumed to be $2I_L$, and the frequency of the secondary current is 1Hz. The bridge field has a magnitude of 0.3T and a frequency of 100Hz. The maximum load current fluctuation ratio allowed is I_Δ. It is also considered that the flux pump is able to compensate the current decay during one cycle of secondary current.

Loss estimation in superconducting circuit (P_{scon})

The transport loss in the secondary winding (P_2): the length of the secondary winding is about 1m, this loss can be estimated according to Ref. [100], and it is denoted as P_{trans} if the secondary current is continuous. The flux dissipation speed is $d\Phi/dt=I_L R_L$. Considering the flux fluctuation limit is $I_L I_\Delta L$ and assuming this amount of flux can be compensated in 1 second, the least time proportion for the flux pump to operate is $|I_L R_L/(I_L I_\Delta L)|= |R_L/(I_\Delta L)|$. Where $|R_L/(I_\Delta L)|$ is the absolute value of $R_L/(I_\Delta L)$, and it is only a number without a unit. The actual transport AC loss in the secondary winding is:

$$P_2=P_{trans}|R_L/(I_\Delta L)| \qquad (4.12)$$

The dynamic resistance loss on the bridge superconductor: to stabilize load field, the flux dissipation speed $d\Phi/dt=I_L R_L$ should be equal to the flux flow speed across the bridge on average. The energy dissipation caused by the dynamic resistance is $I_B\Phi$, and the average loss is:

$$P_d=2\times d\left(I_B\Phi\right)/dt=2\times I_B d\Phi/dt=2I_B I_L R_L \qquad (4.13)$$

This loss is considered twice because the amount of flux that flows across the bridge should be equal to the amount of flux that flows into the charging loop formed by the secondary winding and the bridge.

There is also a magnetization loss in the bridge superconductor, in the region where there is no transport current. As shown in Fig. 4.44, during an AC field cycle, there is net flux flow across the superconductor in the central area where the transport current flows. The net flux flow give rises to dynamic resistance loss; whereas in the outer areas of the superconductor, there is no transport current. Flux enters and exits the areas causing an AC magnetization loss.

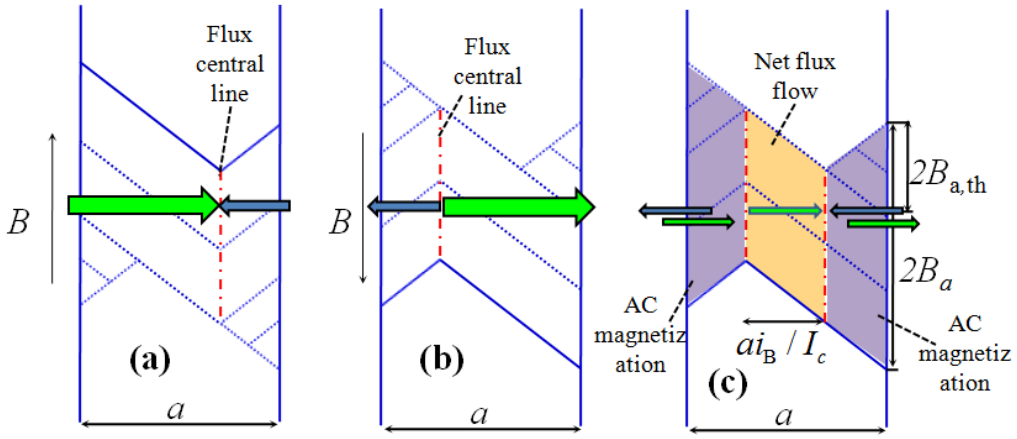

FIG. 4.44. Flux motion and magnetization loss in a DC carrying superconducting slab under perpendicular AC field. The geometry is the same with Fig. 4.4, where *a* is the width of the superconductor. (a) during applied field increasing, flux enters the superconductor from the left edge more than from the right edge, (b) during applied field decreasing, flux exits the superconductor from the right edge more than from the left edge. (c) loss in an AC field cycle, where there is transport current, there is a net flux flow and associated dynamic resistance loss; where is no transport current loss, there is AC magnetization loss.

The loss caused by the magnetization loss on the bridge P_{magnet} is influenced by the transport current level with respect to the critical current of the bridge. The increase of

transport current results in a reduced magnetization loss. The loss P_{magnet} is similar with P_d when the bridge current magnitude is half of the critical current of the bridge.

Therefore the total loss in superconducting circuit of the flux pump is mainly contributed by transport loss in the secondary winding of the transformer, the dynamic resistance loss on the bridge, and the magnetization loss on the bridge, it is written as:

$$P_{scon} = P_2 + P_d + P_{magnet} \approx P_{trans} \left| R_L / (I_\Delta L) \right| + 2I_B I_L R_L + 2I_B I_L R_L \qquad (4.14)$$

Loss estimation in electromagnets (P_{em})

The resistance of the transformer primary winding is 0.6Ω @ 77K, and the primary current has a $0.02I_L$ peak value to generate a $2I_L$ secondary current. Considering the average operating time ratio is $R_L/I_\Delta L$, this loss is:

$$P_{trans\_copper} = \frac{1}{2}(0.02I_L)^2 0.6\Omega * R_L / (I_\Delta L) \qquad (4.15)$$

The resistance of field magnet is 2.2Ω @ 77K, with a 1.5A current to generate 0.3T field. Considering each field cycle the flux injection is:

$$\Phi_{per\_cycle} = 2B_a a L I_B / I_C \qquad (4.16)$$

The copper loss in the field magnet is:

$$P_{mag\_copper} = \frac{1}{2}(1.5\text{A})^2 \times 2.2\Omega \times I_L R_L / (\Phi_{per\_cycle} \times 100) \qquad (4.17)$$

The transformer can be considered nearly shorted because the dynamic resistance value is very low. So the flux density in the iron core is very low, thus the hysteresis loss can be neglected.

The field magnet core is made of laminated silicon steel, which has a loss of about 0.4 watts per pound at 60Hz, 1.5T [101]. Considering weight of the core is about one

pound, the field in it is only 0.3T, and it operates very infrequently. This loss is negligible.

Therefore, the total loss of electromagnets is mainly contributed by copper windings of the transformer and the field magnet, which is expressed as:

$$\begin{aligned} P_{\text{em}} &= P_{\text{trans\_copper}} + P_{\text{mag\_copper}} \\ &= \frac{1}{2}(0.02I_{\text{L}})^2 0.6\Omega \times |R_{\text{L}} / (I_{\Delta} L)| + \frac{1}{2}(1.5\text{A})^2 \times 2.2\Omega \times I_{\text{L}} R_{\text{L}} / (\Phi_{\text{per\_cycle}} \times 100) \end{aligned} \tag{4.18}$$

Case study

Assuming that R_{L}=0.1$\mu\Omega$, L=1H, I_{L}=50A, $I_{2\text{peak}}$=2I_{L}, I_{Δ}=1/million, and I_{B}=50A, the loss in the superconducting circuit is:

$$P_{\text{scon}} = P_2 + P_{\text{d}} = P_{\text{trans}} |R_{\text{L}} / (I_{\Delta} L)| + 4 I_{\text{B}} I_{\text{L}} R_{\text{L}} = 2\text{mW} \tag{4.19}$$

Where P_{trans} is 1mW according to the result in Ref. [100], considering the transport current is 100A at a frequency of 1Hz.

The total loss in the electromagnets is:

$$P_{\text{em}} = P_{\text{trans\_copper}} + P_{\text{mag\_copper}} = 0.03\text{W} + 0.01\text{W} = 0.04\text{W} \tag{4.20}$$

Where $\Phi_{\text{per\_cycle}}$ is chosen to be 10μWb considering the geometry of the magnet, field magnitude, and critical current of the bridge superconductor.

4.8.3 Loss analysis of the flux pump in charging up a magnet

There are different strategies in charging up a magnet, as shown in Section 4.7. Here only constant voltage output mode (Fig. 4.39(c)) is discussed.

Loss in superconducting circuit

As the load inductance L and the bridge dynamic resistance R_{B} is much larger than the load resistance R_{L}, flux leakage and associated loss is neglected in the load. The

final load current is assumed to be I_L, and the charging time is assumed to be T_{charge}. Therefore, the power loss in the bridge superconductor is $(LI_L/T_{charge})^2/R_B$. The actual loss in the charging loop should double this number because the same amount of flux has to flow in the charging loop as the flux flow in the load loop, and we assume that these two losses are the same for simplicity. This loss dominates the total loss in the superconducting circuit, as other losses such as transport AC loss in the secondary winding, magnetization AC loss in the bridge (assuming that the transport current in the bridge is close to the critical current of the bridge), and loss in the load are neglected. Therefore the total loss in superconducting circuit is roughly:

$$P_{scon}=2(LI_L/T_{charge})^2/R_B \qquad (4.21)$$

As can be seen from Eq. 4.21, the loss is proportional to the square of charging speed, and it is inversely proportional to the dynamic resistance in the bridge.

The total energy consumption is $2(LI_L)^2/(T_{charge}R_B)$, and the total stored energy in the load is $0.5L(I_L)^2$, so the loss to stored energy ratio is $4L/(T_{charge}R_B)$. To reduce this ratio, it is preferred to have a long charging time and a large dynamic resistance.

Loss estimation in the electromagnets

As analyzed above, the loss in the electromagnets mainly come from the copper loss of the transformer and the field magnet. It is estimated to be several Watts even if we consider both the transformer and the field magnets are in continuous operation.

4.8.4 Loss comparison with current leads or rotating magnets based flux pump

The heat loss of using a pair of current leads to power the magnet at 50A is about 2.5W [102]. Using a rotating magnets based flux pump will incur a loss of more than 0.3W [67], excluding the loss caused by the moving parts (continuous operation is considered because acceleration and deceleration of the motor would cause huge

fluctuation in load current). The actual loss caused by the moving parts will be rather high. In comparison, the proposed flux pump using feedback control only has a loss of 2mW in superconducting circuit, and a total loss of 0.04W even if the electro-magnets are in Liquid Nitrogen environment. Loss in the proposed flux pump is much smaller than rotating magnets based pump. This is because on one hand the proposed flux pump does not need to work continuously to maintain a field, and on the other hand unlike rotating magnets based pump, in the proposed flux pump load current does not flow through the bridge when the field is applied, thus significantly reducing the transport loss on the bridge. The proposed flux pump is therefore ideal in maintaining a field.

4.9 Conclusion

In this chapter, the author has proposed and experimentally verified a novel HTS flux pumping mechanism. The well-known effect that flux flow can be triggered when a DC carrying type-II superconductor is subjected to a perpendicular AC field was used. In the flux pump, a transformer was used to generate an alternating current with high magnitude and low frequency in its secondary winding. A load was connected across the secondary winding, and an HTS bridge was used to short both the secondary winding and the load. An AC magnetic field was intermittently applied perpendicularly to an HTS bridge, when the transporting alternating current in the bridge reached one polarity, thus resulting in a unidirectional flux flow in the HTS bridge. Flux gradually accumulated in the superconducting load. The load current saturated when flux injected into the load was balanced by the flux consumption in the load. The results have clearly shown that flux pumping can be achieved without driving superconductor normal, which is a significant theoretical breakthrough.

The author experimentally examined the influential factors on the flux pump. These factors include secondary current magnitude and waveform, bridge field magnitude,

frequency and duration, phase difference between current and field. The flux pump is very easy to control. The pumping speed can be adjusted by changing the bridge field magnitude, frequency or duration. The final achievable load current can be controlled by changing secondary current magnitude, bridge field, or their phase difference. All the result well validated the previously proposed analytic model.

A feedback control system was developed, by which the load current can be stabilized at a preset level with minimized loss. With the help of the feedback control system, a constant voltage output mode was achieved. The flux pump makes quantitative flux injection possible. In the future it is possible to achieve micro-Wb flux injection, which can be used to generating extremely stable magnetic field in HTS magnets.

Finally the loss in the flux pump was calculated and compared to using current leads and using a rotating-magnets based flux pump. It has been shown that the proposed flux pump has much lower losses compared with rotating magnets based flux pumps or current leads in stabilizing field.

The relationship between the proposed flux pump and existing travelling wave flux pumps will be revealed in Chapter 6.

Chapter 5
An HTS Flux Pump Operated by Directly Driving Superconductor into Flux Flow Region in the *E-J* Curve

5.1 Introduction

In the previous chapter, it has been shown that flux pumping can be achieved using AC field triggered flux flow, and that it is not necessary to drive high T_c superconductors normal to achieve flux pumping. In fact, as long as there is flux motion, flux pumping could be achieved. Flux motion occurs when a type II superconductor is subjected to an AC field, transporting an alternating current, or transporting a direct current above its critical current. In Ref. 103, Ref. 104, the authors proposed a self-switching LTS flux pump, which depends on making superconductor normal by driving current above the critical value. Following their work, in this chapter, the author will show that for an HTS flux pump, it can also work by driving high T_c superconductors into the flux flow region in the *E-J* curve. The performance of the flux pump under different operating conditions will also be presented.

5.2 Basic principle

As shown in Fig. 5.1(a), a varying magnetic field is applied to an HTS loop (in yellow) which includes a resistive joint. An alternating current $i(t)$ circulating the loop is induced by the changing magnetic field. A superconducting load L which we want to magnetize is connected to branch *ab*. The branch has a much lower critical current than the rest of the HTS loop. If there is a continuous net flux flow across branch *ab*, there is an associated voltage $v(t)$ across branch *ab* which has a DC value. Flux accumulates in

the load L and it can be charged. In the following we will explain how the net flux flow across branch *ab* is achieved. If we properly coordinate the resistance and inductance of the HTS loop, as well as the changing rate of the applied field, we can achieve an asymmetrical $i(t)$ which has zero DC value. The *V-I* curve of branch *ab* and one example waveform of the periodical circulating current $i(t)$ is plotted together in Fig. 5.1(b). During each cycle of $i(t)$, at region *A* and only region *A*, the critical current of the bridge superconductor I_c has been exceeded, the superconductor is in flux flow region, and a voltage developed across the load. The remainder of the waveform is arbitrary save that $abs(i(t))<I_c$ and the integration of $i(t)$ over each period is zero. Therefore, during each cycle, there is a net flux flowing across branch *ab*, and the DC voltage across branch *ab* is non-zero. The superconducting load inductor which is connected to branch *ab* is hence gradually charged.

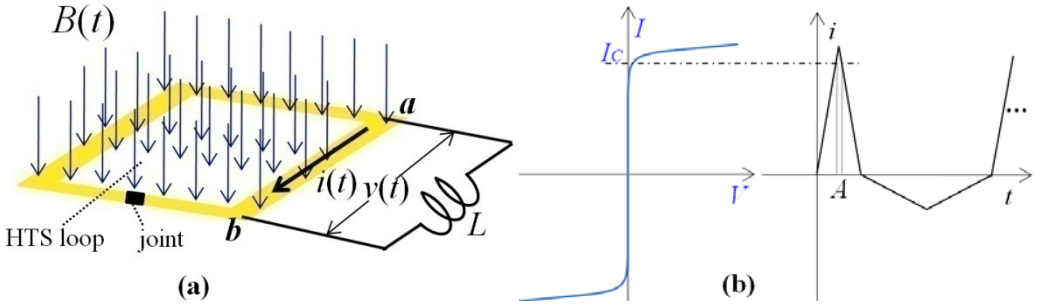

FIG. 5.1. Basic principle of the proposed HTS flux pump. (a) A varying magnetic field is applied to an HTS loop which consists of a resistive joint. A superconducting load L is connected to branch *ab* which has a smaller critical current value than the rest of the HTS loop. (b) the V-I curve of branch *ab* (left), and one example waveform of the circulating current $i(t)$ (right). During each cycle of $i(t)$, at region *A* and only region *A* the critical current of branch *ab* has been exceeded and a voltage developed across the load. For the remainder of the waveform, $abs(i(t))<I_c$.

In the following, an experimental system is built to verify the proposed principle.

5.3 Experimental system

5.3.1 The circuit

A Superconducting circuit was built up, as shown in Fig. 5.2. A 200:2 transformer was used to induce an alternating current with high magnitude in its secondary winding. The secondary winding was made from two parallel 6mm YBCO tapes with a total critical current of 360A. Two ends of the secondary winding were soldered together via another piece of 6mm YBCO tape which we refer to as "the bridge". The soldering process can be found in Ref. [44]. The bridge length was 10cm and it had a critical current of 180A. The bridge was also used to short an YBCO double pancake load coil. The inductance of the coil was 0.388mH. The critical current of the coil was 81A. Other specifications of the coil can be found in Section 3.3. All above critical current values were measured at the temperature of 77k with the criterion of $E_0=10^{-4}$V/m.

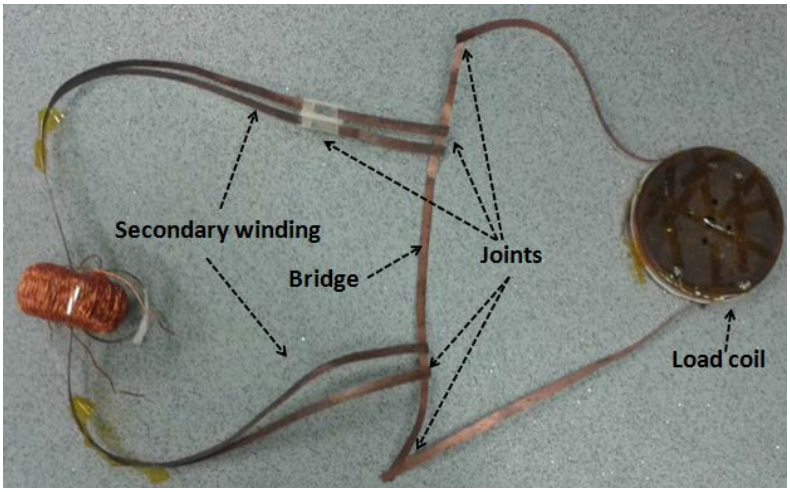

FIG. 5.2. Picture of the circuit of the proposed flux pump. The circuit consists of a 200:2 transformer, in which the primary winding is made of copper and the secondary winding is made of two 6mm wide YBCO CCs in parallel. A superconducting bridge shorts the secondary winding as well as an HTS load. The bridge has a lower critical current than that of the secondary winding.

5.3.2 Power supply, signal generation system, and measurement system

The primary winding of the transformer was powered by a KEPCO-BOP 2020 power amplifier. The KEPCO was controlled by an NI-USB 6002 data acquisition card which can output programmable analogue signal from LabVIEW software. The KEPCO worked in current mode, which means that output current is proportional to the input signal. In this way it was possible to generate a desirable primary current. The primary current i_1 was measured via a 0.47 ohm resistor in series with the primary winding, the secondary current i_2 was monitored by an open loop Hall Effect current sensor, load current i_L was measured by a pre-calibrated hall sensor fixed at the centre of the load coil. The sensors are the same with that described in Chapter 5. All analogue signals were sampled by the NI-USB 6002 card, with a sampling rate of 400Hz. The load current data were filtered by averaging every 5 continuous samples. The whole superconducting system was immersed in Liquid Nitrogen (LN_2).

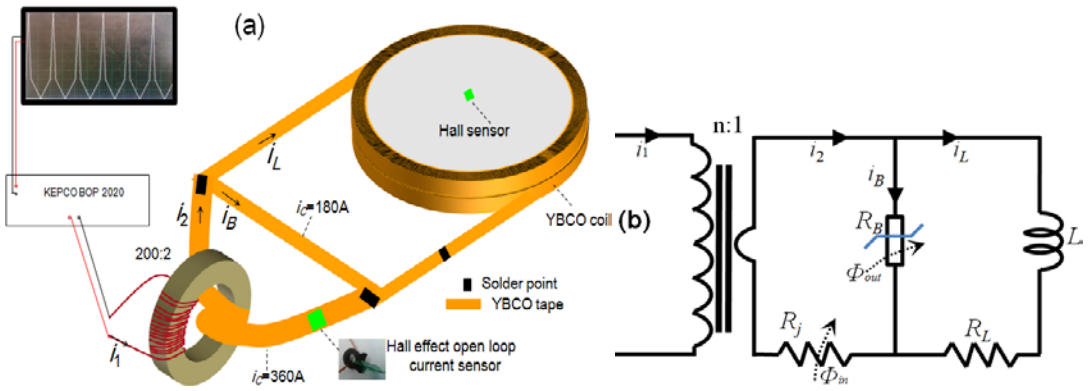

FIG. 5.3. Schematic drawing of the proposed flux pump system and its equivalent circuit. (a) Schematic experimental system. A transformer generates an asymmetrical current in its secondary winding which is shorted by the bridge. The bridge has a lower current capacity than the winding. When the secondary current i_2 exceeds the critical current of the bridge, flux will flow to the load via the bridge. (b) Circuit analogue of the system, where R_j denotes joint resistance, R_B denotes flux flow resistance of the bridge superconductor. The flux flow direction has also been drawn in the circuit.

The schematic drawing of the whole system is shown in Fig. 5.3(a). The equivalent circuit of the system is shown in Fig. 5.3(b). R_j represents joint resistance in the secondary winding, R_B denotes flux flow resistance of the bridge superconductor, R_L is an equivalent resistance in the load loop which includes joint resistance and other losses, and L is the load inductance. The bridge inductance is too small to be considered. It should be noted that the joint resistance R_j is essential to damp down any direct current component in the secondary winding, otherwise the transformer iron core might be saturated. In the experiment, the total joint resistance was estimated to be R_j=10$\mu\Omega$. From a circuit point of view, the proposed flux pump is similar to the LTS flux pump in Ref. [103]. However, they are distinct from each other in terms of physics and control strategy. The origin of R_B in the manuscript is due to flux flow [25] of high-T_c superconductor, while in Ref. [103] it depends on driving the low-T_c superconductor normal.

5.4 Experiments and result

5.4.1 Primary current setting and charging details

In the experiment, an alternating triangular signal has been used to control the primary current i_1. During the period when i_1 is positive, i_1 ramps up to a peak value I_{1pp} at a constant rate, and then ramps down with the same rate to zero; during the period when i_1 is negative, i_1 ramps down to a negative peak value of $-I_{1np}$, and then ramps up with the same rate to zero again. The length of positive period over the length of negative period is inversely proportional to I_{1pp}/I_{1np}, thus making the dc component in i_1 equals to zero, i.e.:

$$\int_0^T i_1(t)dt = 0 \qquad (5.1)$$

Where T is the period of i_1.

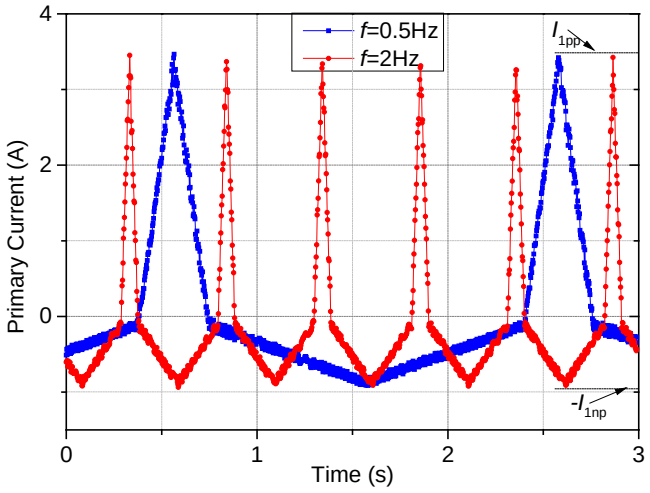

FIG. 5.4. Waveform of primary current of the transformer i_1, with frequency f=0.5Hz and f=2Hz. I_{1pp} denotes the positive peak value of i_1, and $-I_{1np}$ denotes the negative peak value of i_1.

In the following experiment, the controllable parameters include the current positive peak value I_{1pp}, the negative peak $-I_{1np}$, and the current frequency f. Fig. 5.4 shows two waveforms with the same peak values but at different frequencies.

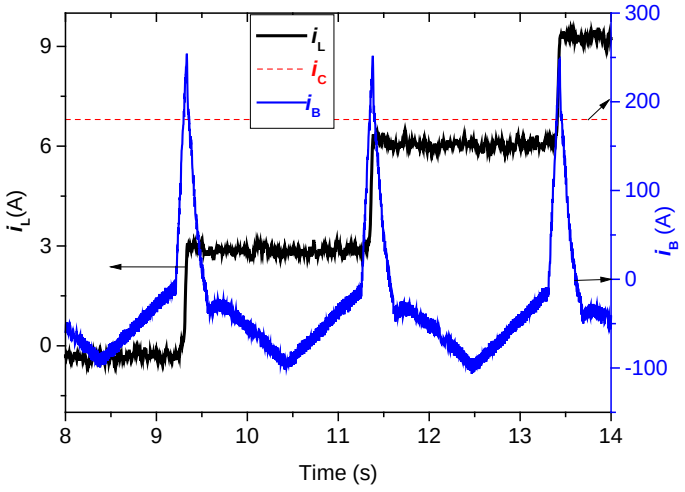

FIG. 5.5. Detailed Waveform of bridge current i_B, load current i_L, and critical current of the bridge i_C.

Fig. 5.5 shows the detailed waveform of bridge current i_B and the load current i_L. The positive peak current of i_B is about 250A, and the negative peak value of i_B is around

-100A. The critical current of the bridge superconductor i_C is 180A, which is in between the positive peak value and the negative magnitude (absolute value). As can be seen from Fig. 5.5, at each period when the bridge current exceeds i_C, the load current increases by about 3A; during the rest of i_B cycle, the load current nearly remains stable. The average voltage across the bridge can be expressed as:

$$V = \frac{1}{T_{ff}} \Delta i_L \times L \qquad (5.2)$$

Where T_{ff} represents the duration when the bridge superconductor is in flux flow region in each current cycle, and it is about 0.1s in Fig. 5.5. Δi_L denotes the current increase in each cycle, and it is estimated to be 3A. L is the inductance of the load which is 0.388mH.

According to the above numbers, the voltage V is estimated to be 11.64mV. The electric field is then calculated to be 1.16mV/cm. If all of the current had migrated to the copper layer, the electric field would be over 40 mV/cm, which is much larger than 1.16mV/cm. Therefore the superconductor is far from normal.

5.4.2 Load current under different primary current magnitudes

For an ideal transformer, its secondary current i_2 is always proportional to the primary current i_1. However, for a real transformer, if the load impedance is high, the output voltage may reach its limit so that the secondary current cannot follow the primary current. In this section, the influence of primary current magnitude on the load current will be studied, since the bridge resistance originally depends on the primary current.

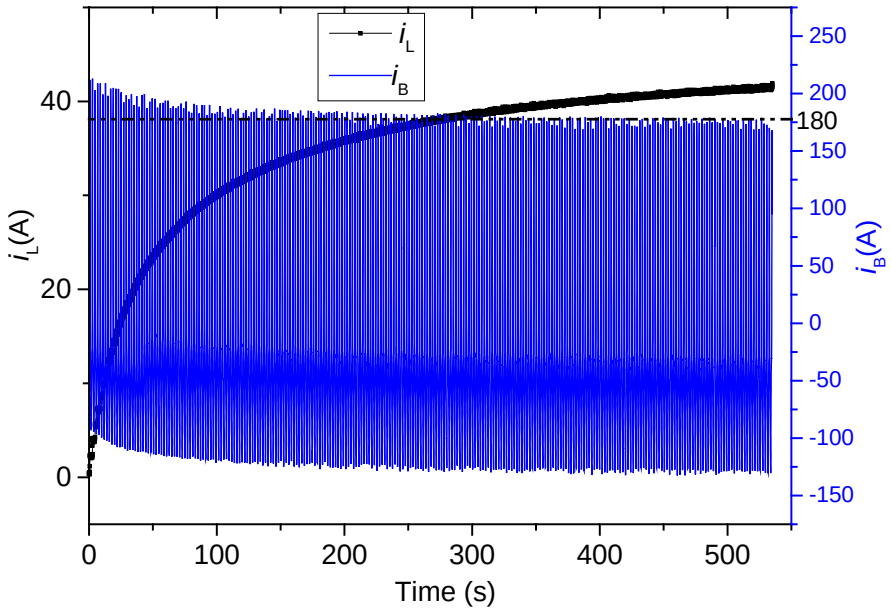

FIG. 5.6. Waveform of bridge current i_B and load current i_L during the whole charging process. The primary current is low, so that the bridge current i_B reduces with the increase of load current. The load current cannot reach the critical current of the coil. It stabilizes at a level where the positive peak value of the bridge current approximately equals to the critical current of the bridge.

If the positive peak of primary current I_{1pp} is relatively too low to make the bridge voltage reach the limit, then the secondary current is proportional to the primary current with a ratio of 100:1. The charging curve is shown in Fig. 5.6. At the beginning of the charging process, the secondary current i_2 equals to bridge current i_B because load current i_L is zero. With the increase of i_L, i_B is gradually biased to the opposite direction. In this case the bridge DC voltage also drops with the increase of load current. Therefore, the load current presents a curve which is like the charging curve of a first order circuit. When I_{1pp} is too low to drive the bridge to flux flow region, the load current tends to saturate at a value which is lower than the critical current of the load coil. Fig. 5.6 shows the case where the load current i_L saturated at 40A when I_{1pp} reduced to about 180A (the critical current of the bridge).

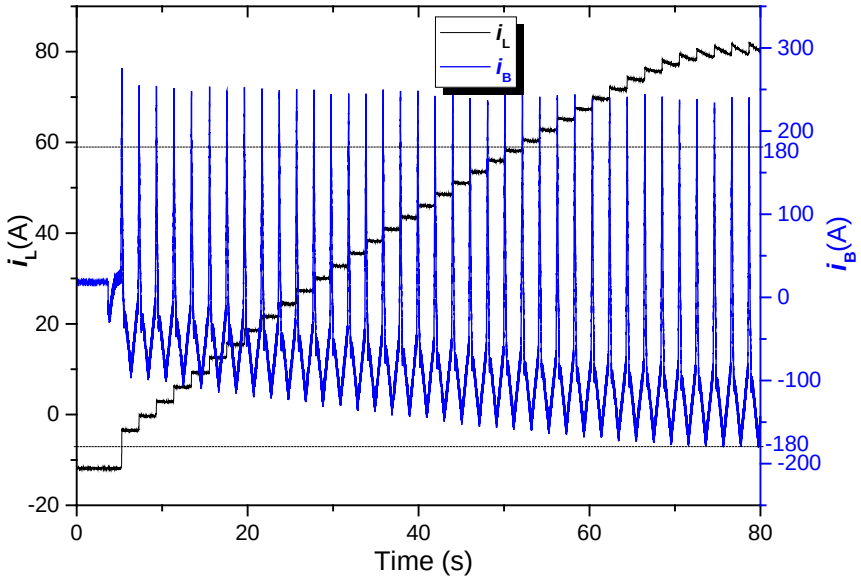

FIG. 5.7. Waveform of bridge current i_B and load current i_L during the whole charging process. The primary current is high, so that the bridge voltage is always limited by the capacity of the transformer during the whole charging process. The load current curve is nearly linear before reaching the critical current of the load coil.

In contrast, when the primary current level is high, the bridge voltage will reach its limit. This means that the bridge DC voltage in each cycle nearly remains constant. In this case, the positive peak value of the bridge current remains constant during the whole charging process as well. The charging process is shown in Fig. 5.7. During each cycle, the load current increases by the same amount, so the load current's rate of change is nearly constant until it reaches the critical current of the load coil, which is 81A in the experiment.

It should be noted that no matter whether the primary current is high or low, the negative magnitude (the absolute value) of the bridge current will increase with the increase of the load current. In the experiment, the load coil critical current is 81A, and the critical current of the bridge is 180A. To make sure that the negative magnitude of the bridge current will not exceed 180A, the negative magnitude of the secondary

current should be less than 99A. Fig. 5.7 shows the actual case where the load current reaches the critical value, and at the same time the negative magnitude of the bridge current reaches the bridge critical current.

Fig. 5.8 shows the load current curves under different primary current magnitudes. In all experiment, the negative magnitude of the primary current I_{1np} is set to be 1A.

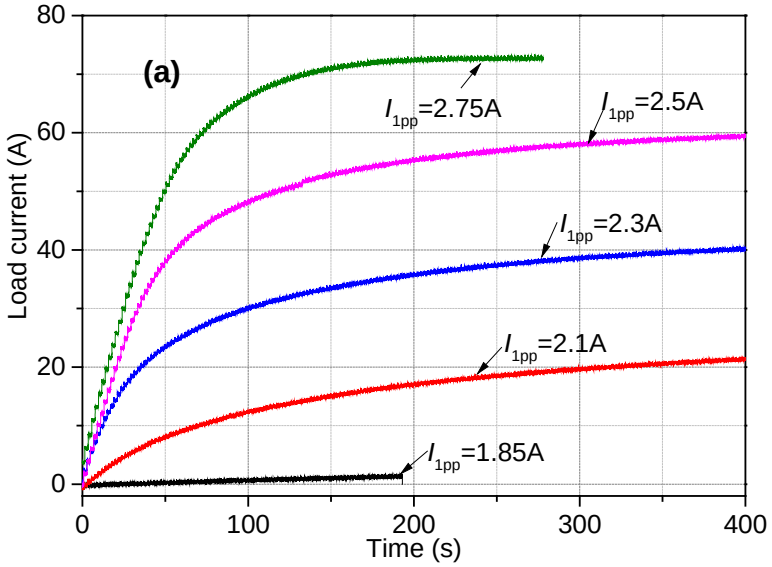

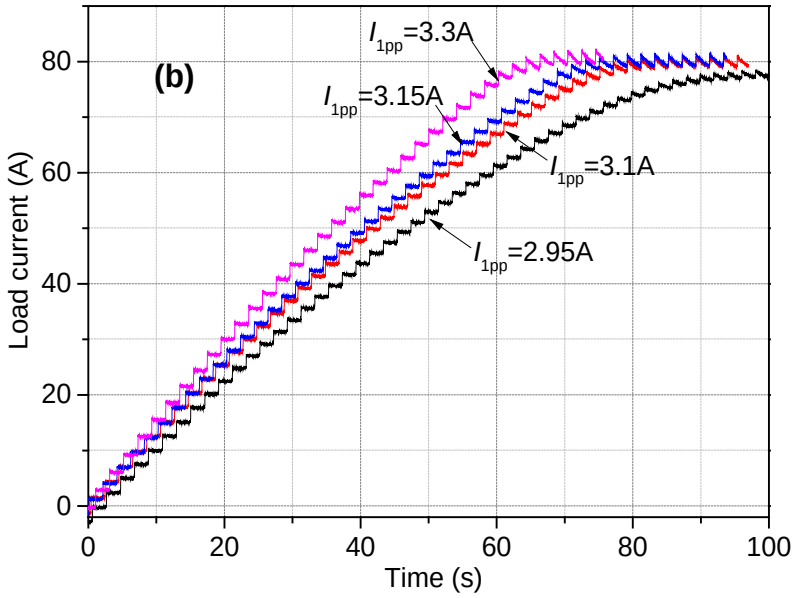

FIG. 5.8. Load current curves under different positive peak values of primary current I_{1pp}. The negative magnitude in all measurements is set as I_{1np}=1A. The frequency of the primary current is 0.5Hz.

5.4.3 Load current under different primary current frequencies

In this part of experiment, the aim is to test the frequency dependence of charging performance. During each measurement, the shape of the primary current was fixed. The frequency of primary current varies from 0.5 Hz to 16Hz. The waveform of primary current is shown in Fig. 5.9, where I_{1np}=1A, I_{1pp}=3.3A. Higher frequency was not tested due to the voltage limitation of the KEPCO.

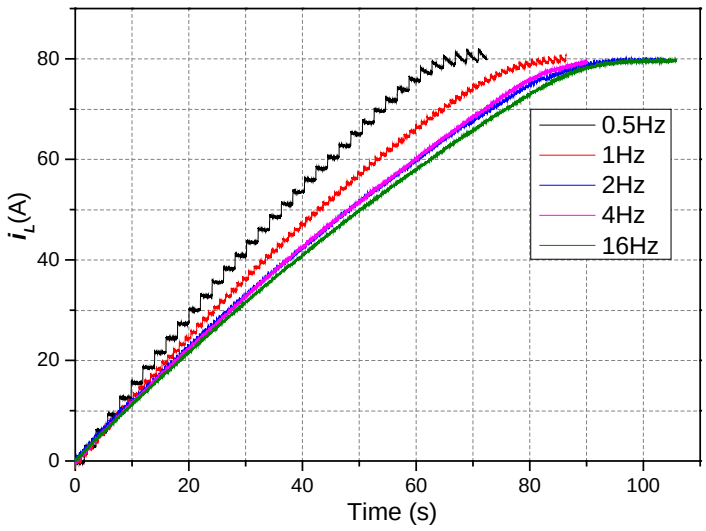

FIG. 5.9. Load current curves under different frequencies of primary current.

It can be seen from Fig. 5.9, all load currents saturate at about the critical current of the load coil, but the speed differs a little bit. The fastest charging is under 0.5Hz, followed by the 1Hz case, and the rest curves are nearly overlapped. Theoretically all curves should overlap together, if the *v*-*i* relationship of the bridge superconductor is independent of current frequency. This is because the waveforms of the primary current are the same except for the frequency, which means the amount of flux flow into the load should be the same during the same time period. However, in practice, the *v*-*i* relationship of the bridge superconductor depends on temperature. The flux flow during a certain time can be described as:

$$\phi = \int_0^P v(i,\ T)dt \qquad (5.3)$$

Where ϕ is the flux flow into the load, $v(i, T)$ denotes the instantaneous bridge voltage which depends on the bridge current i and temperature T, and time period P can be multiples of 2s (the period of 0.5Hz signal). It is understandable that lower frequency means a longer continuous time when the superconductor is in flux flow region during each AC cycle, and it is therefore easier for heat to accumulate in the bridge to cause a temperature rise (This is why the bridge superconductor cannot carry a DC as high as

the peak value of the AC in the bridge @ 77K). Temperature rise promotes flux flow and shifts the *v-i* curve. Therefore, at lower frequencies, the integration in Eq. 5.3 has a larger value, and the flux pumping is faster.

5.5 Discussions

In all previous HTS flux pumps magnetic fields have to be applied perpendicular to an HTS tape (tapes), which is difficult to achieve if the field magnets are outside the cooling system. Having field magnets in the cooling system, however, means more loss, especially for the moving ones. In contrast, the proposed flux pump only needs a single transformer to achieve flux pumping. It is not difficult to place the primary winding and the iron core of the transformer outside the cryogenic system. In this way the loss can be significantly reduced. The proposed flux pump is especially suitable for fast pumping up current in large magnets. The main limitation on pumping speed in this flux pump is the capacity of the transformer. In terms of field stability, however, this flux pump may not be very ideal. Because of the sharp *V-I* curve of the bridge superconductor, it is difficult to achieve an effective control of the bridge voltage. A small noise in the bridge current may induce a large error in the bridge voltage. To solve the problem, it is desirable to combine this flux pump with the dynamic resistance controlled flux pump [97, 98], in which case this flux pump can be used to ramp up the load current and the dynamic resistance controlled flux pump can be used to stabilize the final field.

5.6 Conclusion

In this Chapter, the author has presented the principle and experimental results for an HTS flux pump. The flux pump consists of a transformer with a superconducting secondary winding which is shorted by a piece of YBCO coated conductor referred as

“the bridge”. The transformer generates a high secondary current with its positive peak value much larger than the negative peak value. During each cycle, around the positive peak of the secondary current, the bridge superconductor is driven into the flux flow region, during the rest of the cycle the bridge remains superconducting. Flux is then accumulated in the load.

The author tested the performance of the flux pump under different primary current magnitudes and frequencies. The results show that the performance is more dependent on the primary current magnitude but less on the current frequency. The load current can be easily charged to the critical value. The work makes flux pumping for HTS CC coils much simpler than ever before.

Chapter 6
Origin of DC Voltage in Travelling Wave Flux Pumps: Field, Field Rate of Change, and Current Density Dependence of Resistivity

6.1 Introduction

During this decade, several High-T_c Superconducting (HTS) flux pumps based on travelling magnetic field have been developed for CC coils [52, 62, 66, 79]. These flux pumps use a piece of CC (CCs) connecting to a superconducting load. When travelling magnetic field generated either by rotating permanent magnets or by linear electromagnets passes across the CC, flux gradually accumulates in the load, as shown in Fig. 6.1.

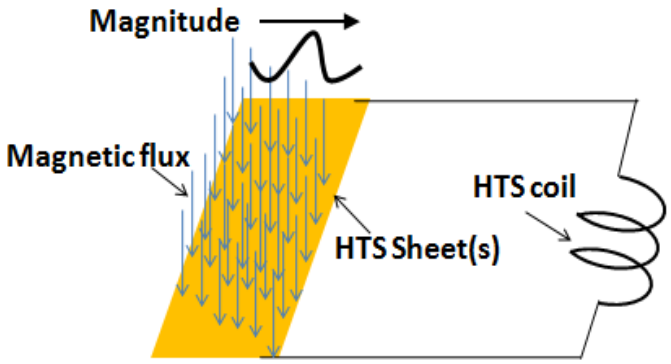

FIG. 6.1. Schematic drawing of travelling wave flux pumps. Magnetic field which is varying with time and in space is applied to an HTS sheet, resulting in the current increase in the HTS load connected to the sheet.

The flux pumping effect can be equated to a DC voltage being induced across the HTS sheet by the applied travelling wave, as shown in Fig. 6.2. The key point of these

flux pumps is how the DC voltage across the load is induced by external AC magnetic fields, which has also been confusing for many years.

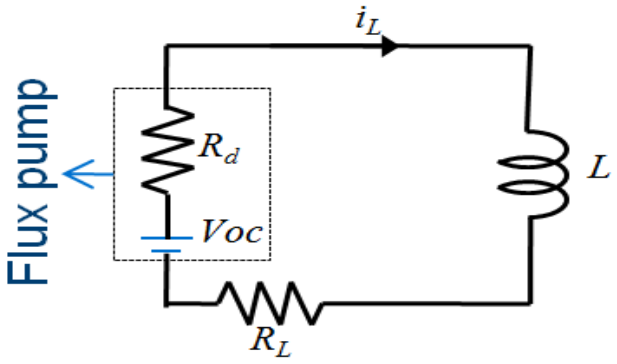

FIG. 6.2. Equivalent circuit of travelling wave flux pump. Where V_{OC} is the induced DC open circuit voltage, R_d is the internal resistance, R_L is the load resistance and L is the load inductance [62].

The DC transformer which predates the flux pumps described by Van Klundert [50, 51] et al appears in Gieaver [105] who pointed out that flux motion can be used to induce a DC voltage in a superconductor and described a rectifier based on a superconducting switch. These explanations, however, all rely on generating a moving normal spot or partially breaking superconductivity in low T_c superconductors. For high T_c superconductors such as YBCO the upper critical field is so high that it is impossible to generate normal spot in existing travelling wave HTS flux pumps [62]. In this Chapter, the author will reveal that varying resistivity of type II superconductors due to flux flow is the origin of the DC voltage and therefore flux pumping. The resistivity is influenced by current density in the superconductor, flux density experienced by the superconductor, and field rate of change. The proposed principle can well explain not only travelling wave flux pumps but also all other existing HTS flux pumps for coils.

6.2 Explanation of open circuit DC voltage in travelling wave flux pumps

6.2.1 Circuit model [106]

Fig. 6.3 shows a schematic of travelling wave flux pumps, which comprise a superconducting loop (loops) connecting to a superconducting load which we want to magnetize. The superconducting loop is formed either by one HTS sheet or several HTS tapes in parallel. The superconducting loop is subjected to magnetic fields which vary in time and space, these induce a voltage across the branch which is connected to the load, as shown in Fig. 6.3(a).

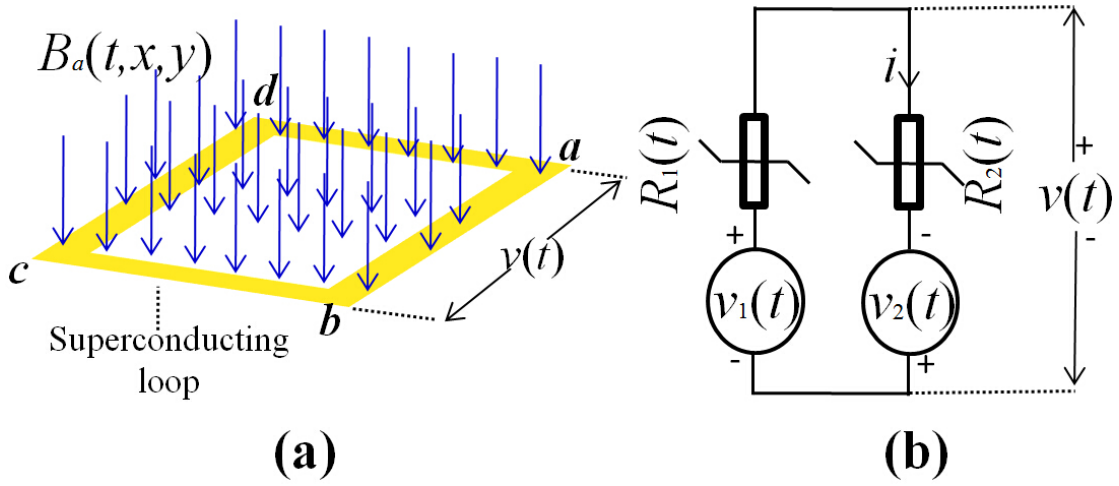

FIG. 6.3. Schematic drawing of open circuit voltage of travelling wave flux pumps. (a) Magnetic field varying in time and space is applied to a superconducting loop, part of which will be connected to a superconducting load. (b) Circuit analogy of travelling wave flux pump, where $v_1(t)$ and $v_2(t)$ represent the induced EMF forces in each branch, and $R_1(t)$ and $R_2(t)$ represent the resistance of each of the branches.

If the open circuit voltage $v(t)$ has a DC component V_{DC}, it will generate an increasing DC current in an inductive load. Therefore, the DC component is substantial in flux pumping. If the perimeter of the loop is considerably larger than the width of branches, and the resistance of this loop along its length is considerably larger than its inductance, Fig. 6.3(a) can be described by Fig. 6.3(b) as a circuit model, where the right branch of the circuit represent the branch *ab* in Fig. 6.3(a), the left branch in the circuit represents branch *adcb* in Fig. 6.3(a), $v_1(t)$ and $v_2(t)$ represent the induced EMF forces in each branches, and $R_1(t)$ and $R_2(t)$ represent resistance of the branches accordingly.

According to Faraday's Law:

$$v_1(t)+v_2(t)=\int_{adcb}\vec{E}\cdot d\vec{l}+\int_{ba}\vec{E}\cdot d\vec{l}=\oint_{l}\vec{E}\cdot d\vec{l}=-\int_{S}\frac{d\vec{B}}{dt}\cdot \mathbf{n}ds=-d\Phi/dt \qquad (6.1)$$

Where l is the perimeter of the loop, S is the area of the loop, B is the applied field, and Φ is the total flux that links the loop.

The open circuit voltage $v(t)$ across the branch is :

$$v(t)=iR_2(t)-v_2(t)=\frac{v_1(t)+v_2(t)}{R_1(t)+R_2(t)}R_2(t)-v_2(t) \qquad (6.2)$$

The DC component in $v(t)$ is:

$$V_{DC}=\frac{1}{T}\int_0^T v(t)dt=\frac{1}{T}\int_0^T\frac{-d\Phi/dt}{R_1(t)+R_2(t)}R_2(t)dt \qquad (6.3)$$

Where T is the period of the applied field in the area of the loop. Here we should consider $\int_0^T v_2(t)dt=0$ (Otherwise an AC magnetic field would induce a DC electric field, which is against Faraday's Law). It should be noticed that the same conclusion can be drawn by analyzing the left branch in Fig. 6.3(b). **Flux pumping is achieved if V_{DC} is non-zero**.

In Eq. 6.3, if $R_2(t)/(R_1(t)+R_2(t))$ is constant, then we can get:

$$V_{DC} = \frac{1}{T}\frac{R_2(t)}{R_1(t)+R_2(t)}\int_0^T -d\Phi / dtdt = 0 \qquad (6.4)$$

However, if $R_2(t)/(R_1(t)+R_2(t))$ is not constant during Φ increasing and decreasing process, Eq. 6.3may be non-zero. For simplicity, we assume that $R_2(t)/(R_1(t)+R_2(t))$ is constant during Φ increasing or Φ decreasing, and define $p_{dec}=R_2(t)/(R_1(t)+R_2(t))$ for Φ decreasing, and $p_{inc}=R_2(t)/(R_1(t)+R_2(t))$ for Φ increasing, then we can get:

$$V_{DC} = \frac{1}{T}(p_{dec}\int_0^{t_1} -d\Phi / dtdt + p_{inc}\int_{t_1}^T -d\Phi / dtdt) = \frac{1}{T}(p_{dec} - p_{inc})\Delta\Phi \qquad (6.5)$$

Where $t=t_1$ is the time flux is minimum, $t=0$ is the time flux is maximum, and $\Delta\Phi$ is the peak-peak value of Φ. According to Eq. 6.5, if the ratio of $R_1(t)$ and $R_2(t)$ changes in the flux increasing process and flux decreasing process, a DC component in the open circuit voltage will occur. The physics of p_{dec} and p_{inc} can be understood as follow: p_{inc} describes the proportion of flux that flows into the loop via branch *ab* in Fig. 6.3(a); p_{dec} describes the proportion of flux that flows out of the loop via the same branch. Since the net flux variation in the loop is zero during each cycle, if $p_{inc}\neq p_{dec}$, it means a net flux flows across branch *ab*. This net flux flow induces a DC voltage. This analysis also applies to branch *adcb* in Fig. 6.3(a).

For a superconducting loop which has a large inductance, the situation is slightly different. In this case,$v_1(t)$ and $v_2(t)$in the above equations now represent the co-function of EMF forces and induced inductive voltages due to current variation in the loop. Due to the fact that the circulating current in the loop is periodical, the integration of inductive voltage over T is zero. In fact, the inductance only influences the relative phase between the circulating current and the flux linking the loop. It will not change the substance that the variation of resistance in branches generates a DC component in the open circuit voltage.

For practical applications, we may want V_{DC} as large as possible. Various ways can be used to increase the value. By changing the value of $R_1(t)$ and $R_2(t)$, p_{dec}-p_{inc} varies in the region of (-1,1). For example, if $R_2(t)$ is much larger than $R_1(t)$ when Φ is decreasing and $R_2(t)$ is much smaller than $R_1(t)$ when Φ is increasing, then p_{dec}-$p_{inc}\approx$-1. By increasing field frequency, 1/T can be increased. By increasing field magnitude or area, $\Delta\Phi$ can be increased.

6.2.2 Influential factors on branch resistances

For a type-II superconductor, its resistivity is variable against current density, field intensity and field rate of change.

Firstly, the branch resistance depends on current density and applied field intensity, as described in *E*-*J* power law [26] under Kim's Model [20]:

$$R=\int_L \rho s dL=\int_L E_0 J^{n-1}/(\frac{J_{c0}}{1+B/B_0})^n s dL \qquad (6.6)$$

Where ρ is the resistivity, s is the cross section of the branch, and L is the length of the branch.

Secondly, the change in applied field will generate a loss, which can be considered as an equivalent AC loss resistance [107] or dynamic resistance [67, 92-94]:

$$R_{dyn}=\frac{2afL}{I_c}(B_a\text{-}B_{a,th}) \qquad (6.7)$$

Where a is the width of the superconductor, L is the length of superconductor that subjected to magnetic field, f is the frequency of applied field, B_a is the magnitude of applied field, I_c is the critical current of the superconductor, and $B_{a,th}$ is threshold field.

Last but not least, crossed-magnetic-field effect [108] and flux cutting effect [109] may also contribute to the variation of resistance, and thus contributes to pumping.

For a type II superconductor, if the geometries of the branches are the same and they are in a homogeneous AC magnetic field, $R_2(t)/(R_1(t)+R_2(t))$ is always constant, so no DC voltage can be generated. However, if the geometries are different, e.g. the branches have different current capacities, a DC voltage may occur even if the loop is in homogeneous field.

6.2.3 Explanation of travelling wave flux pumps

Several existing travelling wave flux pumps can be considered as the realization of Eq. 6.5 in the previous section, since in these flux pumps, an inhomogeneous AC magnetic field travels across the superconducting branches. This is explained as follows: When a travelling wave passes across the superconductor the two branches see different portions of the wave at the same instant. Two things result from this: in the first the flux density seen by each branch is different and in the second the rate of change of flux density is also different.

Flux pumping due to field dependence of branch resistances

Fig. 6.4(a) shows a symmetrical triangular magnetic wave travelling across a superconducting loop. The loop is formed from two branches with same geometry and which are infinitely long into the page.

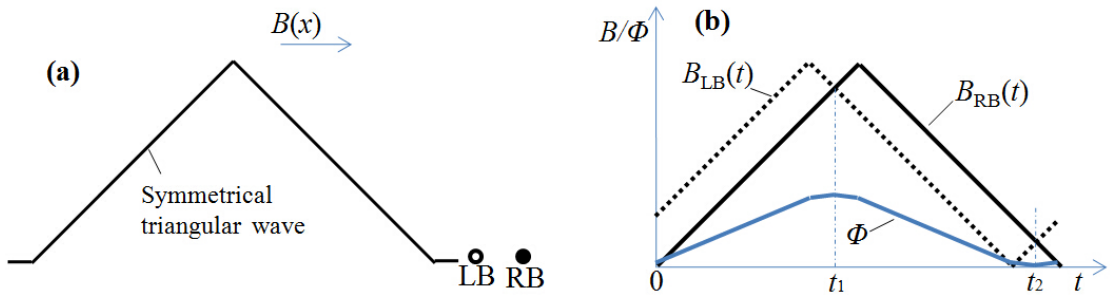

FIG. 6.4. Schematic drawing of a superconducting loop experiencing a symmetrical triangular travelling magnetic wave. (a) travelling magnetic field is proceeding towards a superconducting loop, which is formed by two branches infinitely long into the paper. LB denotes left branch, and

RB denotes right branch. (b) flux density experienced by the two branches against time, and total flux applied to the loop.

In Fig. 6.4(b), the two branches both experience a symmetrical triangular wave field and the phase difference is due to the different physical positions of each branch. During the time t=0 to t=t_1, the total flux in the loop is *increasing*, and the left branch is seeing a *higher* flux density than the right branch. During the time t=t_1 to t=t_2, the total flux in the loop is *decreasing*, and the left branch is seeing a *lower* flux density than the right branch. As is shown in Eq. 6.6 the branch resistances are dependent on the applied field. Thus resistance of the left branch is larger than that of the right branch in the flux increasing process, and is smaller during flux decreasing process. Therefore Eq. 6.5 predicts that a DC voltage will be induced.

Flux pumping due to field rate of change dependence of branch resistances

Fig. 6.5 shows the branches experiencing a narrow rectangular wave, in which the distance between the rise edge and the falling edge is shorter than the distance between the branches.

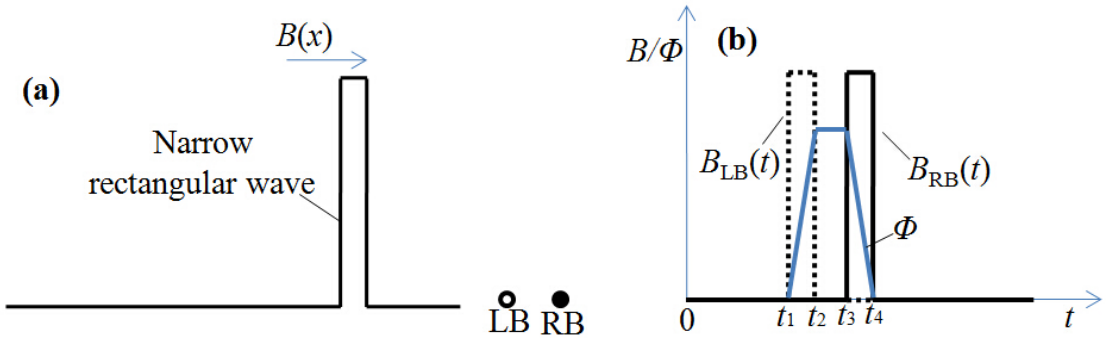

FIG. 6.5. Schematic drawing of a superconducting loop experiencing a narrow rectangular travelling magnetic wave. (a) travelling magnetic field is proceeding towards a superconducting loop, which is formed by two branches infinitely long into the paper. LB denotes left branch, and RB denotes right branch. (b) flux density experienced by the two branches against time, and total flux applied to the loop.

During time $t=t_1$ and $t=t_2$ the total flux in the loop increases, and the left branch experiences a fast change in field, which generates a loss (which can be considered as a dynamic resistance since the field in left branch changes much faster than the current in the loop, otherwise it can be considered as an AC loss resistance). During time $t=t_3$ and $t=t_4$ the total flux in the loop drops, and the right branch experiences a fast change in field, which generates a loss. So the ratio of resistances in the branches changes during flux rising and falling, thus resulting in a DC component in the open circuit voltage.

6.3 Experimental validation

A linear travelling wave based flux pump was built by Matsuda and Fu, which is shown in Fig. 6.6(a) [81].

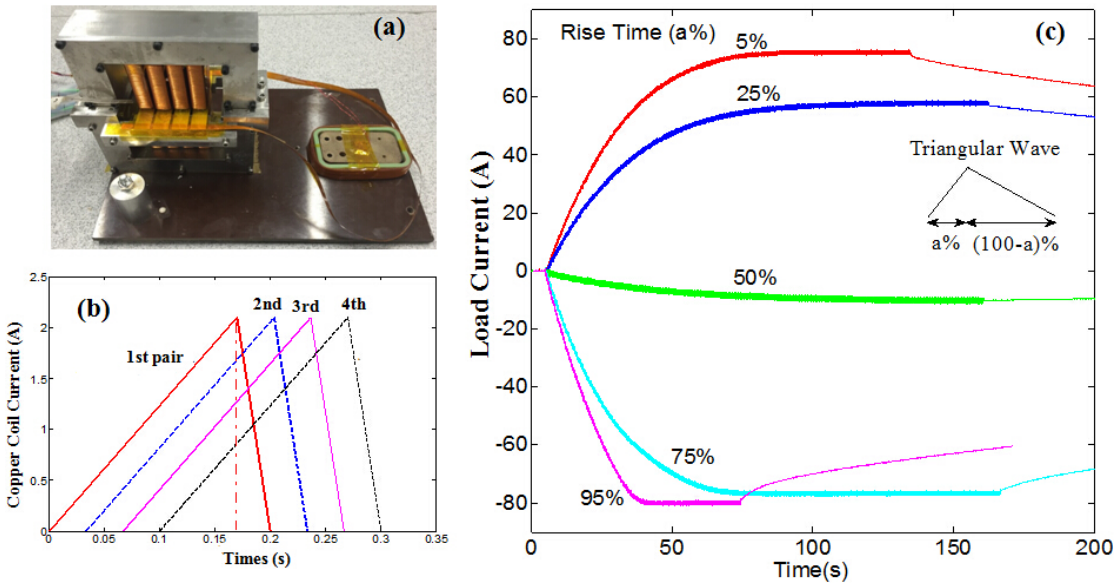

FIG. 6.6. Linear HTS flux pump device and flux pumping result. (a) The picture of the flux pump, which has 4 pole pairs that can generate a travelling magnetic wave. (b) The waveform of current in each pole pair. (c) The load current under different waveforms. **The flux pump was developed by Matsuda and Lin, and the results are also from their experiment**.

Four pairs of copper poles are used to generate travelling waves of various shapes. Four parallel placed CC tapes experience the travelling magnetic wave which is orientated perpendicular to their faces. The tapes are connected to a coil constructed from CC. The set up can be considered as two separate loops working in parallel. A triangular magnetic wave with different duty ratios (i.e. the ratio of the rise time to the period was varied) was applied and the results are shown in Fig. 6.6(c). The current induced in the coil rises exponentially which corresponds to it being induced by a DC voltage with an internal resistance. The results presented here show that different duty ratios end up with different load currents. The difference between field rise time and fall time influences not only the final load current magnitude but also the polarity and the rate of rise.

The effect of field dependence of resistance

For a symmetrical waveform, which is similar to the description in Fig. 6.4, a very small amount of current is pumped into the load with a low speed, which indicates a low DC voltage is induced. This result shows that the field dependence of the critical current density (branch resistance) is not the key influential factor in the experiment. This may be because the circulating current induced in the loops is small compared to branches critical current, so that even though different branches experience different magnetic fields, the difference between branches resistances is negligibly small.

The effect of field rate of change dependence of resistance

When the duty ratio is changed then the rate of change of field is markedly different for the two branches. The current rises more rapidly which indicates the DC voltage is higher. This is similar to the process described in Fig. 6.5, where the loss caused by the rate of change of the field has become the dominant factor in the experiment.

A similar result is obtained for moving magnet based flux pumps [62-67], if more than one piece of tape forms the superconducting loop, it is very similar to the description in Fig. 6.3.The published results [62, 65, 67] show that the pumping speed

is nearly proportional to rotating frequency and the load current polarity is related to rotating direction, which proves the assumption. If only a single piece of tape experiences the moving magnetic field, it may also be considered as a loop as the induced currents will circulate within the tape [105]. In this case there is an additional factor as the size of the two branches is not fixed.

6.4 Discussion

Although this explanation has concentrated on travelling waves, it has been shown in Chapter 4 and Chapter 5 that it is not necessary for a travelling wave to be present for a DC voltage as predicted by Eq. 6.5 to be induced. Substantially, travelling wave flux pumps share the same mechanism as the flux pump proposed in Chapter 4. In these flux pumps, travelling magnetic field plays two roles simultaneously: magnetic induction and development of branches resistances. Because the magnetic induction and development of branches resistances are bonded together, it is difficult of achieve an optimized operation of these flux pumps. In contrast, in the flux pump proposed in Chapter 4, a transformer is used to induce EMF in the loop, and the resistance is generated independently of the magnetic induction. The separation of these two processes makes it possible for flexible control of the flux pump, and to achieve minimized losses.

The flux pump proposed in Chapter 5 is also a theoretical breakthrough. Previous HTS flux pumps all rely on inhomogeneous magnetic field to achieve flux pumping, whereas the results in Chapter 5 shows that homogeneous wave could also work (if we consider the transformer as a source of uniform field) as long as Eq. 6.5 is satisfied.

6.5 Conclusion

In this chapter, the author has revealed variation in the resistivity of type II superconductors is the origin of the DC component of the open circuit voltage of travelling wave flux pumps. Because the resistivity of type II superconductors depends on the field magnitude, field rate of change, and current density, when magnetic fields with different magnitudes and different changing rates in space are applied to a superconducting loop, there is different and changing resistivity around the loop. This results in a DC open circuit voltage and is the origin of flux pumping in these devices. In a type I superconducting flux pump, a normal spot is used to transport flux into a superconducting loop, whereas in a type II or travelling wave type flux pump the normal spot is not necessary. The variable resistivity property is particularly evident in High Temperature Superconductors making them ideal candidates for this type of pump.

The work in this chapter make travelling wave flux pumps on longer mysterious.

Chapter 7
Voltage-Ampere Characteristics of YBCO Coated Conductor under Inhomogeneous Oscillating Magnetic Field

7.1 Introduction

The previous chapter explained the origin of DC component in the open circuit voltage of travelling wave flux pumps. This chapter will extend the research to the Voltage-Ampere (V-I) characteristics of coated conductor under external travelling magnetic fields.

It is well known that type II superconductors carrying a direct current present a resistance when they are under a perpendicular oscillating magnetic field [92-95, 110-116]. Theoretical analysis [94, 95, 110, 112] and experimental results [110-114] have shown that this resistance is due to flux flow caused by the interaction between the transport current and the applied field, and it is defined as dynamic resistance. The dynamic resistance value is proportional to the applied field magnitude and frequency if the superconductor in a homogeneous field, and it is nearly independent of transport current if the field magnitude is high [94]. Hoffmann and coworkers [62] discovered flux pumping effect when a piece of superconducting stator connecting to a superconducting load was subjected to inhomogeneous magnetic fields orthogonal to the tape surface generated by rotating permanent magnets. Researchers from VUW [67] pointed out that dynamic resistance is the main limiting factor of saturation current in the flux pump. Concerning the open circuit voltage, they proposed a geometrical explanation considering screening current [75]. All these existing researches focus on the flux pumping effect, where the superconducting stator generates DC power. It will

be interesting and beneficial to extend the research to the V-I characteristics of YBCO Coated Conductor (CC) under rotating permanent magnets, in which the CC could either absorb or generate DC power.

7.2 Experimental system

The experimental system is shown in Fig. 7.1, which is similar to rotating magnets flux pumps [62-66]. Eight Neodymium 52 permanent magnets with a diameter of 20mm and a thickness of 10mm are uniformly mounted on a round copper disc. The outer diameter of the disc is about 81mm. All magnets were mounted with their north poles facing outward. The disc was fixed on a shaft, which was driven by a motor controlled by a three-phase inverter. A piece of *Superpower* 12mm width copper stabilized YBCO Coated Conductor (CC) tape was put beneath the disc. The tape was submerged in Liquid Nitrogen (LN2) @77K.When the disc rotates, each magnet passes across the tape. The minimum gap between each magnet and the tape surface was 2mm, when the tape surface was facing a magnet's north pole. In this case, the maximum flux density was about 0.2T. The rotating speed of the shaft can be adjusted in the range of 0-15Hz, so the field frequency experienced by the CC tape was adjustable from 0 to 120Hz.

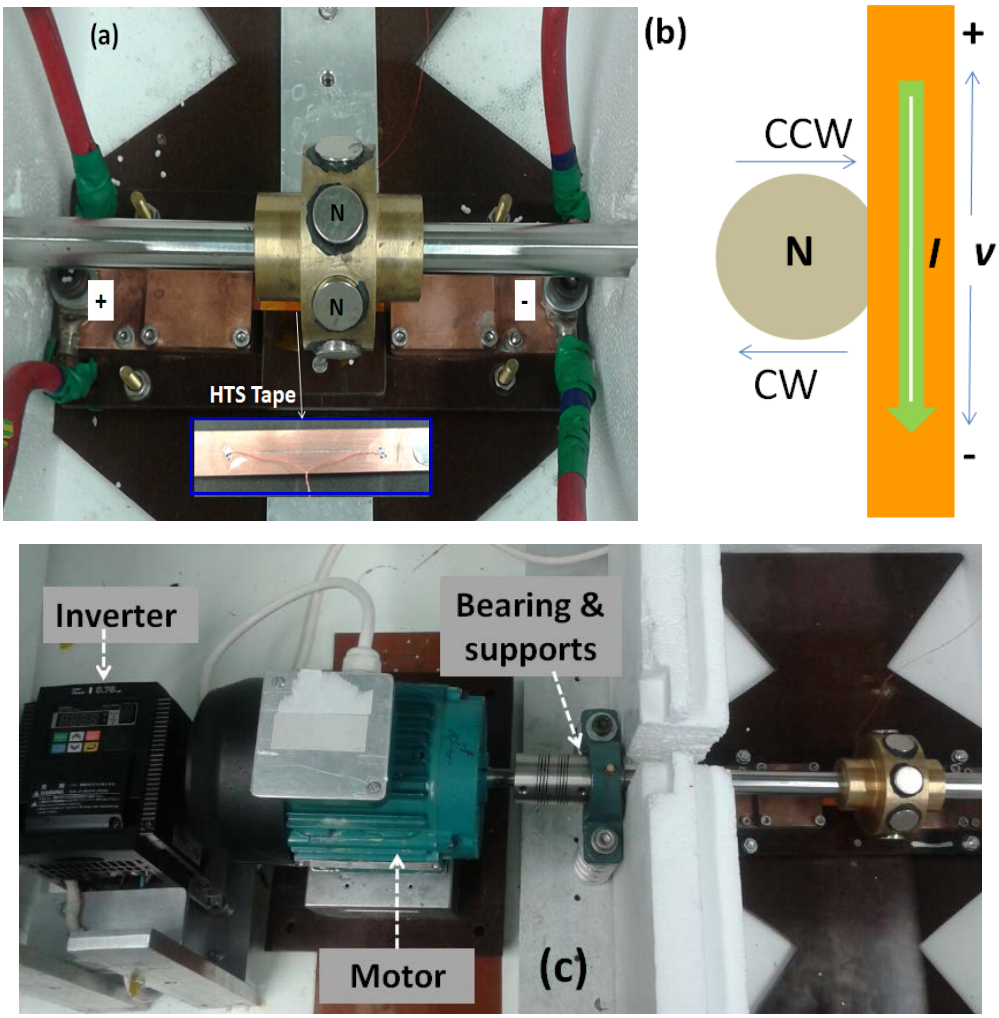

FIG. 7.1. Experimental system to investigate the V-I characteristics of CC under inhomogeneous magnetic field. (a) picture of the experimental system, where permanent magnets spin across a DC carrying YBCO CC. (b) reference direction of voltage, current, and magnets' movement. It is the bottom view of Fig. 1(a) so that the north pole of a magnet is seen, and the reference direction of voltage is marked in Fig. 1(a). CW refers to clockwise, and CCW refers to counter clockwise. (c) picture of the driving system.

A main difference between this system and a rotating magnet flux pump is that the tape (or stator wire in flux pumps) is connected to a constant DC power supply via a pair of current leads rather than to an inductive load. This set up allows the author to investigate the V-I characteristics in a wide current range. A pair of voltage

measurement leads was soldered to the centre of the stabilizer layer of the tape, as shown in Fig 7.1(a). The distance between the two soldering points was 5cm. The voltage leads were closely twisted together to minimize noises and the AC signal generated by the rotating magnets. In between the voltage leads, parallel to the tape, a 4cm long cut was made in the centre of the tape, which broke the superconducting layer. The voltage was sampled by an NI-6221 DAQ card with a sampling frequency of 2.4 kHz. The sampling frequency was chosen considering the highest field frequency to be 120Hz. The reference direction of voltage, current, and magnets' rotation is defined in Fig. 7.1(b), where CCW denotes counter-clockwise and CW denotes clockwise.

7.3 Results and analysis

The static V-I characteristics of the tape were measured both before and after the cut. The V-I curve was measured with two different relative positions between magnets and the tape, i.e. the tape under the surface of a magnet or the tape under the gap between two magnets. As shown in Fig. 7.2, the critical current of the tape under a magnet is much lower than that under the gap. This is because a strong field dependence of critical current density of YBCO. It can also be seen from Fig. 7.2 that the current capacity of the tape reduced slightly after cut.

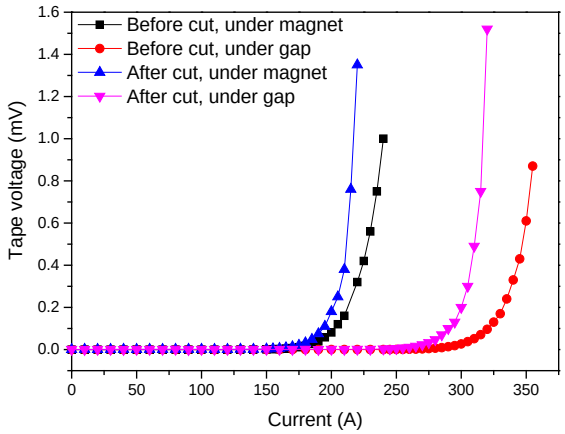

FIG. 7.2. V-I curve of the CC tape before and after the cut without magnets rotating.

In the rotating test, the author firstly adjust the motor at a determined speed, then ramp up the transport current from zero to 296A at an average rate of about 5A/s. Fig. 7.3 shows the V-I curves of the cut tape under rotating magnets with different speeds and directions. The data have been low-pass filtered by averaging samples in each 0.5s, so the AC component in voltage and current was eliminated. As can be seen from Fig. 7.3, when the transport current is less than 200A, all V-I curves are nearly linear. Under the same field frequency, both curves of opposite rotating directions tend to have the same slope although the intercepts differ from each other. When the transport current exceeds 200A, all curves become nonlinear. The difference of any two curves under the same field frequency begins to decrease, and in the end the two curves nearly overlap with each other.

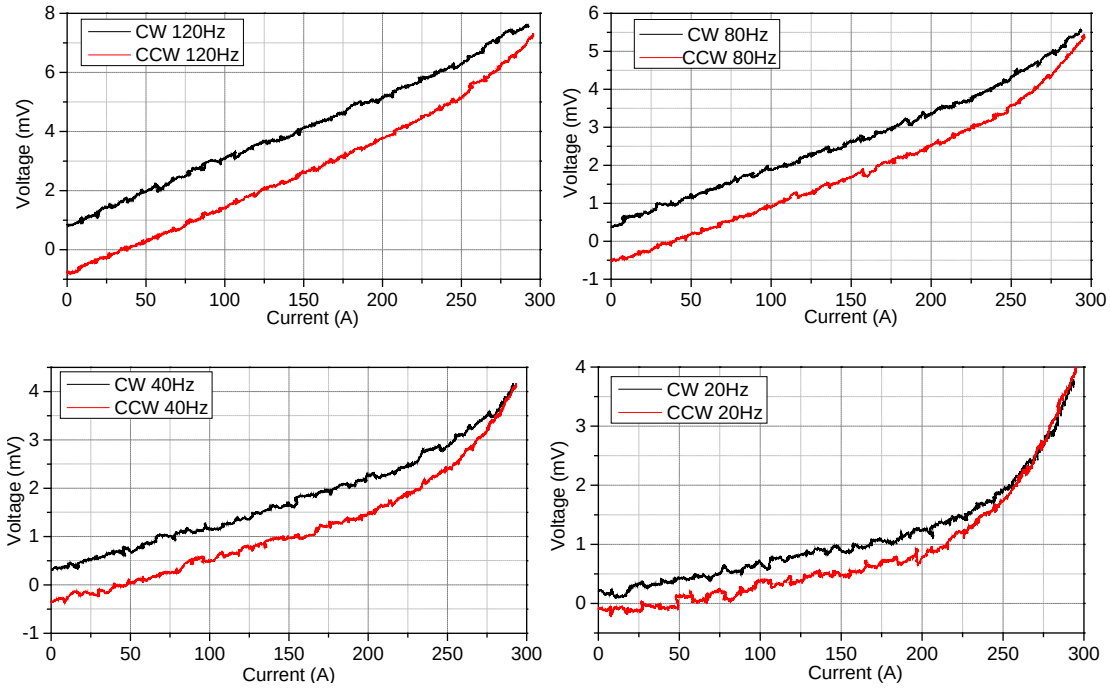

FIG. 7.3. V-I curves of the cut CC tape under magnets of different rotating frequencies and directions.

The author re-plotted the V-I curves under 200A with a linear fitting, as shown in Fig. 7.4 and Fig. 7.5. It can be seen from Fig. 7.4 that for CCW rotation, all curves start with

a negative open circuit voltage, and they cross together at V=0, I=35A. From I=0A to I=35A, DC power consumed by the CC is negative, i.e. the CC actually works as a flux pump, although it is connected to a power supply rather than an inductive load. The result is consistent with the results in Ref. 67. I=35A is actually the largest achievable current if the CC is connected to a superconducting load rather than a power supply. It should also be noticed that at the point I=35A, no transport loss is generated although the superconductor is subjected to an oscillating field orthogonal to its surface. In comparison, Fig. 7.5 shows the V-I curves under CW rotating magnets. All curves start with a positive open circuit voltage, and the voltage increases linearly with current. The voltage is always positive, which indicates that the CC consumes dc power all the time. From Fig. 7.4 and Fig. 7.5, it is clear that the transport loss is dependent on the magnets' rotating direction, with a certain transport current. This is distinct from dynamic resistance model under homogeneous AC field. The result may be indicative in designing superconducting motors [117], especially in reducing persistent current decay in rotor stack tapes [118] or coils [47-49] which are under ripple travelling waves.

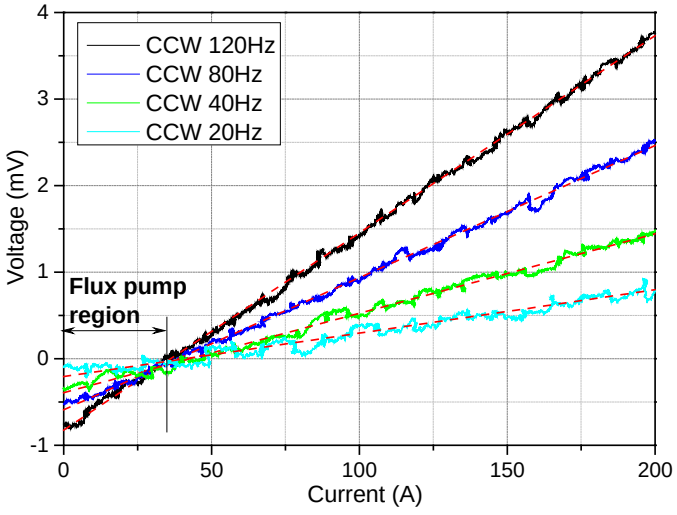

FIG. 7.4.V-I curves of counter clockwise rotating magnets together with linear fitting curves. For each field frequency, all curves start with a negative open circuit voltage. The curves cross

together at V=0, I=35A. From I=0 to I=35A, it is actually working as a flux pump. I=35A is therefore the maximum current the device can output in a flux pump.

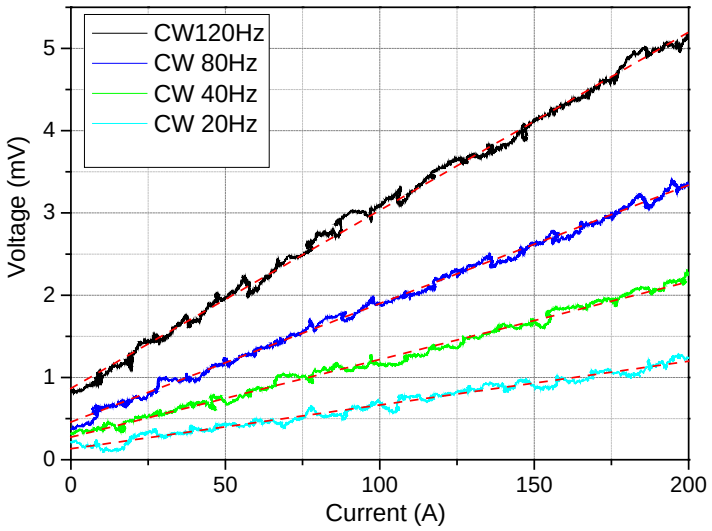

FIG. 7.5. The results of clockwise rotating together with linear fitting curves. For each field frequency, all curves start with a positive open circuit voltage. For each curve, the voltage increases linearly with the current.

From the intercept and slope of fitting curves in Fig. 7.4 and Fig. 7.5, we can get the open circuit voltage V_{oc} and equivalent resistance R_{eq} of each curve, which have been plotted in Fig. 7.6 and Fig. 7.7. Both of the open circuit voltage and the equivalent resistance are proportional to field frequency. The result extended the previous researches on flux pump [62-66] which only generates DC power. The result shows that flux pumping effect exists even though the CC is open circuited, it also indicates that the open circuit voltage exist all the time no matter whether the CC generates dc power or consumes dc power.

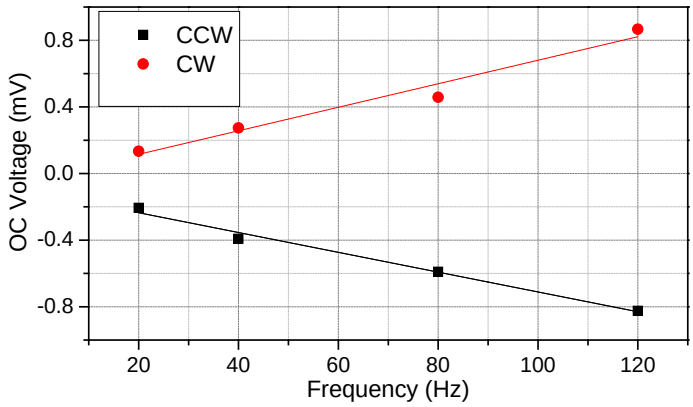

FIG. 7.6. Open circuit voltage of the YBCO CC tape under different field frequencies.

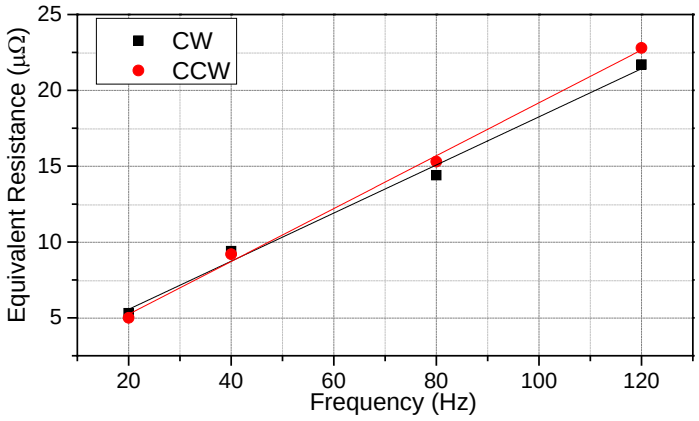

FIG. 7.7. Equivalent resistance of the YBCO tape under different field frequencies.

After the transport current exceeds 200A, two phenomena in the V-I curves in Fig. 7.3 should be noticed: the curve under lower frequency field tends to be more nonlinear although the absolute voltage is lower; the difference between the curves of CCW and CW rotating reduces faster with lower frequency.

In Ref. 75, the open circuit voltage of a flux pump was explained as: the screening current follows the position of the magnet; due to the geometry of the magnet and the CC width, the width of forward path and backward path of the screening current changes, thus resulting in a rectifying effect. In this experiment, however, the tape was cut, and therefore a barrier occurs in the middle of the tape, and the screening current

distribution is different from that described in Ref. 75. The screening current tends to more locally circulate either side of the cut, rather than entirely circulate a loop round the cut. Therefore, the current density inside the tape will cannot be inversely proportional to the angle of the magnet which has been described in Ref. 75.

The general explanation for the open circuit DC voltage of type II superconducting films under travelling magnetic field has been analyzed in previous Chapter. The open circuit DC voltage can be expressed as:

$$V_{DC} = \frac{1}{T}\int_0^T \frac{-d\Phi / dt}{R_1(t) + R_2(t)} R_2(t)dt \qquad (7.1)$$

Where T is the ac period of applied travelling field, Φ is the flux into the superconducting film due to external field excitation, and $R_1(t)$ and $R_2(t)$ represent the time varying resistances of the two edges of the film. The origin of the resistances is flux motion. The physics of Eq. 7.1 has been explained as if more flux enters the film from one edge than that leaves the same edge, a DC open circuit voltage will appear.

For a CC transporting a current I, when it is under a perpendicular ac field, two kinds of flux motion occur [93, 113]. When $I \ll I_c$, the pinning energy [119] is large so the flux motion is mainly caused by the interaction between the ac field and transport current I, i.e. dynamic resistance; whereas when I approaches or exceeds I_c, the pinning energy becomes low, the superconductor will be in flux flow region. Therefore, the author proposes the following model to explain the result (Fig. 7.8).

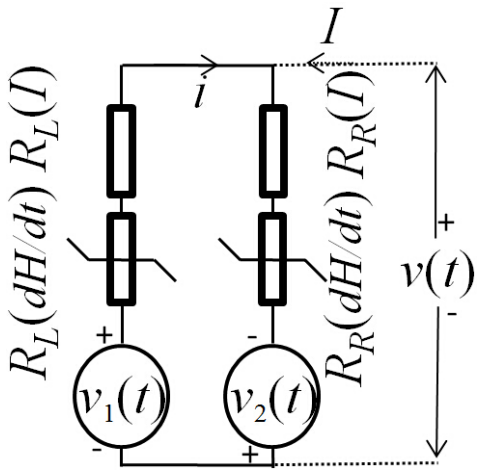

FIG. 7.8. Equivalent circuit model for the CC transporting a DC under rotating magnets. Where *i* represents the screening current circulating the cut and *I* represents the transport current, $v_1(t)$ and $v_2(t)$ represent EMFs. Each edge of the tape can be considered as two resistances in series, $R_L(dH/dt)$ and $R_R(dH/dt)$ represent equivalent resistances of flux flow caused by the interaction between the local AC field and *i*, $R_L(I)$and $R_R(I)$can be considered as flux motion caused by de-pinning.

Each edge of the CC can be considered as the sum of two resistances:

$$R_{edge}(t) = R_{edge}(dH / dt) + R_{edge}(I) \qquad (7.2)$$

Where $R_{edge}(t)$ represents the total resistance of either edge, and $R_{edge}(dH/dt)$ is the dynamic resistance of each edge which is caused by the interaction between the changing field at each edge and the global screening current *I* circulating the cut, and $R_{edge}(I)$ is caused by the de-pinning effect. When the transport current *I* is smaller than 200A, the pinning energy is large, so $R_{edge}(I)$ is negligibly small compared with $R_{edge}(dH/dt)$. In this case, the open circuit voltage is the same as we reported in Chapter 6. Most flux will enter the CC from one edge and leaves at the other, so the open circuit voltage magnitude is proportional to field frequency and its polarity is determined by field travelling direction. When the transport current *I* exceeds 200A, $R_{edge}(I)$ gradually increases and become the dominant resistance. In this case, when a magnet is

approaching the CC, flux flows into the CC from both edges; when a magnet is leaving the CC, flux flows out of the CC from both edges. The net flux flow across each edge reduces with the increase of the de-pinning flux flow. For a lower frequency field, the values of $R_{edge}(dH/dt)$ is smaller, so the effect of de-pinning flux flow is more significant. Therefore, the difference between the two V-I curves under opposite rotating directions decreases faster at lower field frequencies.

The equivalent resistance is approximate to the parallel of edge resistances. When the transport current is low, the equivalent resistance is mainly contributed by dynamic resistance, which is proportional to field frequency, and is independent of transport current. In this case, the V-I curves tend to be linear. When the transport current is high, de-pinning flux flow dominates the equivalent resistance and the curves become nonlinear. Similar results can be found in Ref. 111 and Ref. 113, where the superconductor is more nonlinear due to lower dynamic resistances.

7.4 Conclusion

The author conducted experiments on the *V-I* curve of YBCO coated conductor under permanent magnets with different rotating speeds and directions. The results are distinct from the V-I curve of a superconductor under homogeneous AC field. When the transport current is under the critical current, all curves can be well fitted by an open circuit voltage and a constant equivalent resistance, both of which are proportional to field frequency. Yet the polarities of the open circuit voltage are opposite with opposite rotations. All curves become nonlinear after the transport current exceeds the critical value, and the difference between the two curves under opposite rotations reduces with the current increase. The curves under lower frequency field tend to be more nonlinear, and the difference between the two curves under opposite rotation decreases faster. The author has proposed a circuit model that is a combination of a flux pump model together with flux motion characteristics in dc carrying superconductor under an AC

field. Two factors contribute to the flux flow in the CC: when transport current is low, the pinning energy is high, and the flux flow is due to the interaction between the screening current and the local ac field, which is dependent on field rotating direction; when transport current is high, flux flow is caused by de-pinning, which is independent of field rotating direction.

The result may help researchers further understand the magnetization behaviour of coated conductors under travelling magnetic field, and it may also be beneficial to designing superconducting motors to minimize current decay in the rotor.

Chapter 8
Conclusion and Future Work

8.1 Conclusion

Flux pumping is a promising technology enabling HTS magnets to generate extremely high magnetic fields with insignificant loss. This thesis presented a systematic study on flux pumping for HTS coils. It provided a brand new perspective to comprehensively understand flux pumping behaviour in type II superconductors.

In Chapter 3, the author proposed the idea of using an AC magnetic field to induce a dynamic resistance in a piece of high T_c superconductor as a persistent current switch. The well-known effect that flux flow can be triggered when a DC transporting type-II superconductor is subjected to a perpendicular AC field was used. The idea was experimentally verified by using a DC current supply and an external AC field to charge a closed HTS magnet. The dynamic voltage response of the switch to applied AC field was tested, and the result showed that the response was nearly instantaneous, indicating the switch can operate at much higher speed than existing persistent current switches.

Furthering the study of the persistent current switch in Chapter 3, the author originally proposed a novel HTS flux pump in Chapter 4. In the flux pump, a low frequency AC transport current was induced in the bridge superconductor, and an AC magnetic field was intermittently applied perpendicularly to the bridge when the transport alternating current is in the same polarity. This results in a unidirectional flux flow across the bridge superconductor, pumping up the load current. The flux pump can also be considered as a rectifier in which bridge dynamic resistance generated by AC field rectifies the induced alternating current in the bridge. The results have clearly shown that flux pumping can be achieved without driving high T_c superconductors

normal, which is a significant theoretical breakthrough. The flux pump is also able to make quantitative flux injection. In the future it is expected to achieve micro-Wb flux injection, which can be used to generate extremely stable magnetic field in HTS magnets. The author experimentally examined the influential factors of the flux pump, and developed a feedback control system. Using feedback control, the load current can be stabilized at a preset level with minimized loss, and a constant voltage output mode can also be realized.

In Chapter 5, the author presented the principle and experimental results for a self-switching HTS flux pump. The flux pump further simplified the work in Chapter 4. Instead of controlling the bridge superconductor by an AC field, the self-switching flux pump was achieved by driving bridge superconductor into flux flow region using an induced asymmetrical transport current. A transformer generates a high secondary current with its positive peak value much larger than the negative peak value. During each cycle, around the positive peak of the secondary current, the bridge superconductor is driven into the flux flow region, during the rest of the cycle the bridge remains superconducting. Flux is then accumulated in the load. The load current can be easily charged to the critical value. The work makes flux pumping for HTS CC coils much simpler than ever before.

In Chapter 6, a generalized explanation was given to understand the physics of all flux pumps involving type II superconductors. It is revealed that variation in the resistivity of type II superconductors is the origin of the DC component of the open circuit voltage of travelling wave flux pumps. Because the resistivity of type II superconductors depends on the field magnitude, field rate of change, and current density, when magnetic fields with different magnitudes and different changing rates in space are applied to a superconducting loop, there is different and differing resistivity around the loop. This results in a DC open circuit voltage and is the origin of flux pumping in these devices.

In Chapter 7, the author examined the *V-I* curve of YBCO coated conductor under inhomogeneous AC field. The results are distinct from the well-recognized dynamic resistance model in which the superconductor is under homogeneous AC field. When the transport current is low, the result follows the flux pump model proposed in Chapter 6, whereas when transport current approaches the critical value, flux pumping effect gradually disappears. A circuit model was proposed which is a combination of the proposed flux pump model together with flux motion characteristics in DC carrying superconductor under an AC field. The result may help researchers further understand the magnetization behaviour of coated conductors under travelling magnetic field.

In conclusion, this thesis established a framework in the area of flux pumping for HTS coils. It revealed the underlying physics of existing travelling wave flux pumps, which is an important theoretical contribution. Based on the thorough understanding of flux pumping mechanism, the author proposed two novel types of flux pumps. The new inventions make flux pumping much easier, more controllable, and much less energy consuming. These flux pumps may promote the future applications of HTS magnets. This thesis can be a guidebook for researchers and engineers in developing flux pumps.

8.2 Future work

The first issue is to scale up the two flux pumps proposed in this thesis. The aim is to achieve 2kA-20kA persistent current in closed HTS magnets. The work may have profound engineering influence. The National High Magnetic Field Lab (NHMFL) in Tallahassee, USA is now developing a 60T HTS magnet. Such a magnet needs a huge transport current, and higher the transport current is, smaller the magnet needs to be. However the huge transport current requires huge current leads, consuming massive energy, and generating tremendous loss. They have shown great interest in using the proposed flux pumps as a possible solution. However, to achieve such a goal, a lot of

seen and unseen technological problems have to be solved. Firstly, such a high current will generate huge forces between the superconductor and field magnet, so the mechanical stability is crucial. Secondly, huge transport current generates considerable loss on joints, so it is desirable to develop low loss joints. Thirdly, to fully penetrate the superconductor which has high current capacity, the field strength is demanding. These challenges are worthy of paying great attention.

The second issue is to achieve extremely precise flux injection. The aim is achieve micro-Wb or even nano-Wb level flux injection. This work will involve the careful design the flux pump, the superconducting circuit, and the sensing system. One obvious challenge is how to reduce magnetic coupling between the superconducting loops.

The third issue is to develop a superconducting inverter. In various applications it is desirable to deliver energy out of superconducting magnets and cryogenic environment, such as in SEMS and magnet quench protection. If a flux pump is considered as a rectifier, naturally we should think about operate it inversely, i.e., as an inverter.

References

[1] H. Kamerlingh-Onnes. *Comm. Leiden, Suppl.*, **34**, 1913.

[2] W. Meissner and R. Ochsenfeld, “Ein neuer Effekt bei Eintritt der Supraleitfähigkeit,” *Naturwissenschaften*, **21**, 787, 1933.

[3] "http://en.wikipedia.org/wiki/Superconductivity."

[4] J. G. Bednorz and K. A. Müller, “Possible high T_c superconductivity in the Ba−La−Cu−O system,” *Zeitschrift für Physik B Condensed Matter*, **64**, 189, 1986.

[5] W. Buckel and R. Kleiner. Superconductivity: Fundamentals and applications, 2nd edition, page 211, 2004.

[6] W. Buckel and R. Kleiner. Superconductivity: Fundamentals and applications, 2nd edition, page 234-235, 2004.

[7] D. Larbalestier, A. Gurevich, D. M. Feldmann, and A. Polyanskii, “High-T_c superconducting materials for electric power applications,” *Nature*, **414**, 368, 2001.

[8] L. D. Landau and D. t. Haar, “Collected papers of L. D. Landau,” 1st ed. Oxford: Pergamon,1965.

[9] C. P. Poole, H. A. Farach, and R. J. Creswick. Superconductivity. Page 340-341, 2007.

[10] J. Bardeen, L. N. Cooper, and J. R. Schrieffer, “Theory of superconductivity,” *Phys. Rev.*, **106**(1), 162, 1957.

[11] A. A. Abrikosov, “The magnetic properties of superconducting alloys,” *J. Phys. Chem. Sol.*, **2**(3), 199, 1957.

[12] C. P. Poole, H. A. Farach, and R. J. Creswick. Superconductivity. Page 346, 2007.

[13] K. Fossheim and A. Sudbø. Superconductivity: physics and applications. Page 200, 2004.

[14] C. P. Poole, Hand book of superconductivity. Page 554, 2000.

[15] B. M. Vlcek, *et al.* “Flux pinning in YBa2Cu3O7− δ single crystals: Neutron irradiation and annealing.” *Phys. Rev. B*, **46**(10), 6441, 1992.

[16] E. M. Chudnovsky, “Pinning by oxygen vacancies in high-T_c superconductors,” *Phys. Rev. Lett.*, **65**(24), 3060,1990.

[17] D. R. Nelson, and V. M. Vinokur, “Boson localization and pinning by correlated disorder in high-temperature superconductors,” *Phys. Rev. Lett.* **68**(15), 2398, 1992.

[18] C. P. Bean, “Magnetization of high-field superconductors,” *Rev. Mod. Phys.*, **36**, 31, 1964.

[19] Y. B. Kim, C. F. Hempstead, and A. R. Strnad, “Critical persistent currents in hard superconductors,” *Phys. Rev. Lett.*, **9**, 306, 1962.

[20] Y. B. Kim, C. F. Hempstead, and A. R. Strnad, “Magnetization and critical supercurrents,” *Phys. Rev.*, **129**, 528, 1963.

[21] P. W. Anderson and Y. B. Kim, "Hard Superconductivity: Theory of the motion of Abrikosov Flux Lines," *Rev. Mod. Phys.*, **36**, 39, 1964.

[22] P. W. Anderson, “Theory of flux creep in hard superconductors,” *Phys. Rev. Lett.*, **9**, 309, 1962.

[23] M. R. Beasley, R. Labusch, and W. W. Webb, “Flux creep in type-II superconductors,” *Phys. Rev.*, **181**, 682, 1969.

[24] A. P. Malozemoff, “Flux creep in high temperature superconductors,” *Physica C: Supercond.*, **185–189**, 264, 1991.

[25] Y. Yoshida, M. Uesaka, and K. Miya, “Magnetic field and force analysis of high T_c superconductor with flux flow and creep,” *IEEE Trans. Magn.*, **30**, 3503, 1994.

[26] A. Gladun, G. Fuchs, K. Fischer, D. Busch, R. Eujen, and J. Huedepohl, “Critical current densities and activation energy of BiPbSrCaCuO tapes,” *IEEE Trans. Appl. Supercond.*, **3**, 1390, 1993.

[27] W. J. Carr. AC loss and macroscopic theory of superconductors. 2nd edition, 2001.

[28] H. Wada, *et al*, “Prospect of high-field MRI,” *IEEE Trans. Appl. Supercond.*, **20**(3), 115, 2010.

[29] B. J. Parkinson, R. Slade, M. J. D. Mallett, and V. Chamritski, “Development of a Cryogen Free 1.5 T YBCO HTS Magnet for MRI,” *IEEE Trans. Appl. Supercond.*, **23**, 4400405, 2013.

[30] W. D. Markiewicz, J. R. Miller, J. Schwartz, “Perspective on a superconducting 30T/1.3 GHz NMR spectrometer magnet,” *IEEE Trans. Appl. Supercond.*, **16**(2), 1523, 2006.

[31] Y. Iwasa, *et al.*, “A high-resolution 1.3-GHz/54-mm LTS/HTS NMR magnet,” *IEEE Trans. Appl. Supercond.*, **25**(3), 4301205, 2015.

[32] S. Kusada, *et al.*, “The project overview of the HTS magnet for superconducting maglev,” *IEEE Trans. Appl. Supercond.*, **17**(2), 2111, 2007.

[33] F. Sass, *et al.*, “Application of 2G-tape for passive and controlled superconducting levitation,” *IEEE Trans. Appl. Supercond.*, **21**(3), 1511, 2011.

[34] K. Tasaki, *et al.*, “HTS magnet for maglev applications (1)—Coil characteristics,” *IEEE Trans. Appl. Supercond.*, **16**(2), 1100, 2006.

[35] Y. Iwasa, “HTS magnets: stability; protection; cryogenics; economics; current stability/protection activities at FBML,” *Cryogenics*, **43**(3-5), 303, 2003.

[36] “https://nationalmaglab.org/news-events/news/mini-magnet-packs-world-record-punch”

[37] “https://nationalmaglab.org/about/around-the-lab/what-the/current-lead”

[38] L. Siyuan, J. Xiaohua, C. Guolin, and C. Jiangbo, “Superconducting joint and persistent current switch for a 7-T animal MRI magnet,” *IEEE Trans. Appl. Supercond.*, **23**, 4400504, 2013.

[39] K. Nemoto, S. Saito, Y. Sanada, K. Sasaki, S. Miyake, and H. Hashiguchi, “Niobium-tin persistent-current switch for the superconducting magnet of Maglev,” *IEEE Trans. Appl. Supercond.*, **9**, 181, 1999.

[40] T. K. Ko, Y. S. Oh, and S. J. Lee, “Optimal design of the superconducting persistent current switch with respect to the heater currents and the operating currents,” *IEEE Trans. Appl. Supercond.*, **5**, 262, 1995.

[41] J. Liu, J. Cheng, F. Zhou, Q. Wang, K. Chang, X. Li, “Electrical properties of cold-pressing welded NbTi persistent joints,” *Cryogenics*, **58**, 62, 2013.

[42] G. D. Brittles, T. Mousavi, C. R. M. Grovenor, C. Aksoy, and S. C. Speller, “Persistent current joints between technological superconductors,” *Supercond. Sci. Technol.*, **28**(9), 093001, 2015.

[43] “http://www.superpower-inc.com/content/2g-hts-wire”

[44] Y. Kim, *et al.*, “YBCO and Bi2223 coils for high field LTS/HTS NMR magnets: HTS-HTS joint resistivity,” *IEEE Trans. Appl. Supercond.*, **23**(3), 6800704, 2013.

[45] Y. Park, M. Lee, H. Ann, Y. H. Choi, H. Lee, “A superconducting joint for GdBa2Cu3O7−δ-coated conductors,” *NPG Asia Materials*, **6**(5), e98, 2014.

[46] H. Shin, *et al.*, “The strain effect on critical current in YBCO coated conductors with different stabilizing layers.” *Supercond. Sci. Technol.*, **18**(12), S364, 2005.

[47] Y. Park, *et al.*, “Experimental analysis on initial current decay characteristics of persistent-mode HTS coil by external alternating magnetic field,” *IEEE Trans. Appl. Supercond.*, **25**(3), 3601204, 2015.

[48] Y. Park, et al., “Operational characteristics of HTS coils with flux diverters in semi persistent mode under alternating magnetic field,” *IEEE Trans. Appl. Supercond.*, **26**(4), 5204105, 2016.

[49] J. Geng, H. Zhang, C. Li, X. Zhang, B. Shen, and T. A. Coombs. “Angular dependence of direct current decay in a closed YBCO double-pancake coil under external AC magnetic field and reduction by magnetic shielding,” *Supercond. Sci. Technol.*, **30**(3), 035022, 2017.

[50] L. J. M. van de Klundert, and H. H. J. ten Kate, “Fully superconducting rectifiers and flux pumps Part 1: Realized methods for pumping flux,” *Cryogenics*, **21**, 195, 1981.

[51] L. J. M. van de Klundert and H. H. J. ten Kate, "Fully superconducting rectifiers and flux pumps Part 2: Commutation modes, characteristics and switches," *Cryogenics*, **21**, 267, 1981.

[52] Z. Bai, G. Yan, C. Wu, S. Ding, and C. Chen, “A novel high temperature superconducting magnetic flux pump for MRI magnets,” *Cryogenics*, **50**(10), 688, 2010.

[53] T. G. Berlincourt, “Method and apparatus for magnetic flux accumulation and current generation,” Google Patents, 1966.

[54] H. Van Beelen, *et al.*, “Flux pumps and superconducting solenoids,” *Physica* **31**, 413, 1965.

[55] T. Coombs, Z. Hong, and X. Zhu, “A thermally actuated superconducting flux pump,” *Physica C: Supercond.*, **468**, 153, 2008.

[56] Y. Yu, L. Quan, and T. A. Coombs, “Thermally actuated magnetization flux pump in single-grain YBCO bulk,” *Supercond. Sci. .Technol.*, **22**(10), 105011, 2009.

[57] T. A. Coombs, Z. Hong, Y. Yan, and C. D. Rawlings, “The Next generation of superconducting permanent magnets: The flux pumping method,” *IEEE Trans. Appl. Supercond.*, **19**(3), 2169, 2009.

[58] T. A. Coombs, Z. Hong, X. Zhu, and G. Krabbes, “A novel heat engine for magnetizing superconductors,” *Supercond. Sci. .Technol.*, **21**(3), 034001, 2008.

[59] Y. Yu, H. Chiahao, H. Zhiyong, X. Wei, W. Yuan, and T. A. Coombs, “A novel design of thermally actuated magnetization flux pump for high temperature superconducting bulks,” *IEEE Trans. Appl. Supercond.*, **21**(3), 1568, 2011.

[60] T. A. Coombs, O. Hadeler, M. Zhang, and K. Matsuda, “Flux pumping, fluctuations and climbing fields,” *Supercond. Sci. .Technol.*, **25**(10), 104007, 2012.

[61] T. A. Coombs, “A finite element model of magnetization of superconducting bulks using a solid-state flux pump,” *IEEE Trans. Appl. Supercond.*, **21**(3), 3581, 2011.

[62] C. Hoffmann, D. Pooke, and A. D. Caplin, “Flux pump for HTS magnets,” *IEEE Trans. Appl. Supercond.*, **21**(3), 1628, 2011.

[63] R. M. Walsh, R. Slade, P. Donald, and C. Hoffmann, “Characterization of current stability in an HTS NMR system energized by an HTS flux pump,” *IEEE Trans. Appl. Supercond.*, **24**(3), 4600805, 2014.

[64] C. Hoffmann, R. Walsh, E. Karrer-Mueller, and D. Pooke, “Design parameters for an HTS flux pump,” *Phys. Proc.*, **36**, 1324, 2012.

[65] T. A. Coombs, J. F. Fagnard, and K. Matsuda, “Magnetization of 2-G coils and artificial bulks,” *IEEE Trans. Appl. Supercond.*, **24**(3), 8201005, 2014.

[66] Z. Jiang, C. W. Bumby, R. A. Badcock, and H.-J. Sung, “A novel rotating HTS flux pump incorporating a ferromagnetic circuit,” *IEEE Trans Appl. Supercond.*, **26**(2), 4900706, 2016.

[67] Z. Jiang, K. Hamilton, N. Amemiya, R. A. Badcock, and C. W. Bumby, “Dynamic resistance of a high-T_c superconducting flux pump,” *Appl. Phys. Lett.*, **105**(11), 112601, 2014.

[68] Z. Jiang *et al.*, “Impact of flux gap upon dynamic resistance of a rotating HTS flux pump,” *Supercond. Sci. Technol.*, **28**(11), 2015.

[69] C. W. Bumby et al., “Frequency dependent behavior of a dynamo-type HTS flux pump,” *IEEE Trans. Appl. Supercond.*, **27**(4), 5200705, 2017.

[70] A. E. Pantoja, Z. Jiang, R. A. Badcock, C. W. Bumby, “Impact of stator wire width on output of a dynamo-type HTS flux pump,” *IEEE Trans. Appl. Supercond.*, **26**(8), 4805208, 2016.

[71] R. A. Badcock et al., “Impact of magnet geometry on output of a dynamo-type HTS flux pump,” *IEEE Trans. Appl. Supercond.*, **27**(4), 5200905, 2017.

[72] C. W. Bumby et al., “Through-wall excitation of a magnet coil by an external-rotor HTS flux pump,” *IEEE Trans. Appl. Supercond.*, **26**(4), 0500505, 2016.

[73] C. W. Bumby et al., “Development of a brushless HTS exciter for a 10 kW HTS synchronous generator,” *Supercond. Sci. Technol.*, **29**(2), 024008, 2016.

[74] H.-J. Sung et al., “Design and heat load analysis for a 12 MW HTS wind power generator module employing brushless HTS exciter,” *IEEE Trans. Appl. Supercond.*, **26**(4), 5205404, 2016.

[75] C. W. Bumby, Z. Jiang, A. E. Pantoja, and R. A. Badcock, “Anomalous open-circuit voltage from a high-T_c superconducting dynamo,” *Appl. Phys. Lett.*, **108**(12), 122601, 2016.

[76] T. Nakamura, M. Sugano, T. Doi, and N. Amemiya, “Flux pump effect of HTS films in a traveling magnetic field,” *IEEE Trans. Appl. Supercond.*, **20**(3), 1033, 2010.

[77] Z. Bai *et al.*, "A newly developed pulse-type microampere magnetic flux pump," *IEEE Trans. Appl. Supercond.*, **20**(3), 1667, 2010.

[78] Z. Bai, C. Chen, Y. Wu, and Z. Zhen, "Effect of various pulse waveforms for pulse-type magnetic flux pump," *Cryogenics*, **51**(9), 530, 2011.

[79] L. Fu, K. Matsuda, and T. A. Coombs, "Linear flux pump device applied to HTS magnets: further characteristics on wave profile, number of poles, and control of saturated current," *IEEE Trans. Appl. Supercond.*, **26**(3), 0500304, 2006.

[80] L. Fu, K. Matsuda, M. Baghdadi, and T. Coombs, "Linear flux pump device applied to high temperature superconducting (HTS) magnets," *IEEE Trans. Appl. Supercond.*, **25**(3), 4603804, 2015.

[81] L. Fu, K. Matsuda, T. Lecrevisse, Y. Iwasa, and T. Coombs, "Linear flux pump device applied to high temperature superconducting (HTS) magnets," *Supercond. Sci. Technol.*, **29**(4), 04LT01, 2016.

[82] M. P. Oomen et al., "HTS flux pump for cryogen free HTS magnets," *IEEE Trans. Appl. Supercond.*, **15**(2), 1465, 2005.

[83] W. Wang, M. Zhang, C. Hsu, T. Coombs, "Design consideration of a circular type magnetic flux pump device," *IEEE Trans. Appl. Supercond.*, **22**(3), 5201304, 2012.

[84] O. Sang, *et al.*, "Fabrication of Bi-2223 HTS magnet with a superconducting switch," *EEE Trans. Appl. Supercond.*, **11**(1), 1828, 2001.

[85] T. Tosaka, *et al.*, "Development of a persistent current switch for HTS magnets," *IEEE Trans. Appl. Supercond.*, **14**(2), 1218, 2004.

[86] T. Tosaka, *et al.*, "Persistent current HTS magnet cooled by cryocooler (4)—persistent current switch characteristics" *IEEE Trans. Appl. Supercond.*, **15**(2), 2293, 2005.

[87] D. K. Park, *et al.*, "Design and test of a thermal triggered persistent current system using high temperature superconducting tapes," *J. Phys.: Conf. Series*, **6**, 5, 2006.

[88] Y. Yoon, *et al.*, "Characteristics of a HTS persistent current switch system considering the n-value," *IEEE Trans. Appl. Supercond.*, **16**(2), 1745, 2006.

[89] H. Hayashi, *et al.*, "Connecting tests of superconducting persistent-current-switch in a type of current transformer to 1 kWh SMES system," *IEEE Trans. Appl. Supercond.*, **11**(1), 1904, 2001.

[90] K. Goto, *et al.*, "Development of a 1-kA, 25-ohm magnetically controlled persistent current switch for SMES," *IEEE Trans. Appl. Supercond.*, **9**(2), 173, 1999.

[91] K. Noto, *et al.*, "Development of a 50 A-fast response, magnetically controlled persistent current switch," *IEEE Trans. Appl. Supercond.*, **5**(2), 258, 1995.

[92] T. Ogasawara, K. Yasukochi, S. Nose, and H. Sekizawa, "Effective resistance of current-carrying superconducting wire in oscillating magnetic fields 1: Single core composite conductor," *Cryogenics*, **16**, 33, 1976.

[93] A. Uksusman, *et al.*, "Voltage response of current carrying Y–Ba–Cu–O tapes to alternating magnetic fields," *J. Appl. Phys.*, **105**, 093921, 2009.

[94] M. P. Oomen, *et al.*, "Dynamic resistance in a slab-like superconductor with *Jc*(B) dependence," *Supercond. Sci. Technol.*, **12**, 382, 1999.

[95] G. P. Mikitik, E. H. Brandt. "Generation of a dc voltage by an ac magnetic field in type-II superconductors," *Phys. Rev. B*, **64**(9), 092502, 2001.

[96] J. Geng, *et al.*, "HTS persistent current switch controlled by AC magnetic field," *IEEE Trans. Appl. Supercond.*, **26**(3), 6603304, 2016.

[97] J. Geng, and T. A. Coombs, "Mechanism of a high-T_c superconducting flux pump: Using alternating magnetic field to trigger flux flow," *Appl. Phys. Lett.*, **107**, 142601, 2015.

[98] J. Geng et al., "Operational research on a high-Tc rectifier-type superconducting flux pump," *Supercond. Sci. Technol.*, 29(3), 035015, 2016.

[99] J. Geng, *et al.*, "Feedback control of a rectifier type HTS flux pump: Stabilizing load current with minimized losses," *IEEE Trans. Appl. Supercond.*, 27(4), 0500104, 2017.

[100] M. Majoros, *et al.*, "Transport AC losses in YBCO coated conductors," *Supercond. Sci. Technol.*, **20**, s299, 2007.

[101] "http://www.aksteel.com/pdf/markets_products/electrical/mag_cores_data_bulletin.pdf."

[102] S. S. Kalsi. Applications of high temperature superconductors to electric power equipment. Page 53, 2011.

[103] H. L. Laquer, K. J. Carroll, and E. F. Hammel, "An automatic superconducting flux pump," *Phys. Lett.*, **21**(4), 397, 1966.

[104] K. J. Carroll, "Behaviour of a flux pump using an automatic superconducting switch," *Cryogenics*, **13**(6), 353, 1973.

[105] I. Giaever, "A dc transformer," *IEEE Spectrum*, **3**, 117, 1966.

[106] J. Geng *et al.*, "Origin of dc voltage in type II superconducting flux pumps: field, field rate of change, and current density dependence of resistivity," *J. Phys. D: Appl. Phys.*, **49**, 11LT01, 2016.

[107] J. Rhyner, "Magnetic properties and AC-losses of superconductors with power law current—voltage characteristics," *Physica C: Supercond.*, **212**, 292, 1993.

[108] G. P. Mikitik and E. H. Brandt, "Vortex shaking in rectangular superconducting platelets," *Phys. Rev. B*, **69**, 134521, 2004.

[109] J. R. Clem, "Flux-line-cutting losses in type-II superconductors," *Phys. Rew. B*, **26**(5), 2463, 1982.

[110] V. V. Andrianov, V. B. Zenkevich, V. V. Kurguzov, V. V. Sychev, and F.F. Ternovskii, "Effective resistance of an imperfect type II superconductor in an oscillating magnetic field," *Sov. Phys. JETP*, **31**, 815, 1970.

[111] R. P. Huebener, L. G. Stafford, and F. E. Aspen, "Speed of magnetic-flux penetration and eddy-current damping in thin-film superconductors," *Phys. Rev. B*, **5**, 3581, 1972.

[112] T. Ogasawara, Y. Takahashi, K. Kanbara, Y. Kubota, K. Yasohama, and K. Yasukochi, "Alternating field losses in superconducting wires carrying dc transport currents: Part 1 single core conductors," *Cryogenics*, **19**(12), 736, 1979.

[113] M. P. Risse, M. G. Aikele, S. G. Doettinger, and R. P. Huebener, “Dissipation in the superconducting mixed state in the presence of a small oscillatory magnetic-field component,” *Phys. Rev. B*, **55**, 15191, 1997.

[114] J. J. Rabbers, B. ten Haken, F. Gomory, and H. H. J. ten Kate, “Self-field loss of BSCCO/Ag tape in external AC magnetic field,” *Physica C*, **300**(1-2), 1, 1998.

[115] N. Shaked, *et al.*, “Direct current voltage increment due to ac coupling in a high *T*c superconducting coil,” *Appl. Phys. Lett.*, **73**, 3932, 1998.

[116] E. H. Brandt and G. P. Mikitik, “Why an ac magnetic field shifts the irreversibility line in type-II superconductors,” *Phys. Rev. Lett.*, **89**, 027002, 2002.

[117] Y. Jiang, R. Pei, W. Xian, Z. Hong, and T. A. Coombs. “The design, magnetization and control of a superconducting permanent magnet synchronous motor,” *Supercond. Sci. Technol.*, **21**(6), 065011, 2008.

[118] M. Baghdadi, H. S. Ruiz, and T. A. Coombs, “Crossed-magnetic-field experiments on stacked second generation superconducting tapes: Reduction of the demagnetization effects,” *Appl. Phys. Lett.*, **104**, 232602, 2014.

[119] Y. Yeshurun, A. P. Malozemoff, and A. Shaulov, “Magnetic relaxation in high-temperature superconductors,” *Rev. Mod. Phys.*, **68**, 911, 1996.